MORPHODYNAMICS OF SINGLE-BARRED EMBAYED BEACHES

SHORELINE AND BARLINE MORPHODYNAMICS AT THE SCALE OF THE EMBAYMENT

Dissertation zur Erlangung des Doktorgrades der Naturwissenschaften (Dr. rer. nat.)
im Fachbereich Geowissenshaften der Universität Bremen

Dissertation in fullfillment of the requirements for the Doctoral degree in Natural Sciences (Dr. rer. nat.)
at the Department of Geosciences at Bremen University, Germany

vorgelegt von
presented by

Brice Blossier

Bremen, Oktober 2015

marum INTERCOAST THE UNIVERSITY OF WAIKATO *Te Whare Wānanga o Waikato* Universität Bremen

Supervisors:

PD Dr. Christian WINTER
Prof. Dr. Karin BRYAN

Date of PhD defence:

1st of June, 2016

PhD defence committee:

PD Dr. Christian WINTER
Prof. Dr. Karin BRYAN
Prof. Dr. Michael SCHULZ
Prof. Dr. Dierk HEBBELN
Dr. Gerald HERRLING
Mareike BERGHALD

Declaration

Brice Blossier

INTERCOAST - Integrated Coastal Zone And Shelf Sea Research

Fachbereich 05 - Geowissenschaften
Leobener Strasse
28359 Bremen

Email: bblossier@marum.de

Date: 29/10/2015

Hiermit versichere ich, dass ich die Arbeit ohne unerlaubte fremde Hilfe angefertigt habe, keine anderen als die von mir angegebenen Quellen und Hilfsmittel benutzt habe und die den benutzten Werken wörtlich oder inhaltlich entnommenen Stellen als solche kenntlich gemacht habe.

Herewith I certify that the present thesis has been achieved without external support and that I did not use other than quoted sources and auxiliary means. All statements which are literally or analogously taken from other publications have been identified as quotations.

Das Thema und die Struktur der wissenschaftlichen Artikel (Kapitel 2, 4 und 5) wurden vom Autor in Zusammenarbeit mit den Mitautoren entwickelt. Die Methode, die Analyse und die wissenschaftliche Diskussion wurden vom Erstautor ausgearbeitet. Der Beitrag der Mitautoren zu der wissenschaftlichen Diskussion erfolgte im üblichen Rahmen der Doktorandenbetreuung.

The topic and framework of the research articles presented in chapters 2, 4 and 5 were developed by the author in cooperation with the coauthors. The methodology, analysis and the scientific discussions were elaborated by the first author. The contribution of the coauthors to the scientific discussion is in the common framework of a doctoral supervision.

Brice Blossier

Abstract

Embayed sandy beaches are commonly found along rocky coasts where sand supplied by local rivers, by-passing mechanisms or transported from the continental shelf can accumulate between headlands. Embayed beaches are also common near urban areas where structures such as groynes and breakwaters form artificial headlands. This thesis focuses especially on the morphodynamics of the shoreline and the nearshore parallel sandbar of single-barred embayed beaches, at the scale of the embayment.

Using seven years of shoreline and barline positions extracted from hourly time-averaged images collected at Tairua Beach (New Zealand), the concept of rotation usually attributed to embayed beach shorelines is extended to the nearshore sandbar of single-barred embayed beaches. The orientation appears as a relevant parameter of a reduced state description of such embayed sandbar together with its cross-shore position and alongshore variability.

The concept of rotation is further analysed by means of semi-empirical modelling to relate the rotation process to external wave conditions. A large scale numerical wave model provides a high resolution description of the wave field at Tairua Beach during the seven years of observations. A cross-shore migration model is developed to describe the migration of the barline as a function of the computed incident wave conditions. Then, a rotation model is derived from the formulation of the migration model, assuming that rotation is induced by differential cross-shore migrations of the barline along the embayment.

The models exhibit good skills and therefore support the hypothesis that the rotation of the barline is mainly driven by the cross-shore adaptation of the beach profile to varying wave conditions along the embayment. The rotation rate is explicitly related to the alongshore gradient of wave energy along the bay. The barline rotates towards an equilibrium orientation mainly controlled by this alongshore gradient by means of two different mechanisms. A pivotal rotation occurs when the extremities of the sandbar migrate in opposite directions (seawards and shorewards). On the contrary, a migration-driven rotation occurs when the entire sandbar migrates seawards or shorewards but at different rates along the embayment due to an alongshore gradient in wave energy.

Sandbar migration and rotation exhibit similar response times controlled by the depth of the sandbar crest despite the fact that the two signals are weakly correlated. At low frequencies (three months to several years time periods), the barline cross-shore position and orientation follows the variations of the wave climate properties, whereas at higher frequencies (time periods below a month), the barline tends to stabilize far offshore from the beach, perpendicular to the mean incident wave angle, in agreement with an expected transition of the beach towards more dissipative states.

Then, statistical analyses are conducted to extract the dominant modes of variability of Tairua Beach shoreline and to assess possible relationships between the dynamics of these modes and external wave conditions. The linearity of the employed statistical methods limits the outcomes of the study. However results underline the role of long-travelling swell waves in cross-shore shoreline migration and more importantly show the strong relationship between the alongshore sediment transport and

the shoreline rotation. This observation supports the construction of a simple model that is able to simulate this rotation with good skills.

The acquired knowledge regarding the modelling of Tairua's shoreline and sandbar is then used to analyse the outcomes of two Principal Component Analyses (PCA) of the measured shoreline and barline positions performed using different methods. The first method extracts the dominant modes of variability separately for the shoreline and the barline, showing that in both cases, the morphodynamics of both lines is dominated by migration over rotation. The second method extracts the dominant modes in a combined way, so that the shoreline and barline modes are linked by their temporal function.

The second PCA shows that migration does not only dominate the morphodynamics, but that it occurs almost entirely simultaneously for the shoreline and the barline. This simultaneous behaviour is split over two modes. Firstly, a contrasting mode describes the migration of the shoreline and barline in opposite directions that relates well to the models hindcasts. This mode can be related to beach state transitions towards more reflective or more dissipative beaches. Then, secondly, a joint mode describes migrations in identical directions. This mode is not well simulated by the models and possibly relates to the embayed beach breathing process, extending then the concept of breathing to the entire beach profile and not only to the shoreline.

The rotation of the shoreline and barline appears in the first, third and fourth mode extracted by the second PCA. The first mode describes a partial simultaneity of the shoreline and barline rotation due to a wave energy dependent correlation of their main drivers, the wave obliquity for the first and the alongshore wave gradient in the embayment for the latter. The remaining variability induced by rotation is decomposed separately over the third and fourth modes, showing the large independence of the shore and bar rotation processes.

The PCAs show that shoreline and barline morphodynamic processes at the scale of the embayment are likely to occur simultaneously because they obey to identical or partially correlated drivers. However, physical coupling seems to play a limited role as these processes are well explained by non-coupled models. Physical coupling may be important in the overall cross-shore beach migration described by the joint mode since it is not well simulated by the models.

Zusammenfassung

Sandstrände in Buchten (embayed sandy beaches) entstehen entlang Felsenküsten, wenn Sand zwischen felsigen Küstenvorsprüngen akkumulieren kann. Der Sand erreicht diese Strände entweder über Flussmündungen oder durch Transportmechanismen, welche entweder küstenparallel oder -normal entlang des Kontinentalschelfs verlaufen. Diese Strände sind häufig auch in der Nähe von urbanen Gebieten zu finden, wo Küstenschutzmaßnahmen wie Buhnen oder Wellenbrecher künstliche Küstenvorsprünge bilden. Diese Doktorarbeit befasst sich mit der Morphodynamik dieser Sandstrände auf der räumlichen Skala der durch die Küstenvorsprünge eingeschlossenen Bucht; dabei wird insbesondere die Morphodynamik der Küstenlinie sowie der strandparallelen Einzel-Sandbarre betrachtet.

Die über sieben Jahre aufgezeichneten und im Stundentakt zeitlich gemittelten Videobilder vom Tairua Beach (Neuseeland) ermöglichen die Auswertung der Lagepositionen der Küstenlinie und der Sandbarre. Das Konzept der Rotation, welches für gewöhnlich nur auf die Küstenlinie dieser Strände angewandt wird, ist hier auf die strandnahe Einzel-Sandbarre erweitert worden. Die Ausrichtung der Sandbarre kann als ein relevanter Parameter einer vereinfachten Statusbeschreibung der Barre innerhalb der Bucht herangezogen werden, ebenso wie die Position entlang einer küstennormalen Achse und die räumliche Veränderung in Küstenlängsrichtung.

Das Konzept der Rotation wird weiterhin mithilfe semi-empirischer Modelle analysiert, um den Zusammenhang zwischen Rotationsprozess und dem Seegangsklima aufzuzeigen. Ein großskaliges numerisches Wellenmodell liefert eine hochauflösende Beschreibung des Wellenfeldes am Tairua Beach über den siebenjährigen Beobachtungszeitraum. Ein küstennormales Migrationsmodell wird entwickelt um die Migration der Barre in Abhängigkeit des berechneten Seegangsklimas zu beschreiben. Anschließend wird ausgehend von der Formulierung des Migrationsmodells ein Rotationsmodell abgeleitet, unter der Annahme, dass die Rotation von differentieller küstenlängsgerichteter Migration der Barre entlang der Bucht erzeugt wird.

Die Modellqualität ist gut und stützt somit die Hypothese, dass die Barrenrotation vorwiegend durch die Anpassung des küstennormalen Strandprofils als Folge veränderlicher Seegangsbedingungen entlang der Bucht verursacht wird. Die Rotationsrate ist explizit abhängig vom Küstenlängsgradienten der Seegangsenergie innerhalb der Bucht. Die Barre richtet sich in einen Gleichgewichtszustand aus, der im Wesentlichen von diesem küstenparallelen Gradienten gesteuert wird und dabei zwei unterschiedlichen Mechanismen folgt. Eine zentrale Rotation über einen Drehpunkt erfolgt, wenn die Endpunkte der Barre in entgegengesetzte Richtungen wandern (seewärts und küstenwärts). Andererseits erfolgt eine migrationsgetriebene Rotation, wenn die gesamte Barre seewärts oder küstenwärts wandert, jedoch aufgrund des küstenparallelen Wellenenergiegradientens mit unterschiedlichen Migrationsraten.

Migration und Rotation der Barre zeigen ähnliche Reaktionszeiten, welche von der Wassertiefe über dem Barrenkamm abhängen, obwohl die beiden Signale nur schwach korrelieren. Über lange Zeiträume (von drei Monaten bis zu mehreren Jahren) folgt die Position und Ausrichtung der Barrenlinie den Veränderungen des Wellenklimas. Während kürzerer Perioden (unterhalb eines

Monats) stabilisiert sich die Barre weit entfernt vom Strand senkrecht zum mittleren Wellenangriffswinkel und hin zu einem erwartungsgemäß eher dissipativen Strandprofil.

Danach werden statistische Analysen durchgeführt, um die dominanten Moden der Variabilität der Küstenlinie von Tairua Beach zu extrahieren und mögliche Beziehungen zwischen der Dynamik dieser Moden und den äußeren Wellenbedingungen zu bewerten. Die Linearität der verwendeten statistischen Methoden begrenzt die Aussagekraft der Untersuchungsergebnisse. Dennoch unterstreichen die Ergebnisse die Rolle der Dünung bei der küstennormalen Migration der Küstenlinie und belegen weiterhin den starken Zusammenhang zwischen dem Küstenlängstransport von Sediment und der Rotation der Küstenlinie. Diese Beobachtung spricht für den Aufbau eines einfachen Modells, welches diese Rotation gut abbilden kann.

Die bei der Modellierung der Küstenlinie und der Barre Tairuas gewonnenen Erkenntnisse werden anschließend verwendet um die Ergebnisse zweier Hauptkomponentenanalysen (Principal Component Analysis - PCA) der gemessenen Küsten- und Barrenposition mithilfe verschiedener Methoden zu analysieren. Die erste Methode extrahiert die dominanten Moden der Variabilität jeweils für die Küstenlinie und die Barrenlinie wobei klar wird, dass in beiden Fällen die Morphodynamik der Linien viel mehr von Migration und weniger von Rotation bestimmt wird. Die zweite Methode extrahiert die dominanten Moden in einer kombinierten Art und Weise, so dass die Moden der Küstenlinie und der Barrenlinie durch deren Zeitfunktion gekoppelt sind.

Die zweite PCA zeigt, dass die Migration nicht nur die Morphodynamik dominiert, sondern auch fast vollständig simultan für die Küsten- und Barrenlinie auftritt. Dieses simultane Verhalten ist auf zwei Moden verteilt. Erstens beschreibt eine entgegengesetzte Mode (contrasting mode) die Bewegung der Küsten- und Barrenlinie in entgegengesetzte Richtungen, welche gut mit den modellgestützten Reproduktionen (model hindcasts) übereinstimmt. Diese Mode kann Übergängen des Zustandes zwischen reflektiven oder dissipativen Strandprofilen zugeordnet werden. Weiterhin beschreibt eine gemeinsame Mode (joint mode) die gleichgerichtete Migration. Diese wird von den Modellen nicht gut abgebildet und steht möglicherweise im Zusammenhang mit dem Atmungsprozess von Buchtstränden (embayed beaches), wenn das Konzept der Atmung von der Küstenlinie auf das gesamte Strandprofil übertragen wird.

Die Rotation der Küstenlinie und der Barre zeigt sich in der ersten, dritten und vierten Mode, die von der zweiten PCA extrahiert werden. Die erste Mode beschreibt eine teilweise Gleichzeitigkeit der Rotation von Küsten- und Barrenlinie durch eine wellenenergieabhängige Korrelation ihrer Hauptantriebskräfte; die Wellenschiefe für erstere und der Küstenlängsgradient der Wellenhöhe innerhalb der Bucht für zweitere. Die verbleibende, durch die Rotation verursachte Variabilität verteilt sich auf die dritte und vierte Mode und verdeutlicht die klare Eigenständigkeit der Rotationsprozesse der Küstenlinie und der Barre.

Die PCAs zeigen dass sich morphodynamische Prozesse der Küstenlinie und der Barre in der Größenskala der Buchtdimensionen sich wahrscheinlich simultan abspielen, da sie die gleichen oder korrelierte Antriebskräfte besitzen. Nichtsdestotrotz scheint die physikalische Kopplung eine begrenzte Rolle zu spielen, da diese Prozesse gut durch nichtgekoppelte Modelle erklärt werden können. Die physikalische Kopplung kann für die gesamte küstennormale Strandmigration wichtig sein, die durch die gemeinsame Mode beschrieben wird, da diese von den Modellen nicht gut abgebildet wird.

Table of contents

List of Figures

List of Tables

Notation

a_b, a_s	free parameters, m
ADV_1, **ADV_2**, **ADV_3**	Acoustic Doppler Velocimeter locations
ADP	Acoustic Doppler Profiler location
α_0	free parameter, -
α_b	barline orientation defined as the slope (tangent) of the linear fit to each barline profile, -
$\alpha_{b,min}$, $\alpha_{b,max}$	minimum and maximum values of α_b over a given period, -
α_B	long-term barline orientation signal at dynamic equilibrium, -
$\underline{\alpha_B}$	complex function related to the barline orientation signal at dynamic equilibrium, -
$\alpha_{eq,b}$, $\alpha_{eq,s}$	barline and shoreline equilibrium angles, -
$\alpha_{eq,b,0}$, $\alpha_{eq,b,i}$	barline equilibrium angle for $E = E_0$ and $E = E_{max,i}$, -
α_s	shoreline orientation defined as the slope (tangent) of the linear fit to each shoreline profile, -
α_{s,t_0}	free parameter, -
B	location of BoPRC buoy
Bh	location of Bunkerhill buoy (Sylt)
BoPRC	Bay of Plenty Regional Council
b_b	free parameter, m^2
b_s	free parameter, m s^{-1}
β	lower beach profile time-averaged slope, -
Bss	Brier Skill Score, -
Bss_{y_b}, Bss_{α_b}	Brier Skill Score between modelled and measured values of y_b and α_b, -
Bss_0, Bss_1	Brier Skill Score between modelled and measured values of α_b for rotation model formulations without and with M_α, -
C	covariance of S, m^2
C1, **C2**	Sylt cameras locations, -
CCA	Canonical Correlation Analysis, -
$c_{g,b}$	wave group celerity at breaking, m s^{-1}
c_i	modes contribution to overall variance, -
c_s	free parameter, m^2
C_{α_b}, C_{α_s}	free parameters, $m^{-2}s^{-1}$
C_{y_b}, C_{y_s}	free parameters, $m^{-2}s^{-1}$
δ	free parameter, -
δ^*	embayed beach dimensionless parameter, -
δ_{λ_i}	error in eigenvalues degeneracy, -
d_s	free parameter, m^2
ΔT	time shift in coherence analysis, day

Δ_{y_b}	standard deviation defining the accuracy of the barline position data, m
E	incident wave energy defined as the square of the significant wave height H_s, m^2
E_0	steady wave energy condition, m^2
$E_{eq,b}$	equilibrium wave energy corresponding to the instantaneous barline position, m^2
$E_{eq,s}$	equilibrium wave energy corresponding to the instantaneous shoreline position, m^2
$E_{i,j}$	wave energy oscillatory signal with maximum $E_{max,i}$ and frequency f_j, m^2
EOF	Empirical Orthogonal Function
$E_{max,i}$	maximum of the wave energy oscillatory signal, m^2
E_x	amount of wave energy involved in cross-shore sediment transport, m^2
E_y	amount of wave energy involved in alongshore sediment transport, m^2
e_s	free parameter, m
F	temporal EOFs, -
f_b	damping factor, -
$f_{b,0}$	damping factor for $E = E_0$, -
$F_{i,j}$	wave energy signal with alongshore averaged constant energy $E_{max,i}$ and oscillatory alongshore gradient of frequency f_j, m^2
f_j	frequency, $year^{-1}$
F_x, $F_{x,1}$, $F_{x,2}$	wave-induced alongshore forcing and its components, m
g	gravity acceleration, m s^{-2}
γ	wave breaking criteria, 0.73, -
G_{max}	amplitude of oscillatory signal of alongshore gradient of wave energy
$\underline{H}$	complex transfer function between the alongshore gradient of wave energy and the barline orientation, -
$\lvert\underline{H}\rvert$	amplitude of complex transfer function $\underline{H}$, -
h^*	closure depth, m
H_b	breaking wave height over the bar crest, m
$H_{b,0}$	breaking wave height, m
h_{bar}	constant height of the bar over the averaged beach profile, 1 m
H_s	significant wave height, m
$H_{s,0}$	significant wave height corresponding to E_0, m
h_{y_b}	water depth over the bar crest, m
i	unit imaginary number
K	coefficient accounting for sediment properties, -
K^*	coefficient, $m^{-2}s^{-1}$
L	beach length, m
Λ	matrix of eigenvalues λ_i of C, m^2
λ_i	eigenvalues of C, m^2

m	free parameter, -
M_α	cross-shore migration-driven rotation term of rotation model, day^{-1}
n	free parameter, -
N	number of dataset samples, -
N^*	number of dataset independent samples, -
$\nabla_x(E)$	alongshore gradient of wave energy, m
$\nabla_x(F_{i,j})$	oscillatory alongshore gradient of wave energy signal $F_{i,j}$, m
$\underline{\nabla_x(F_{i,j})}$	complex function of the alongshore gradient of wave energy signal $F_{i,j}$, m
p	parameter used in the formulation of the damping factor, 8, -
P	eigenvectors of C (spatial EOFs)
PCA	Principal Component Analysis
$\phi(E_{i,j})$	phase of signal $E_{i,j}$, -
$\phi(\underline{H})$	phase of complex transfer function $\underline{H}$, -
$\phi(Y_B)$	phase of signal Y_B, -
$\Psi_{\alpha,1}$	relative amplitude between the amplitude of α_b computed by the rotation model and the maximum expected range of α_b values, -
$\Psi_{\alpha,2}$	phase between α_b computed by the rotation model and the forcing signal $\nabla_x(F_{i,j})$, -
$\Psi_{y,1}$	relative amplitude between the amplitude of y_b computed by the migration model and the maximum expected range of y_b values, -
$\Psi_{y,2}$	phase between Y_B computed by the migration model and the forcing signal $E_{i,j}$, -
$\Psi_{y,3}$	ratio between average value of Y_B maximum reachable barline position
r	correlation, -
R^2	squared correlation coefficient, -
$R^2_{y_b}$,$R^2_{\alpha_b}$	squared correlation coefficient between modelled and measured values of y_b and α_b, -
R^2_0,R^2_1	squared correlation coefficient between modelled and measured values of α_b for rotation model formulations without and with M_α, -
R_α	pivotal rotation term of rotation model, day^{-1}
ρ_w	water density, kg m^{-3}
$RMSE$	root mean square error
$RMSE_{y_b}$, $RMSE_{\alpha_b}$	root mean square error between modelled and measured values of y_b and α_b
$RMSE_0$, $RMSE_1$	root mean square error of α_b for rotation model formulations without and with M_α
S	two-dimensional signal depending on time and space
S4_1, **S4_2**, **S4_3**	S4 locations during Tairua beach campaign, 2014
S4_N, **S4_S**, **S4_P**	S4 locations during Tairua beach campaign, 2011
S_b	time-varying signal
S_n	n$^{\text{th}}$ surrogate signal based on red noise
$S_{b,c}$, $S_{b,m}$	computed and measured value of signal S_b

σ	standard deviation, m
σ_{y_b}	standard deviation of y_b over a certain period, m
σ_{y_s}	standard deviation of y_s over a certain period, m
σ_{α_b}	standard deviation of α_b over a certain period, -
$\sigma_{S_{b,c}}$, $\sigma_{S_{b,m}}$	standard deviation of computed and measured value of signal S
t	time, day
τ_{α_b}	instantaneous characteristic response time of the barline rotation, day
$\tau_{\alpha_b,i}$	instantaneous characteristic response time of the barline rotation for $E = E_{max,i}$ and $y_b = y_{eq,i}$, day
τ_{α_s}	instantaneous characteristic response time of the shoreline rotation, day
τ_{y_b}	instantaneous characteristic response time of the barline cross-shore migration, day
τ_{y_s}	instantaneous characteristic response time of the shoreline cross-shore migration, day
T_d	characteristic time equal to one day
θ	peak incident wave angle, -
θ_0	steady peak incident wave angle condition, -
T_m	mean wave period, s
T_p	peak wave period, s
O	origin of the local reference frame at Tairua Beach
x	alongshore dimension in the local reference frame, increasing southwards, m
x_i	alongshore position of i$^{\text{th}}$ transect, m
y	cross-shore dimension in the local reference frame, increasing seawards, m
y_b	barline alongshore averaged cross-shore position, m
$y_{b,0}$	equilibrium barline cross-shore position for $E = E_0$, m
$y_{b,min}$, $y_{b,max}$	minimum and maximum values of y_b over a given period, m
$y_{eq,0}$	equilibrium barline cross-shore position for $E = E_0$, m
$y_{eq,E=0}$	equilibrium barline cross-shore position for $E = 0$, m
$y_{eq,i}$	equilibrium barline cross-shore position for $E = E_{max,i}$, m
Y_B	long-term barline cross-shore position signal at dynamic equilibrium, m
y_s	shoreline alongshore averaged cross-shore position, m
y_s'	shoreline cross-shore fluctuations explained by a semi-empirical model, m
$< S_b >$	time averaging of S_b
$\tilde{S}$	demeaned linearised component of S in the alongshore dimension
$\overline{S}$	alongshore averaging of S

Acknowledgments

The present work was funded by the Deutsche Forschungsgemeinschaft (DFG) through the International Research Training Group INTERCOAST (Integrated Coastal Zone and Shelf-Sea Research) and MARUM (Centre for Marine Environmental Sciences, University of Bremen).

I would like to acknowledge my supervisors PD. Dr. Christian Winter and Prof. Dr. Karin Bryan for their support all along this PhD. I appreciated their ideas and their advice towards this research and I enjoyed the transmission of their enthusiasm towards coastal morphodynamics in general. I would like to particularly thank them for giving me entire freedom and enough time to explore technical instruments and participate to a research cruise while keeping this work on track.

I want to deeply acknowledge Dr. Christopher Daly for his support throughout the thesis, his advice while sharing the same office, his introduction to New Zealand, his patient work in collecting data that saved me a great amount of time and his careful reviews.

This is also for me the occasion to thank my Master's thesis supervisors at TU Delft and Deltares (Netherlands) who introduced me to coastal dynamics and particularly to sandbars dynamics and numerical modelling.

During my PhD, the INTERCOAST program gave me the opportunity to conduct my research in New Zealand for six months. I would like to deeply thank the University of Waikato for hosting this cooperation and all the members of the Coastal Marine Group for their warm welcoming and their support. I acknowledge in particular the technical staff, Dirk Immenga, Dean Sandwell and Chris Morcom for their availability and active participation in our beach campaign in 2014. This is for me the occasion to also thank Tobias Kulgemeyer and Franziska Staudt, members of INTERCOAST, for their assistance in the construction of the Lagrangian drifters, Franziska Hellmich, for her help during the design of the campaign as well as Mariana Cussioli, Christina Gawrych, Victor Godoi, Rafael Guedes, Priscilla Lad, James Robinson, Simon Steward and Justin Walker for their additional help during their deployment.

This research would not have been possible without the support of the Coastal Dynamics working group of MARUM. It was for me a great pleasure to be regularly involved in the research of my fellows and friends. I deeply appreciated our enjoyable discussions and debates about mud dynamics, bedforms, Columbian beaches and numerical modelling. As well it was a great pleasure to be part of our research experiments in the North Sea and along the German coast.

I would like to thank the staff of INTERCOAST for their assistance during the PhD, within the administrative tasks but also regarding the organisation of our yearly workshops. As well I would like to thank my PhD fellows and friends from INTERCOAST who greatly helped me to apprehend Germany and New Zealand, in particular Merle Bollen and Alex Port.

To finish, all this work would not have been possible without the support and patience of my family, my parents, my brother and sister all along my higher education. I would like to thank them for their encouragements and their understanding, especially during the last phase of this PhD. I would

also like to thank all the friends I met along my education in France, in the Netherlands, in Germany and elsewhere who always made my studies a pleasure.

Special thanks to Alice, my partner, who supported me patiently during long working evenings and nights and who provided me with the necessary strength to accomplish this PhD.

Chapter 1

General introduction

1.1. Coastal systems: attractive areas confronted to interactions and conflicts

Coastal areas constitute by definition interfaces between land and sea and as such provide humanity with a large amount of goods and services. According to *Costanza et al.* [1997], the coastal biome including estuaries, seagrass, algae beds, coral reefs and continental shelves produces 38 % of the world's ecosystem services and natural capital. In addition, wetlands (including tidal marshes, mangroves, swamps and floodplains) provide an additional 15 %. The main ecosystem services supplied by coastal areas are their ability to damp environmental fluctuations by providing storm protection and flood control, and their capacity of creating the appropriate conditions for efficient nutrient cycling and biological control. As well, they play an important role in supplying food, providing recreational areas and integrate a significant cultural dimension.

This large supply of goods and services results in a high attractiveness of littoral areas. This is reflected by the fact that 30 % of the population was found within 100 km from the coast in 1990 [*Small and Nicholls* 2003] and 41 % in 2002 [*Martínez et al.* 2007, *UN Millenium Project* 2005]. More precisely, 635 million or 10.9 % of the world's population lived in 2000 in the low-elevation coastal zone (contiguous and hydrologically connected coastal areas below 10 m elevation, LECZ) constituting 2.3 % of the land area of coastal countries [*Neumann et al.* 2015]. According to their study, this number is likely to grow up to approximately 900 million in 2030 and will exceed a billion in 2060.

This high attractiveness implies the cohabitation of economical, urban and social interests. The economy sector includes different activities among which harbour activity (e.g. fishing, international shipping, mining), agriculture and tourism. These activities induce a development of coastal infrastructures in different manners. Harbour activity requires the safety of moored ships by means of coastal protections such as breakwaters and the maintenance of navigability by means of dredging. Agriculture and in particular aquaculture can lead to large modifications of the coastal environment such as the large scale mangrove deforestation accomplished to install shrimp farms in Asia [*Adger et al.* 2005]. In addition, conventional agriculture in coastal regions is likely to release high quantity of nitrates, inducing eutrophication and provoking algae blooms in coastal waters (e.g. in France [*Dion and Bozec* 1996]). On the opposite, tourism actors tend to defend aesthetic and cultural assets that are of primary importance for the sector. Urban interests deal mainly with the development of the aforementioned coastal infrastructures, but cities also account for social interests by planning the development of residential and recreational areas, while minimizing flood risks for all coastal actors.

When the interactions between these different stakeholders is not properly handled, conflicts arise and induce degradations of the coastal ecosystem. Incidentally they provoke a decrease of the resilience of the system, meaning that the degraded system becomes unable to absorb recurrent disturbances [*Duxbury and Dickinson* 2007]. This study mentions that natural, institutional and financial resources are the major matter of conflicts between economical and social interests. The authors add that authorities and decision-makers often take their decisions on a case-by-case basis, rather than agreeing on a long-term planning based on an overall agreement of local actors. This results in an unorganised growth of coastal areas and yields potentially to disasters such as hurricane Katrina in New Orleans in 2005 [*Burby* 2006], or storm Xynthia in France in 2010 [*Chadenas et al.* 2014].

The effect of this unorganised growth on the resilience of coastal systems, in particular regarding flood risks, is amplified by the effects of climate change. Indeed, the resulting potential sea level rise [*Nicholls and Cazenave* 2010] but also the potential increase of the intensity and frequency of extreme events [*Knutson et al.* 2010] which are responsible for two third of the coastal disasters [*Adger et al.* 2005] increase the level of potential coastal damage and therefore the level of risk related to flood hazards in coastal areas.

To answer these issues, researchers and intergovernmental institutions advise decision-makers and coastal stakeholders to work together in a process called *adaptive management*. This decision-making process aims at maintaining the sustainability and the resilience of coastal areas by integrating private stakeholders, scientists and public authorities in a decision-making process allowing for uncertainties to be progressively assessed [*Costanza et al.* 1998, *Murray and Marmorek* 2003, *Adger et al.* 2005, *Duxbury and Dickinson* 2007]. Adaptive management loops over six main stages [*Murray and Marmorek* 2003, *Duxbury and Dickinson* 2007]:

1. Assess resources and system dynamics, build knowledge
2. Design solutions including state-of-the-art knowledge
3. Implement solutions including private stakeholders and public institutions
4. Monitor and assess the environmental feedback
5. Evaluate the results and share the obtained knowledge
6. Adjust and redefine the levels of uncertainties across spatial scales and decision levels

While this integrated and multi-disciplinary approach was already encouraged in international programs such as the Agenda 21 (*United Nations Conference on Environment and Development, Rio de Janeiro, Brazil* [1992]), its implementation is not yet widespread at the national level. As an example, adaptive management has been adopted by New Zealand in 2001 as a case law in the framework of the Resource Management Act (1991), has been applied since in six court cases involving marine farms and energy companies and is now found in the New Zealand Coastal Policy Statement [*New Zealand Department of Conservation* 2010], a document guiding local authorities in their management of the coastal environment. Adaptive management was also recommended by the U.S. Army Corps of Engineers in 2009 as the best approach to provide efficient solutions for coastal restoration and the protection of South Louisiana against storm surges (Louisiana Coastal Protection and Restoration Technical Report, *U.S. Army Corps of Engineers* [2009]).

In such a decision-making process, the improvement of the global knowledge about coastal systems is of primary importance in order to decrease the uncertainty related to the implementation of

infrastructures nearshore. While coastal systems exhibit a wide range of morphologies (estuaries and deltas, coral reefs, mangrove forests, tidal marshes, swamps, open coast sand beaches), the present thesis aims at improving the understanding of headland-bay coastal systems that represent 50 % of the world's coastline [*Short* 1999].

1.2. Headland-Bay coastlines

As mentioned in the previous section, the headland-bay coastal system is one of the most common type of coastline found in the world. In nature, such coastlines are usually found along rocky shores forming embayed beaches where local sand – supplied by rivers, by-passing effects or coming from the continental shelf – can accumulate. As with other coastal systems, embayed beaches are subject to rising anthropogenic pressure that has been the focus of recent studies [*Cavazza et al.* 2000, *Healy and Soomere* 2008, *Chaibi and Sedrati* 2009, *Lasagna et al.* 2011, *Mrini et al.* 2012, *Albino et al.* 2015]. Embayed beaches are not only common because of their large occurrence among natural coastal settings, in which case rocky headlands often offer attractive and spectacular development sites. They also widely occur in urban settings because man-made coastal structures related to shore protection and harbour development, namely groynes and breakwaters, constitute artificial headlands (e.g. in Italy [*Archetti and Romagnoli* 2011], Spain [*Ojeda and Guillén* 2008] and Estonia [*Soomere et al.* 2008]).

The development of the understanding of embayed beach morphodynamics has been conducted following different approaches. Researchers first attempted to understand their long-term development by creating the concept of *static bay shape* equations. This concept relates the long-term average wave angle of incidence to the generation of longshore currents in the embayment [*LeBlond* 1972] and wave diffraction at the upstream headland tip [*Rea and Komar* 1975] that eventually result into half-hearted shapes [*Silvester* 1960], logarithmic-spiral shapes [*Yasso* 1965] or parabolic shapes [*Hsu and Evans* 1989]. Recent studies emphasized the possible role of other drivers such as the variability of the wave angle of incidence in the development of such planform shapes [*Daly et al.* 2014].

This approach, suitable for long-term equilibrium of embayed beach shorelines planform shapes, however, does not explain the variability of the upper beach profile at shorter time scales. In order to characterise the flow circulations and the underlying morphological patterns that occur in sandy embayments, a classification depending on the geometrical settings of the bay has been proposed in *Short* [1999] and refined in *Castelle and Coco* [2012]. The latter study proposes a parameter comparing the beach length to the average surfzone width. Longer beaches tend to behave as open sandy coasts whereas short length beaches exhibit specific circulations and morphologies directly controlled by the headlands.

Regarding this classification, the present study focuses on intermediate beaches. As such, these beaches behave partially as open coast. Therefore, they exhibit transitions between more dissipative states and more reflective states [*Wright and Short* 1984]. The dissipative state is commonly found on beaches constituted of fine sand and facing high energetic conditions and is characterised by a mild slope and one to multiple nearshore parallel sandbars. The reflective state is found at low wave energy beaches and favoured by coarser grain sizes. This state exhibits a steep upper beach

slope due to the accretion of sandbars along the shoreline. For a given grain size distribution, beach states are evolving between these extreme states depending on the wave conditions. The mobility of nearshore sandbars during these transitions is accompanied by the emergence of complex morphological features associated with seaward currents flowing through rip channels depending on the wave obliquity at the bar crest [*Garnier et al.* 2013] and the wave period [*de Schipper et al.* 2014]. Rip channels are also observed at the shoreline [*Gallop et al.* 2011] and have been modelled in *Castelle and Coco* [2012], showing that they develop similarly to open coast rip channels in the case of intermediate embayed beaches. In this case, headlands influence locally the flow circulations so that headland-rip channels are observed at the beach extremities.

The transitions between beach states have been widely observed and conceptualized [*Wright and Short* 1984, *Masselink and Short* 1993, *Ferrer et al.* 2009, *Price and Ruessink* 2011]. They are characterised by an apparent migration in the cross-shore direction of the shoreline and barline at the intermediate states. More dissipative states exhibit wide surfzones with eroded shorelines and parallel sandbars located offshore. On the opposite, more reflective states are characterised by narrow surfzones with accreted shoreline and sandbars merging with the shore. The present work focuses on single-barred embayed beach, meaning that the present outcomes are applicable to beaches where state transitions do not lead to multiple parallel sandbars system where bars can decay offshore and be replaced at the shore [*Ruessink et al.* 2009].

Different models have been proposed to describe shoreline migration on open coast beaches [*Miller and Dean* 2004, *Yates et al.* 2009, *Davidson et al.* 2010; 2013, *Jara et al.* 2015] as a function of the incident wave energy. Using these models, shoreline migration is well described on monthly to interannual scales (2 to 3 years). Similar results have been obtained for barline migration with the models of *Plant et al.* [1999] and *Plant et al.* [2006]. In this case, the short-term description has been improved in *Splinter et al.* [2011] by including the development of the barline alongshore variability related to larger wave periods.

In addition to beach state transitions and cross-shore migration processes, embayed beaches exhibit particular morphodynamic patterns that relate to varying morphological development of the beach profile along the bay. This results in apparent rotations of the beach shoreline and nearshore sandbars. Shoreline rotation in embayments has been already observed in *Clarke and Eliot* [1982] but it is in the last decade that research focused intensely on the topic with observational studies [*Klein et al.* 2002, *Ojeda and Guillén* 2008, *Archetti and Romagnoli* 2011, *Bryan et al.* 2013], statistical studies [*Short and Trembanis* 2004, *Harley et al.* 2011, *Turki et al.* 2013a, *Harley et al.* 2015] and modelling studies [*Turki et al.* 2013b]. On the other hand. research is lacking on sandbar rotation as available studies are mainly observational [*Ojeda et al.* 2011, *van de Lageweg et al.* 2013]. Although evidence of shore-bar coupling has been shown numerically [*Castelle et al.* 2010a;b] and observed [*Guedes et al.* 2012, *van de Lageweg et al.* 2013], potential interactions between nearshore sandbars and the shoreline at embayed beaches at the scale of the embayment has not yet been studied in details.

1.3. Objectives

Section 1.1 showed that improving the understanding of the behaviour of coastlines is a requirement in order to provide adequate solutions to the issues raised by the anthropogenic pressure and the effects of climate change in coastal areas. The present thesis focuses in particular on intermediate single-barred embayed beaches that are long enough to observe open coasts flow patterns and short enough to observe a consistent gradient of wave energy along the embayment in case of oblique waves. This work aims at developing the understanding of their morphodynamics at the scale of the embayment by answering the following research questions:

1. ***How significant is sandbar rotation at single-barred embayed beaches and how does it relate to external conditions?***

Embayed shoreline morphodynamics at the scale of the embayment have been extensively studied [*Clarke and Eliot* 1982, *Ojeda and Guillén* 2008, *Harley et al.* 2011, *Turki et al.* 2013b]. In these studies, the orientation of the shoreline in the embayment appeared as a relevant parameter of the reduced description of the shoreline state together with its averaged cross-shore position. It is therefore pertinent to analyse if the same applies to the nearshore sandbar of single-barred embayed beaches. In this case, it becomes relevant to assess how external conditions, especially in terms of incoming waves, influence the orientation of the barline in the embayment.

2. ***Which external drivers can be related to the migration and rotation of an embayed beach shoreline?***

In embayments, a sandy beach shoreline can rotate either because of cross-shore processes, occurring for instance when there is a variation of wave conditions along the embayment [*Harley et al.* 2011; 2015], or due to longshore sediment transport induced by the obliquity of incident waves [*Turki et al.* 2013b]. The present work evaluates which wave climate parameters are involved in the rotation of the shoreline of an intermediate embayed beach.

3. ***How are the behaviours of the shoreline and the sandbar of a single-barred embayed beach interrelated at the scale of the embayment?***

Shoreline and barline interdependency and coupling has been studied in the recent years, in particular concerning the emergence of rip channels [*Castelle et al.* 2010a;b, *van de Lageweg et al.* 2013] but also concerning swash zone flow dynamics [*Guedes et al.* 2012] and therefore focusing on spatial scales several times smaller than the embayment length (for intermediate embayments). The present work analyses whether or not the shoreline and barline exhibit simultaneous or asynchronous behaviours, how such behaviours can be related to external forcing conditions, and finally evaluates if the location of the barline controls the location of the shoreline and vice versa.

1.4. Approach and thesis outline

The work presented in this thesis is based on the study of an intermediate embayed beach located in the North Island of New Zealand in the Coromandel Peninsula, Tairua Beach. A video imagery system installed in 1999 by the Waikato Regional Council and maintained by the National Institute

for Water and Atmospheric Research (NIWA) recorded time-averaged images of Tairua Beach every daylight hour since its installation. Seven years of shoreline and barline positions extracted from these images after georectification [*van de Lageweg et al.* 2013] were used as the main support of the following work. It is assumed all along the thesis that the transfer of sediment into and out of the embayment was either negligible or in balance, so that the amount of sand at the beach was conserved.

In chapter 2, the 7-year dataset of barline positions was first used to assess the relevance of the bar orientation in the embayment as a parameter of the reduced description of the bar state. To validate these observations, a wave model was developed at the regional scale in order to hindcast the spatial wave pattern over Tairua's embayment. This was used to calibrate and validate a new model relating the orientation of single-barred embayed beaches barline to the alongshore gradient of wave energy in the embayment. In chapter 3, the barline rotation model is applied to characterise the response of the barline to varying frequencies in the incident wave conditions (e.g. higher storm frequency, low-frequency fluctuations driven by climate oscillations).

In chapter 4, the 7-year dataset of shoreline positions was analysed using two statistical methods. A Principal Component Analysis extracts the dominant modes of variability of the shoreline signal. Then a Canonical Correlation Analysis relates these modes to external wave climate parameters and allows the identification of a relationship between shoreline rotation and the amount of wave energy contributing to alongshore sediment transport.

In chapter 5, the dominant modes of variability are extracted for the shoreline and barline signals first separately, and then for the shore-bar system. These two methods enable to identify dominant behaviours as well as simultaneous and asynchronous shore and bar morphodynamic patterns. The results in terms of shoreline and barline modelling from chapter 2 and chapter 4 are then used to provide an interpretation of the different modes of shore and bar variability by identifying the hydrodynamic processes that are potentially involved in their dynamics.

Chapter 2

Nearshore sandbar rotation at single-barred embayed beaches

B. Blossier [(1)], K.R. Bryan [(2)], C.J. Daly [(3)] and C. Winter [(1)]

[(1)] MARUM, Center for Marine Environmental Sciences, University of Bremen, Leobener Strasse 28359 Bremen, Germany.
[(2)] Coastal Marine Group, Faculty of Science and Engineering, University of Waikato, Hamilton, New Zealand.
[(3)] Department of Civil and Environmental Engineering, University of the West Indies, St. Augustine, Trinidad and Tobago.

In second review at *Journal of Geophysical Research: Oceans*

2.1. Abstract

The location of a shore-parallel nearshore sandbar derived from seven years of video imagery data at the single-barred embayed Tairua Beach (NZ) is investigated to assess the contribution of barline rotation to the overall morphodynamics of sandbars in embayed environments and to characterise the process of rotation in relation to external conditions. Rotation induces cross-shore barline variations at the embayment extremities on the order of magnitude of those induced by alongshore uniform cross-shore migration of the bar. Two semi-empirical models have been developed to relate the barline cross-shore migration and rotation to external wave forcing conditions. The rotation model is directly derived from the cross-shore migration model. Therefore its formulation advocates for a primary role of cross-shore processes in the rotation of sandbars at embayed beaches. The orientation evolves towards an equilibrium angle directly related to the alongshore wave energy gradient due to two different mechanisms. Either the bar extremities migrate in opposite directions with no overall cross-shore bar migration (pivotal rotation) or the rotation relates to an overall migration of the barline which is not uniform along the beach (migration-driven rotation). Migration and rotation characteristic response times are similar, ranging from 10 to 30 days for mild and energetic wave conditions and above 200 days during very calm conditions or when the bar is located far offshore.

2.2. Introduction

Embayed sandy beaches are common coastal features representing approximately 50 % of the world's coastlines [*Short* 1999, *Ratliff and Murray* 2014]. They are located along rocky coasts where the local supply of sand from rivers, from by-passing around headlands or from the inner continental shelf allows the beach to form. Embayed beaches are also common in urban areas where coastal infrastructure such as harbour breakwaters, jetties and groins create artificial headlands [*Ojeda and Guillén* 2008].

In embayed environments, the influence of headlands on the hydrodynamics results in an equilibrium between flow circulation and shoreline response, which gives these beaches their characteristic shapes [*Daly et al.* 2014] on the timescale of one to several years [*Daly et al.* 2011; 2015]. Different empirical formulations have been proposed for these planform shapes such as the logarithmic-spiral of *Yasso* [1965] or the parabolic bay shape equation from *Hsu and Evans* [1989]. Studies usually relate the development of these equilibrium shapes to headland-induced diffraction of the incident waves [*Leblond* 1979, *Iglesias et al.* 2009, *Silva et al.* 2010]. However, *Daly et al.* [2014] showed that the variability in the peak wave incident direction associated with the shadowing effect induced by the surrounding headlands could also explain the characteristic curvature of embayed beach profiles.

The control of headlands over wave propagation does not only directly control the long-term morphological development of embayed beaches but also affects their short-term topography. In particular, the length and spacing of the headlands influence the number of rip channels emerging in the embayment on the timescales of weeks to months [*Short* 1999]. When the headland spacing is much larger than the headland length, the beach tends to behave as a regular straight open coast with rip currents observed at each of the headlands. This case is commonly associated with four rips or more (excluding the headland rips) according to *Castelle and Coco* [2012]. When the headland spacing is of the order of the headland length, the circulation is mainly determined by the beach geometry and exhibits either two headland rip currents or one central rip current. In between these two extremes, the flow circulation remains significantly influenced by the headlands (with headland rip currents and spacing different than that observed in open conditions).

Therefore, if the spacing of headlands is large enough, embayed beach morphodynamics exhibit the usual behaviour of straight open beaches, with profiles ranging over the different beach states proposed by *Wright and Short* [1984]. In this case, the effect of energetic wave conditions, potentially enhanced by fine grain sizes distributions, yields to a dissipative beach state characterised by a mildly-sloped cross-shore profile and the occurrence of one to several shore-parallel sandbars. Fair weather conditions, potentially enhanced by coarse grain sizes distributions usually drive the beach morphology towards the reflective beach state with a typical longshore-uniform steep profile without bars. The transition from the dissipative to the reflective state, frequently occurring during a fair weather period following a storm, is characterised by the shoreward migration of the sandbars as well as the simultaneous progradation of the shoreline [*Ranasinghe et al.* 2004a, *Ojeda et al.* 2011]. The opposite transition can be observed when a storm occurs after fair weather conditions. Energetic events induce a significant erosion of the shoreline and an upstate change from more reflective to more dissipative. The overall beach slope becomes more gentle (although the upper beach face

can become faceted) and shore parallel sandbars form at the outer edge of the surfzone.

In addition to the open coast beach state morphodynamics, embayed beaches also experience rotation. The rotation of embayed beaches usually refers to shoreline rotation in which both extremities of the beach behave in opposing ways (one progradates while the opposite one erodes) [*Ranasinghe et al.* 2004b, *Ojeda and Guillén* 2008, *Harley et al.* 2011, *Turki et al.* 2013b]. Observations have shown that beach rotation events occur on varying timescales. On the daily to weekly scale, rotation is directly related to storm events [*Ojeda and Guillén* 2008], whereas decadal time scales have been linked to the long-term variations of the incident wave direction and energy related to climate indicators. This has been demonstrated by *Ranasinghe et al.* [2004b] in the case of beaches located on the eastern coast of Australia influenced by the Southern Oscillation Index.

The rotation of embayed beach shorelines is usually associated with the obliquity of incident waves and a consequent longshore transfer of sediments from one extremity of the beach towards the other [*Short* 1999, *Ojeda and Guillén* 2008]. *Turki et al.* [2013b] implemented this hypothesis in a semi empirical model by relating directly the volume of sand transported along the beach during a rotation event (removed at one extremity of the beach and deposited at the other) to the alongshore sediment transport induced by the incident wave conditions and computed using the formulations of *Inman and Bagnold* [1963] and *Komar and Inman* [1970]. The longshore transport depends on the angle between the breaking waves and the shoreline, and reaches zero when waves are normal to the beach. Therefore the model of *Turki et al.* [2013b] defines an equilibrium shoreline angle corresponding to the orientation of the breaking waves crests and the shoreline rotation rate depends linearly on the difference between the actual shoreline orientation and the equilibrium one. The resulting semi-empirical model was able to accurately reproduce the shoreline rotation of three neighbouring embayed beaches in Barcelona (Spain).

Conversely, other studies indicate that alongshore differences in cross-shore processes are the dominant driver in the rotation of shorelines. For example, *Ranasinghe et al.* [2004b] explained that the alongshore variations of wave energy related to the incident angle of energetic wave events played a role in the rotation of eastern Australia embayed beach shorelines. Conducting a principal component analysis and focusing on extreme accretionary and erosive events, *Harley et al.* [2011] highlighted the dominance of cross-shore sediment transport processes in shoreline rotation events at Collaroy-Narrabeen Beach (southeast Australia). They related contrasting erosion-sedimentation patterns at the north and the south of the beach with concomitant alongshore variations of the incident wave energy. Higher (lower) incident wave energy was related to the evolution of the beach towards dissipative (reflective) profiles and to erosion (sedimentation) at the shoreline respectively. This results in an apparent rotation of the beach shoreline. Observed shoreline rotation would therefore not only result from a longshore transfer of sediments along the beach but also from a contrasting development of the cross-shore profiles at each extremity of the beach due to alongshore varying wave energy intensities. Nonetheless these studies do not consider the fact that an alongshore gradient of wave energy induces alongshore radiation stresses in the water column that are likely to generate a longshore current able to transport sediments along the beach. Therefore cross-shore and alongshore sediment transport processes are likely to be involved simultaneously in rotation events.

Although many studies of embayed beaches have focused on the behaviour of the shorelines, only few have examined the alongshore behaviour of sandbars. However nearshore barlines strongly

influence the morphology of shorelines. For instance, *Guedes et al.* [2011] have stressed their role in attenuating the incident wave energy by inducing wave breaking at the seaward edge of the surfzone that eventually results in coupling effects between the barline and the shoreline [*Castelle et al.* 2010a, *van de Lageweg et al.* 2013]. Recent sandbar studies using numerical models and long-term datasets obtained using video techniques [*Lippmann and Holman* 1990, *Pape et al.* 2007, *Price and Ruessink* 2011], have concentrated on cross-shore movement of sandbars, and the processes controlling the emergence of patterns. For example, *Plant et al.* [1999], *Ruessink et al.* [2007a], *Pape et al.* [2007], *van Maanen et al.* [2008] investigated the alongshore-averaged sandbar cross-shore migration. *Reniers et al.* [2004], *Plant et al.* [2006], *Splinter et al.* [2011], *de Schipper et al.* [2014] focused on the development of complex three dimensional morphological features along the sandbar. The models used in these studies are either process-based [*Reniers et al.* 2004, *Ruessink et al.* 2007a, *de Schipper et al.* 2014], exclusively data-driven [*Pape et al.* 2007] or based on semi-empirical formulations [*Plant et al.* 1999; 2006, *Splinter et al.* 2011].

In relation to their computation costs, these three different modelling approaches provide different insights in terms of the description and understanding of the modelled system. Most costly, process-based models attempt to include increasingly detailed (micro-scale) processes of a complex system expecting that the combination will correctly reproduce the macro-scale morphodynamics. This approach allows an in-depth description and simulation of the system [*Ruessink et al.* 2007a, *van Maanen et al.* 2008, *Castelle and Ruessink* 2011, *Daly et al.* 2014]. Faster, data-driven models are based on correlative properties between external conditions and observations. Although they can be used to hindcast, and partly forecast the evolution of a system, they do not provide insight into its internal behaviour [*Pape et al.* 2007, *Iglesias et al.* 2009, *de Alegria-Arzaburu et al.* 2010]. Semi-empirical models combine reduced computational costs with the possibility of describing a system as they are based on the physical formulation of a limited number of relevant processes involved in the system behaviour. Processes that are not included directly in the model formulation are then described by free coefficients computed from the correlative properties between external conditions and observations.

Semi-empirical models have been used extensively in hydrodynamics (for instance in wave breaking [*Battjes and Stive* 1985], wave dissipation [*Ardhuin et al.* 2010], bed shear stress [*Soulsby* 1995] and sediment transport [*Bagnold* 1963, *Bailard* 1981, *Soulsby* 1997, *van Rijn* 2007] formulations) and have also been applied to shoreline and sandbar morphodynamics. As an example, *Yates et al.* [2009; 2011] proposed a model in which an equilibrium shoreline position was linearly related to the incident wave energy and successfully described the shoreline cross-shore migration at several Torrey Pines Beach transects (South California, USA). *Plant et al.* [1999] used similarly a simple model relating the equilibrium cross-shore location of a sandbar to the wave breakpoint [*Dean* 1973, *Dally* 1987] which explained 50 to 90 % of the local bathymetric variability. *Plant et al.* [2006] extended the wave breakpoint model to integrate the bar alongshore variability. This model showed the dynamic stability of a sandbar's cross-shore position and alongshore variability. *Splinter et al.* [2011] developed the model further by introducing an energy-based sediment transport formulation into the migration rate description and by modelling the sandbars alongshore variability growth as an instability depending on the wave period and the wave height as suggested by *van Enckevort et al.* [2004], *Calvete et al.* [2005] and *Garnier et al.* [2008].

Although sandbars have been observed to rotate in the same way as shorelines [*Ojeda et al.* 2011,

van de Lageweg et al. 2013, *Bryan et al.* 2013], little work has been done on characterising and modelling this apparent rotation. Using pre-existing semi-empirical models developed for sandbar migration [*Splinter et al.* 2011, *van de Lageweg et al.* 2013] together with 7 years of barline position data obtained from video imagery techniques at Tairua Beach (NZ), the present study proposes first two models describing respectively the migration and the rotation of a subtidal sandbar in an embayed beach environment. These models are then used to identify the key environmental parameters involved in the rotation process and to study critical aspects of the barline response such as its characteristic response time.

2.3. Study area

2.3.1. Geological characteristics

The data used in the present study was collected at Tairua Beach in the North Island of New Zealand. Tairua is located on the east coast of the Coromandel peninsula (Figure 2.1). It is one of the numerous embayed sandy beaches interrupting the rocky coast, that is dominated by features such as extinct volcanoes and eroded volcanic plugs. Tairua Beach is approximately 1.2 km long. The bay is delimited by a rocky headland at the north, Pumpkin Hill, and an extinct volcano at the south, Paku Hill. Shoe Island is located 3 km eastwards from the southern extremity of Tairua Beach and stretches from south to north over a distance of 1 km. The island causes significant wave shadowing in the area of Tairua Beach, especially during easterly and south-easterly conditions [*Bryan et al.* 2013].

Tairua Beach typically exhibits a single-barred profile showing a single dynamic longshore subtidal bar with two headland- and three to six additional rip channels [*Gallop et al.* 2011]. Therefore the embayed beach shows a mixed-behaviour of an open beach that remains significantly influenced by the headlands [*Castelle and Coco* 2012]. The upper shoreface is usually steep with an average slope of 0.2, whereas the subtidal bar is located on the less steep lower shoreface profile with an average slope of 0.02. The beach is composed of well-sorted medium sand with a mean grain size diameter of about 300 μm. The beach is microtidal with a tidal range between 1.2 and 2 m and is generally exposed to north-easterly to easterly waves. In deep water, offshore of Tairua, the mean significant wave height is 1.4 m and can reach 6 m during storm conditions [*Smith and Bryan* 2007]. Similar to the other beaches in this part of the bay, Tairua is subject to successive progradation and retreat of its shoreline as well as rotation events [*van de Lageweg et al.* 2013, *Bryan et al.* 2013] and is classified as intermediate according to *Wright and Short* [1984].

2.3.2. Barline data

Morphological data has been derived from video imagery. The Cam-Era network installed by the National Institute of Water and Atmospheric Research (NIWA) is composed of 9 computer-controlled cameras monitoring 5 beaches over New Zealand. One camera has been installed on Paku Hill in 1998 at the southern extremity of Tairua Beach (Figure 2.1).

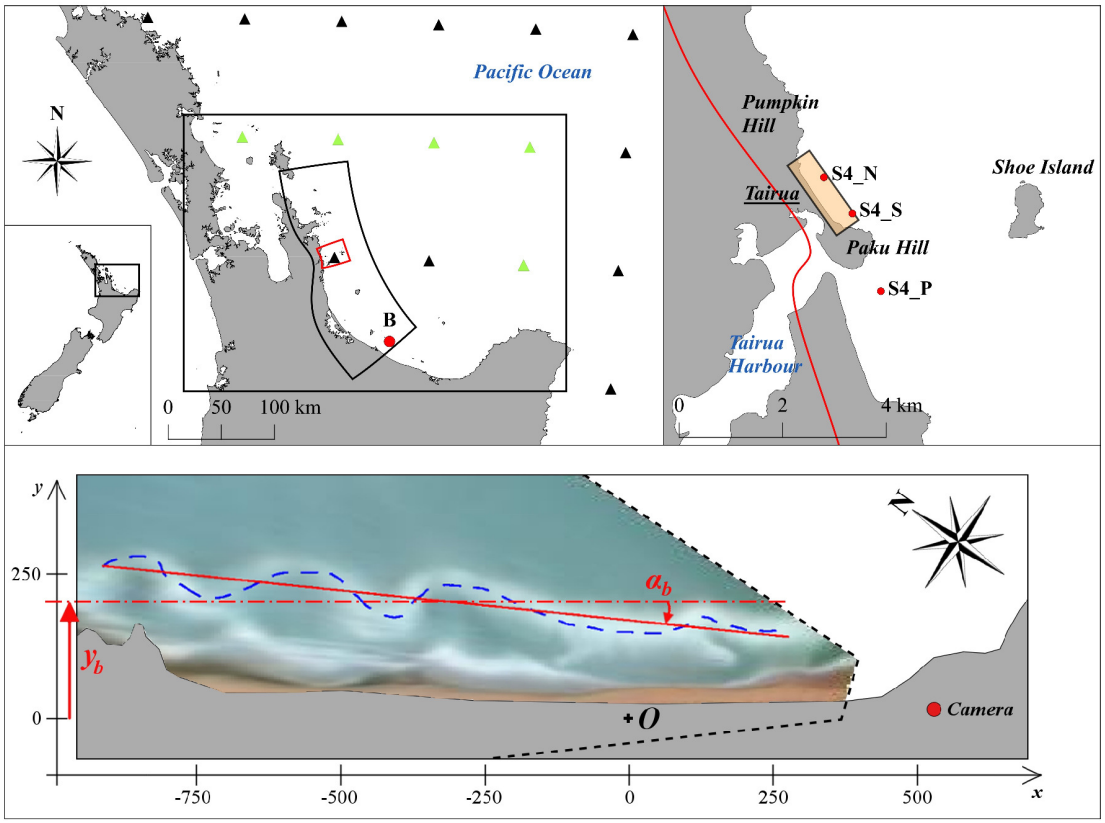

Figure 2.1.: *Upper panels: Location of Tairua in New Zealand North Island. Left: Detail of the Bay of Plenty with black and red enclosures corresponding to the SWAN wave model grids extent. Triangles represent the available locations of WW3 hindcasts. Green triangles display the locations used in the SWAN wave model.* ***B*** *is the location of the wave buoy maintained by the Bay of Plenty Regional Council. Right: Vicinity of Tairua Beach. The red line represents the extent of the grid used in the SWAN model.* ***S4_N****,* ***S4_S*** *and* ***S4_P*** *are the locations of the three instruments measuring the local wave characteristics at 8 m depth in 2011. The yellow area with black surrounding shows the area of study presented in the lower panel. Lower panel: georectified image of Tairua Beach (19th of December 2000) in local reference frame (origin O). The blue dashed line represents the digitized barline, the red solid line its linear regression and the red dot-dashed line its alongshore averaged cross-shore position y_b. The angle between the average shoreline orientation (angle 0) and the barline is represented by α_b. The red filled circle displays the location of the camera and the black dashed line the field of view of the camera.*

Seven years of video images captured between 1999 and 2006 were used in the present study. 600 images were averaged over a period of 15 minutes every hour during daylight. The video images were georectified over a 0.5 x 0.5 m grid following the procedure described in *Heikkila and Silven* [1997]. When wave breaking is observed at the location of the bar crest, a corresponding high intensity line can be observed and extracted from the time-averaged images [*Lippmann and Holman* 1990, *Ruessink et al.* 2007b]. The barlines have been extracted by fitting a second-order polynomial function to the pixel intensity along each cross-shore transect to reach subgrid accuracy and minimise the noise as described in *van de Lageweg et al.* [2013]. In order to obtain a good

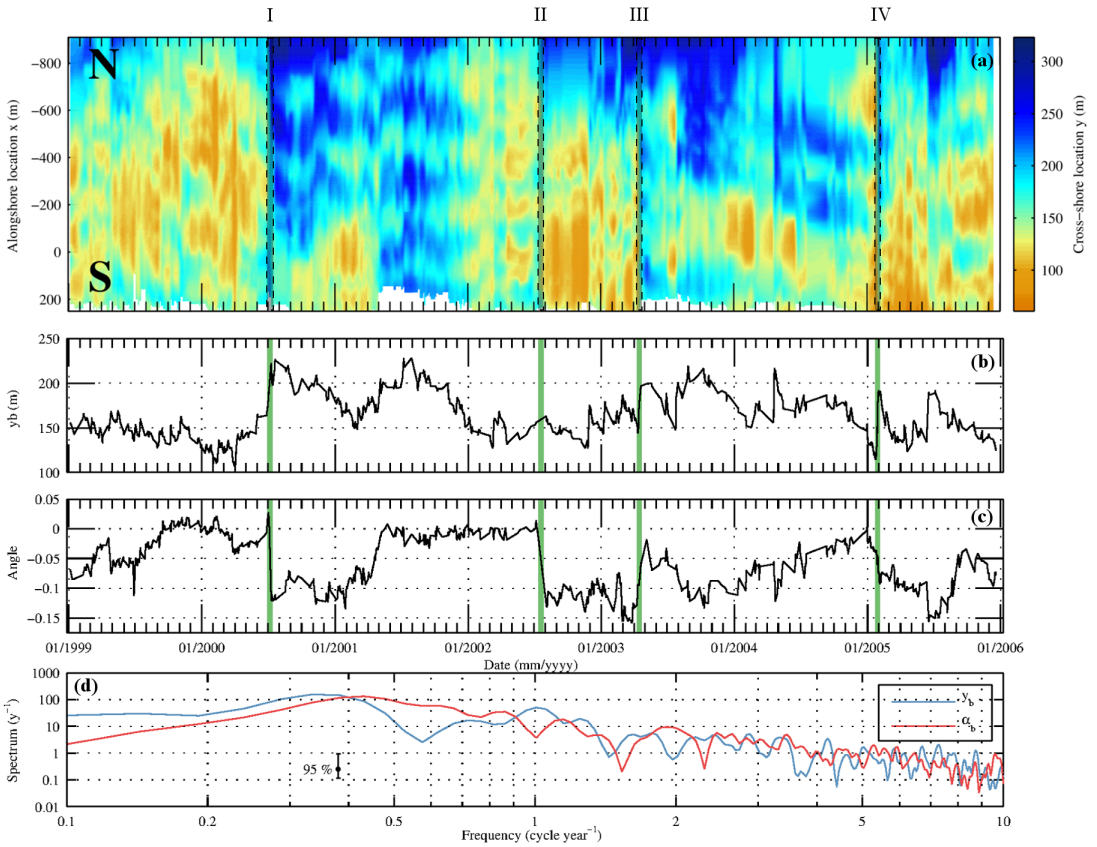

Figure 2.2.: *Barline measured locations (colorscale in metres) as a function of time and alongshore position (a), corresponding barline mean cross-shore position (b) and orientation (c) between 1999 and 2006. Erosion and rotation events I, II, III and IV are represented by the gray (panel (a)) and green (panels (b) and (c)) shaded areas. Panel (d) presents the Lomb-Scargle normalised spectrum of the cross-shore position and orientation for 1999-2006 computed using 8 DOFs (the 95 % confidence interval is given by the error bar). Blue: cross-shore position. Red: Orientation.*

representation of the barline all along the shore, only low tide images were retained and those where the wave height was insufficient to observe breaking over the bar were manually excluded from the dataset. No bathymetric data was available at the time of the measurements, therefore the cross-shore accuracy Δ_{y_b} of the barline cross-shore position was evaluated according to *van Enckevort and Ruessink* [2001] and *Ruessink et al.* [2009]. In the first study, they found standard deviations between the image-based and measured bar crests of 9.5 m and 8.3 m for all images and images selected at low tide respectively. In *Ruessink et al.* [2009], a deviation of 10 to 15 m seawards per lower metre of tidal level has been found. In the present case, low tide values range from -1 to -0.5 m below mean sea level, corresponding to a possible deviation of 7.5 m, similar to the results of *van Enckevort and Ruessink* [2001]. Therefore, a standard deviation $\Delta_{y_b} = 10$ m is considered to be here a conservative evaluation of the error in the measured cross-shore position of the bar crest. An example of a digitized barline is presented in Figure 2.1.

The evolution of the barline profile over 7 years is shown in Figure 2.2. The position is expressed

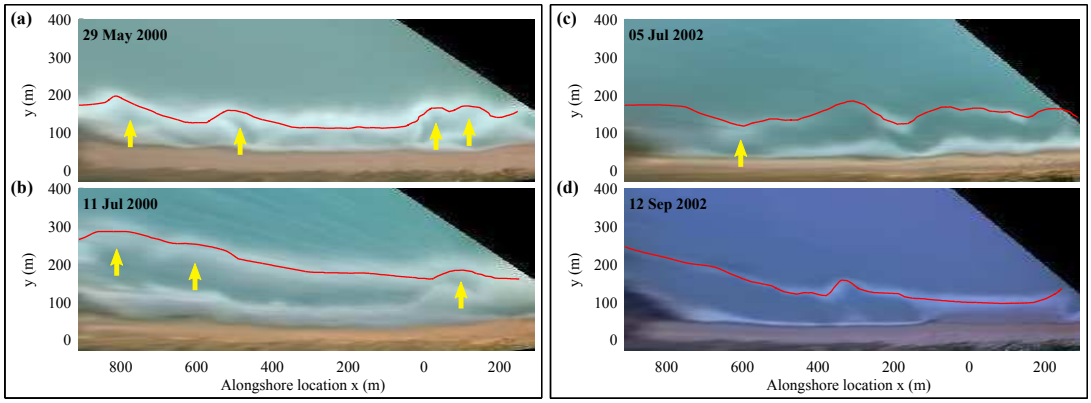

Figure 2.3.: *Barlines (red lines) displayed on corresponding georectified images. (a) and (b) are the barline locations before and after the storm events of June-July 2000 (Event I). (c) and (d) are the barline locations before and after the storm events of July 2002 (Event II). Yellow arrows indicate migrating and merging rip channels in (a) and (b). In (c), the yellow arrow shows a bar horn that cannot be observed two months later in (d).*

in a local reference frame with the origin located at the south end of the beach on the foredune and the x-axis parallel to the 7-year averaged coastline orientation, pointing southwards (see Figure 2.1). Different alongshore shapes are observed such as curved shapes (June 1999, October 2003), rhythmic shapes (January 1999, January to April 2002) or quasi uniform shapes (February 2002, February 2004). Significant seaward migration events can be observed in the dataset (July 2000 (Event I), April 2003 (Event III) and January 2005 (Event IV) in Figure 2.2), accompanied by a straightening of the barline. In addition, the data shows for Event I and IV that the barline cross-shore position varies more at the north of the beach than at the south. These two events of seaward migration therefore also resulted in an apparent clockwise rotation of the barline. On the contrary, a counter-clockwise rotation occurred with the seaward migration of the bar during Event III.

Barline rotation can also occur without any significant overall migration of the barline. The storm-induced rotation of June-July 2000 (Event I) is compared to the rotation observed in July 2002 (Event II, see the georectified images in Figure 2.3). During Event I, the alongshore averaged cross-shore position of the bar evolves seawards. The bar becomes clearly oblique due to the emphasis of the seaward migration at the north of the beach. In Event II, the alongshore-averaged cross-shore position of the bar remains approximately constant. However the southern (northern) extremity shifted shorewards (seawards) respectively. This event corresponds to a pivotal rotation around the central area of the beach.

These two events also show that barline rotation does not result from a migration restricted to the bar extremities, but rather corresponds to a large scale reorientation of the barline. Small features (O(100 m)) associated with rip channels have a limited impact on rotation. Between May and July 2000, the two systems of rip channels at the south and north of the bay followed the rotation and eventually merged at the southern extremity (see arrows in panels (a) and (b) of Figure 2.3). In July 2002, the bar horn at the north vanished during the rotation (see arrow in panel (c) of Figure 2.3).

Table 2.1.: *Barline minimum, maximum and standard deviation for five overlapping 3-year long time periods.*

Time period	$y_{b,min}$	$y_{b,max}$	σ_{y_b}	$\alpha_{b,min}$	$\alpha_{b,max}$	σ_{α_b}
1999-2002	107	228	29	-0.13	0.027	0.041
2000-2003	107	228	29	-0.14	0.027	0.047
2001-2004	127	228	24	-0.16	0.014	0.048
2002-2005	127	219	20	-0.16	0.013	0.043
2003-2006	115	219	21	-0.16	0.002	0.036

Similarly these small scale features have limited impact on migration events although they can show some persistence (for instance three barline horns can be observed before and after the seaward migration event of April 2004 in the upper panel of Figure 2.2). Bar crescentic features are likely to grow during accretionary events (July 2001 to February 2002) and their amplitude can influence the alongshore averaged cross-shore position of the bar. For example, their amplitude increased in April 2002 and then decreased until the end of June (see in Figure 2.2, panel (a), just before event II). It is also noticeable that the bar bays did not migrate significantly during this process, which means that the variations of small scale features amplitude did not occur symmetrically compared to the initial alongshore-averaged cross-shore position of the barline. Therefore this event appears here as an apparent shoreward migration of the bar in April followed by a progressive retreat until the end of June (panel (b)). Similar observations concerning the straightening of nearshore sandbars without any significant migration of their bays have been made by *Almar et al.* [2010]. These variations in the alongshore-averaged cross-shore position of the sandbar are limited to half the cross-shore extension of small scale features and are not considered in the present study.

The limited influence of small scale features on the large scale bar morphology suggests to reduce the barline description to two characteristic parameters, its alongshore averaged cross-shore position y_b and its orientation α_b (see lower panel in Figure 2.1). These are obtained by computing the alongshore trend of each barline profile (see Figure 2.1) and are presented in Figure 2.2 with their respective Lomb-Scargle spectrum [*Press et al.* 1992].

According to the two spectra, the amplitude of the cross-shore migration and rotation of the barline are both dominated by interannual variability. The cross-shore position of the bar exhibits large scale triennial events whereas the barline orientation signal is dominated by biennial frequencies. Such frequencies have already been observed in the morphodynamics of South Western Pacific beaches [*Clarke and Eliot* 1982, *Eliot and Clarke* 1982, *Clarke and Eliot* 1988]. The cross-shore location and orientation of the barline also exhibit significant amounts of variability at higher frequencies, with significant peaks in the annual and semiannual ranges for the position and the orientation of the barline respectively.

The angle and the cross-shore position of the barline are weakly negatively correlated ($r = -0.25 \pm 0.07$) meaning that offshore migrations are potentially accompanied by a clockwise rotation of the barline (for example during event I in June-July 2000) and vice-versa (October 2003 until December 2004) (Figure 2.2). The weakness of the correlation can be related to the fact that y_b and α_b are described by different frequency components in the spectral space. Therefore no significant correlations could be found in the cross-correlation spectrum (compared to the 95 % level of 1000 cross-spectra computations using a red noise signal instead of the migration signal, not presented

here). The lack of correlation between y_b and α_b tends to support the hypothesis that the migration and the rotation of the barline are either weakly coupled or not coupled, as suggested by the previous examples in Figure 2.3.

The weak dependency of the barline orientation on small scale morphological features and its cross-shore position advocates for the validity of using this parameter as a main descriptor of the bar state in an embayed environment. In order to confirm this, we present in this paper a semi-empirical model relating the evolution of the barline angle α_b to the incident wave climate at Tairua (see section 2.4).

2.3.3. Waves at Tairua Beach

There are only few wave measurements in the direct vicinity of Tairua Beach. The Bay of Plenty Regional Council (BoPRC) maintains one wave buoy in the Bay of Plenty (see **B** on Figure 2.1). This wave buoy was installed in 2003 13 km off Pukehina Beach, 6 km southeast of Motiti Island, which is 90 km south of Tairua. In addition, waves were observed over three 6-week periods in March-April, August-September and October-November 2011 at three locations in the vicinity of Tairua Beach, at 8 m depth (see **S4_N**, **S4_S** and **S4_P** on Figure 2.1).

A suitable continuous source of wave data offshore of Tairua is currently the global WaveWatch III (WW3) Ocean Wave hindcast model of the National Oceanic and Atmospheric Administration (NOAA), where the main driver is the new Climate Forecast System Reanalysis (CFSR) homogeneous dataset of hourly 0.5° spatial resolution winds from the National Centres for Environmental Prediction (NCEP). Geographical locations of the WW3 hindcasts nodes are displayed in Figure 2.1.

Modelling sandbar morphodynamics at Tairua Beach requires high temporal and spatial resolution of the wave field in order to compute the variations of the wave height along the shore, likely to be involved in the local bar morphodynamics [*Bryan et al.* 2013]. A regional non-stationary wave model was set-up using SWAN modelling system [*Booij et al.* 1999] to include the local propagation of time-varying spectral wave conditions at five nodes of the global WW3 model area nearest to the boundaries of the SWAN model (Figure 2.1). The wave spectrum bulk parameters as well as its spectral peaks are available every three hours at each node. 2D spectra are then reconstructed by using a superposition of JONSWAP shaped spectra corresponding to each spectral peak and by normalising the overall obtained spectrum by the corresponding total wave energy. The formulation of *Longuet-Higgins* [1963] has been used for the directional spreading. To account for the wind-generated waves inside the Bay of Plenty, the NCEP wind fields have been used as surface boundary conditions in the SWAN model.

The model uses three nested grids with increasing spatial resolution (Figure 2.1). The largest grid is a rectangular grid with 5 km square grid cells covering the entire Bay of Plenty. The finest grid is a rectilinear grid extending 10 km south and north of Tairua and 25 km offshore, accounting for the influence of the offshore islands on the wave propagation, reaching a resolution of 120 m alongshore and 75 m cross-shore over Tairua Beach. The non-stationary model time step was of 30 min and wave characteristics used in the present paper were generated every 3 hours at 8 m depth.

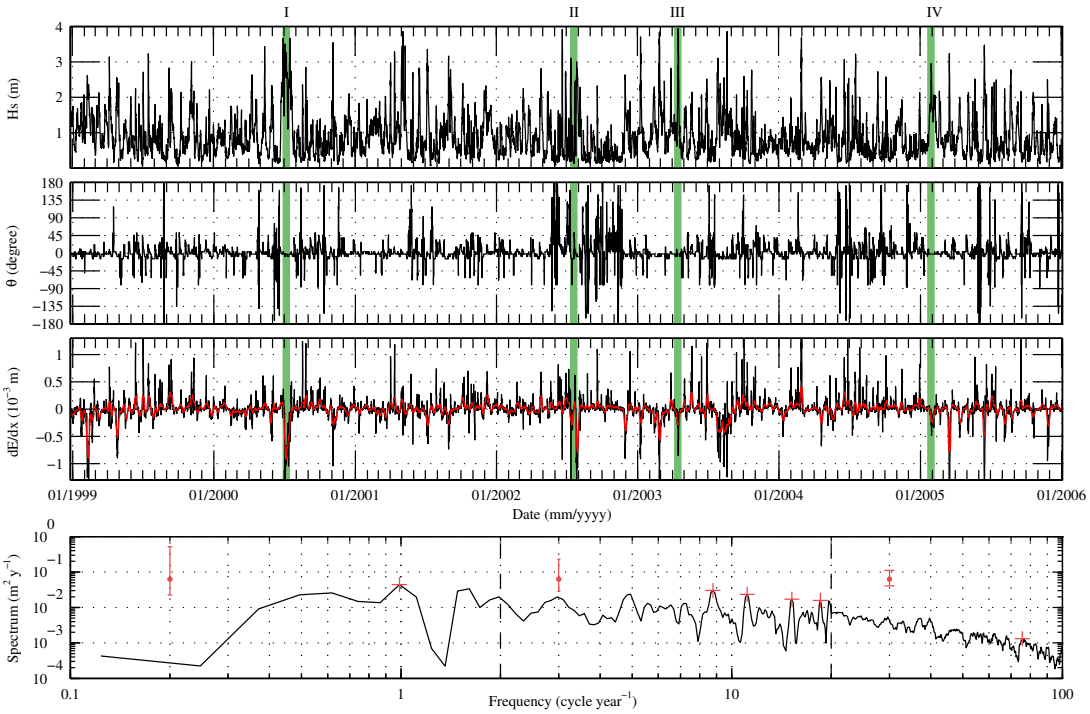

Figure 2.4.: *Wave conditions modelled at the centre of Tairua Beach (8 m depth) between 1999 and 2006. Top panel: significant wave height in metres. Second panel: incident wave angle in degrees compared to the normal to the beach (positive angles indicate southward orientated waves). Third panel: Modelled (black line) and weekly-averaged (red line) alongshore wave energy gradient in metres. Erosion and rotation events I, II, III and IV are represented by the green shaded areas Lower panel: wave spectrum between 1999 and 2006 with associated confidence interval using 4, 8 and 32 DOFs in the left, central and right sections delimited by the dashed lines respectively. Error bars indicate the 95 % confidence intervals and the red pluses the significant peaks.*

The SWAN model was calibrated using wave characteristics measured in 2011 by the wave buoy of the BoPRC. This resulted in increasing the simulated white capping dissipation. The model was then validated using the three locations in the vicinity of Tairua. In terms of wave height, the R^2 coefficients range from 0.51 to 0.83 at the three nearshore locations with a root mean square error (*RMSE*) between 7 and 15 cm. The variability of the mean period is better simulated at the BoPRC buoy ($R^2 = 0.75$) than at Tairua (R^2 between 0.02 and 0.20). However, the *RMSE* remains small, between 0.9 and 2.1 s (time-averaged value of 7.2 s). The peak wave angle is only available at the BoPRC buoy. The R^2 coefficient is 0.27 for all wave conditions and increases to 0.68 for wave heights above 2 m. Modelled Pacific storms occurrences and peak wave heights are in good agreement with in-situ measurements.

Figure 2.4 shows the significant wave height, peak wave angle, alongshore wave energy gradient and significant wave height power spectrum over 7 years simulated at the centre of Tairua Beach at 8 m depth. The mean significant wave height is 0.85 m. 5 % of the wave heights reach values above 2 m with a maximum of 3.9 m. Compared to the beach main orientation over the 7 years, the

mean incident wave angle is 2°, showing a standard deviation of 30°. The alongshore wave energy gradient is computed by extracting the wave energy at the south and the north of the beach and dividing the difference by the distance separating the two points (1200 m). The difference reaches values of up to 3 m^2 over the beach length. In terms of significant wave height the difference ranges from -0.52 to 0.60 m. In the following the wave energy gradient is not used directly, instead its weekly-average is prefered (red line in third panel of Figure 2.4). The wave climate is dominated by interannual fluctuations. Significant components of the wave climate were also found at the monthly scale.

2.4. Methodology

2.4.1. Bar cross-shore migration model

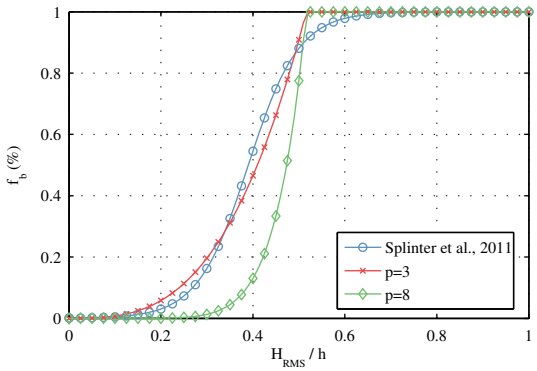

Figure 2.5.: *Blue: fraction of wave breaking used in Splinter et al. [2011]. Red: damping factor f_b using p=3. Green: damping factor f_b using p=8.*

In the present work, the method used to verify the concept of barline rotation is based on the quality of a semi-empirical model that is able to hindcast and forecast observations of the Tairua Beach barline rotation. The development of this model, presented in the next section, builds on a formulation describing the migration of a subtidal bar. The present barline migration model is an extension of the shoreline migration model described in *Yates et al.* [2009] as this model is already able to explain 39 % of the overall variability of the Tairua barline [*van de Lageweg et al.* 2013]. The model of *Splinter et al.* [2011] developed for barlines and likely to be more accurate, cannot be reliably implemented in the present case because the coupling between the sandbar cross-shore position and its alongshore variability requires good knowledge of the incident wave periods which are not computed as accurately as the incident wave heights and directions in the present wave model.

Yates et al. [2009] assume that an equilibrium incident wave energy depends linearly on the location of the shoreline. Here, it is similarly assumed that an equilibrium incident wave energy corresponds to a specific location of the barline, in agreement with the breaking point hypothesis of *Dean* [1973]

and *Dally* [1987]. Assuming a linear relationship, the relation is:

$$E_{eq,b} = a_b y_b + b_b \tag{2.1}$$

with $E_{eq,b}$ the equilibrium energy, y_b the barline cross-shore position and a_b and b_b are the linear relation coefficients. The formulation of *Plant et al.* [1999] is similar but uses the root mean square wave height instead of the wave energy. Equation 2.1 appears therefore as a linearisation of the breakpoint hypothesis in the present paper since this hypothesis supposes a quadratic relationship between $E_{eq,b}$ and y_b for a constant beach slope.

The next hypothesis of *Yates et al.* [2009] is to relate the migration rate of the shoreline to the difference between the instantaneous incident wave energy and its equilibrium value related to the actual position of the shoreline. In order to account for the increase of sediment transport related to higher wave energy, this term is multiplied by the square root of the incident wave energy:

$$\frac{\partial y_b}{\partial t} = C_{y_b} \sqrt{E}(E - E_{eq,b}) \tag{2.2}$$

where E is the instantaneous incident wave energy, assimilated here to the square of the significant wave height H_s and C_{y_b} is a free parameter of the model that can be later calibrated such as a_b and b_b.

Figure 2.2 shows that offshore migration occurs much more quickly than onshore migration. In order to account for similar effects on shoreline migration, *Yates et al.* [2009] multiplied the right hand side of Equation 2.2 by coefficients C_+ and C_- to calibrate separately for the shoreline progradation and the retreat events as they showed different response times. In the present study, rather than calibrating separately the shoreward and seaward migration of the bar, one free constant parameter C_{y_b} allows for model calibration and the ratio between the offshore significant wave height H_s over the breaking wave height at the bar crest location H_b is used to enhance or damp the mobility of the bar. When waves break offshore of the bar ($H_s > H_b$ and $E > E_{eq,b}$), the bar is highly mobile and migrates offshore towards the breaking point. During calm conditions, waves break onshore of the bar ($H_s < H_b$ and $E < E_{eq,b}$) and the bar migrates slowly towards the shoreline. The right hand side of Equation 2.2 is therefore multiplied by a *damping factor* f_b which is the ratio of H_s over H_b elevated to the power p with a maximum value set to 1:

$$f_b(H_s, H_b) = \min\left(\left[\frac{H_s}{H_b}\right]^p, 1\right) \tag{2.3}$$

The damping factor f_b can be directly compared to the fraction of breaking waves used in *Splinter et al.* [2011] (see the comparison for different values of p in Figure 2.5). Indeed in both cases, the barline migration rate is proportional either to f_b in the present formulation or to the fraction of breaking waves (parameter b_b in the work of *Splinter et al.* [2011]). However, f_b is suggested here as a more general morphodynamic damping factor and cannot be directly related to the fraction of breaking curve since little is known about this curve at Tairua. The exponent p has been manually calibrated to a value of 8. The best fit with the sigmoid curve proposed by *Splinter et al.* [2011] is found for $p = 3$ (see Figure 2.5). However this choice led to an overestimation of the shoreward migration of the bar under low wave conditions and to an underestimation of the most seaward

locations of the bar.

The computation of the breaking wave height H_b requires the water depth over the bar crest to be known. The derivation of the depth h_{y_b} at the bar crest and the breaking wave height H_b follows:

$$h_{y_b} = \beta(y_b - < y_s >) - h_{bar}, \tag{2.4}$$

$$H_b = \gamma h_{y_b} \tag{2.5}$$

with $< y_s >$ time-averaged alongshore-averaged shoreline position obtained from the 7-year dataset (over 7 years, $< y_s > = 37$ m) and γ is the breaker parameter with a value of 0.73 [*Battjes and Stive* 1985]. β is the average slope of the beach in the area where the bar is active and has been set to 0.023 according to beach profiles measured in 2011 (eight 150 m-spaced and 600 m long cross-shore transects measured in April, May and July 2011). h_{bar} stands for a constant height of the sandbar over the average profile. A value of 1 m has been selected based on the beach profile measurements. Bar cross-shore shape considerations used in *Ruessink et al.* [2007a] and *Splinter et al.* [2011] have been ignored here. Since the model described by Equation 2.2 can be applied by definition to every cross-section of the beach, in order to describe the alongshore-averaged migration of the barline the model is also alongshore-averaged (see appendix A.1). The averaging follows the following assumptions:

1. a_b is symmetric in the embayment
2. E and y_b can be linearised with an alongshore-averaged value $\overline{E}$ and $\overline{y_b}$ and an alongshore-varying value $\tilde{E}$ and $\tilde{y_b}$
3. $\tilde{E} << \overline{E}$
4. f_b is uniform along the beach, using $f_b(\overline{H_s}, \overline{H_b})$

The final formulation for the barline migration model is then:

$$\frac{d\overline{y_b}}{dt} = C_{y_b}\sqrt{\overline{E}}(\overline{E} - (\overline{a_b}\,\overline{y_b} + \overline{b_b}))f_b(\overline{H_s}, \overline{H_b}) \tag{2.6}$$

2.4.2. Barline rotation model

In order to explain the rotation of the embayed barline, we suppose here that this process is induced by the adaptation of the cross-shore beach profiles to alongshore varying wave energy conditions. The rotation model was initially implemented by applying the cross-shore migration model along different alongshore sections of the beach. A similar approach here is to differentiate and average the cross-shore model formulation Equation 2.2 along the alongshore dimension x (see appendix A.2). This means that by definition, the model only accounts for cross-shore processes and computes how the alongshore variation of these processes affects the barline migration and translates into a

rotation of the barline. Differentiation and alongshore-averaging leads to:

$$\overline{\frac{\partial}{\partial x}\left(\frac{\partial y_b}{\partial t}\right)} = \overline{\frac{\partial}{\partial t}\left(\frac{\partial y_b}{\partial x}\right)} = \overline{\frac{d\alpha_b}{dt}} = \frac{d\alpha_b}{dt}, \tag{2.7}$$

$$\begin{aligned}\frac{d\alpha_b}{dt} &= C_{\alpha_b}\Big[\sqrt{\overline{E}}\left(\frac{\partial \tilde{E}}{\partial x} - \delta\,\overline{a_b}(\alpha_b - \alpha_0)\right) \\ &\quad + \frac{1}{2\sqrt{\overline{E}}}\frac{\partial \tilde{E}}{\partial x}\left(\overline{E} - \overline{a_b}\,\overline{y_b} - \overline{b_b}\right)\Big] f_b(\overline{H_s}, \overline{H_b}),\end{aligned} \tag{2.8}$$

where C_{α_b}, δ and α_0 are free parameters of the model. C_{α_b} is used for the overall calibration of the rotation rate. α_0 is used to let the model find the best value of α_b corresponding to a zero value of the alongshore wave energy gradient. δ is a parameter allowing factors a_b and b_b defining the equilibrium energy $E_{eq,b}$ (see Equation 2.1) to vary in the alongshore dimension (see appendix A.2). In the following, symbols $\tilde{}$ and $\bar{}$ are not represented to simplify the notation.

2.4.3. Model calibration and performance evaluation

Both models (migration: Equation 2.6 and rotation: Equation 2.8) are evaluated by comparing their outcomes with the 7 years of observations. Three parameters have been selected to assess the models performance: the root mean square error (*RMSE*), the coefficient of determination (R^2) and the Brier skill score (*Bss*) to allow the comparison with the existing literature.

$$RMSE = \sqrt{<(S_{b,c} - S_{b,m})^2>}, \tag{2.9}$$

$$R^2 = \left[\frac{<(S_{b,c} - <S_{b,c}>)(S_{b,m} - <S_{b,c}>)>}{\sigma_{S_{b,c}}\sigma_{S_{b,m}}}\right]^2, \tag{2.10}$$

$$Bss = 1 - \frac{<(S_{b,c} - S_{b,m})^2>}{<(S_{b,m} - <S_{b,m}>)^2>} \tag{2.11}$$

where S_b stands for the considered timeseries y_b or α_b, σ is the standard deviation, subscripts c and m stand for computed and measured signals respectively and the angled brackets stand for time averaging. First the migration and rotation models are evaluated on their ability to hindcast the full 7-year time period of barline observations. To assure the robustness of the models and the reliability of their free parameters, they are then evaluated on five overlapping 3-year time periods of observations. Finally, the models are trained on time periods varying from 1 to 4 years and their forecasting abilities are assessed by comparing their outcomes with observations of the corresponding following 2-year time periods.

The choice of the five time segments mentioned in the previous paragraph is motivated by the fact that the barline characteristics in terms of cross-shore position and angle are remarkably stable from one time period to another. Table 2.1 gives the minimum, maximum and standard deviation of the cross-shore position y_b and the angle α_b of the barline during these five periods. The overall ampli-

tude of the bar fluctuations is remarkably stable around 100 m even if the bar did not migrate after December 2000 as far onshore as before. The standard deviation of the barline is similar for all time periods and varies between 20 and 30 m. The stability of these characteristics can be related to the dominating triennial fluctuations that are covered over a 3-year time period. Similar observations can be made for the barline angle with an amplitude of the fluctuations stable around 0.15 (180 m over 1.2 km). Noticeably, during the five time periods, the cross-shore distance between the bar extremities has therefore an amplitude of almost twice the distance between the most shoreward and seaward alongshore averaged locations of the entire barline, confirming that the bar angle is a relevant parameter to describe the bar state.

All numerical integrations are performed using a 4-th order Runge-Kutta scheme, starting from known initial cross-shore position and angle of the barline observations. The integration schemes use a varying time step ranging from 1 hour up to 2 days in order to obtain a sufficient accuracy. Errors are evaluated by comparing the model outcomes obtained using 4-th and 5-th order schemes [*Dormand and Prince* 1980]. The final mean error is of -0.7 m for the bar location and 3×10^{-3} (3.6 m over 1.2 km) for the bar angle compared to higher-order schemes outcomes for which decreasing the error criteria did not influence the results of the integration anymore. The calibration of the model is based on the minimization of *RMSE* between measured and computed values (Equation 2.9) and performed in two stages. First the cross-shore migration model is calibrated, defining the optimal values of C_{y_b}, a_b and b_b and computing the barline position y_b. Then these results are used in the rotation model and the optimal values of C_{α_b}, δ and α_0 are computed. This is allowed by the fact that Equations 2.2 and 2.8 are only partially coupled. As mentioned in *Yates et al.* [2009], gradient-based methods cannot be used due to the occurrence of numerous local maxima over the spaces defined by the three free coefficients of each model. Attempts to optimize the model using simulated annealing [*Kirkpatrick et al.* 1983], genetic algorithm [*Goldberg* 1989] and particle swarm algorithm [*Ebbesen et al.* 2012] have been performed. The latter offered the best compromise between convergence and computation speed and has therefore been used in this study.

2.5. Results

2.5.1. Hindcasts

2.5.1.1. 7-year dataset

The migration and rotation models were first calibrated on the whole 7-year long dataset. Measurements and model results for y_b and α_b are presented in Figure 2.6 (panels (a, b)). Skill scores are presented in Table 2.2.

In comparison to the model of *Yates et al.* [2009] which explained 39 % of the barline migration variability [*van de Lageweg et al.* 2013], the introduction of the morphodynamic damping factor f_b allowed the model to explain 73 % of the barline migration variability, which is comparable to shoreline model skills (61 to 94 % in *Yates et al.* [2009]) and barline model skills on short term periods (from 70 to 80 % in *Plant et al.* [2006] on 2-month observations, 49 % in *Splinter et al.* [2011] on seven observation periods ranging from 3 weeks to 6 months). The root mean square

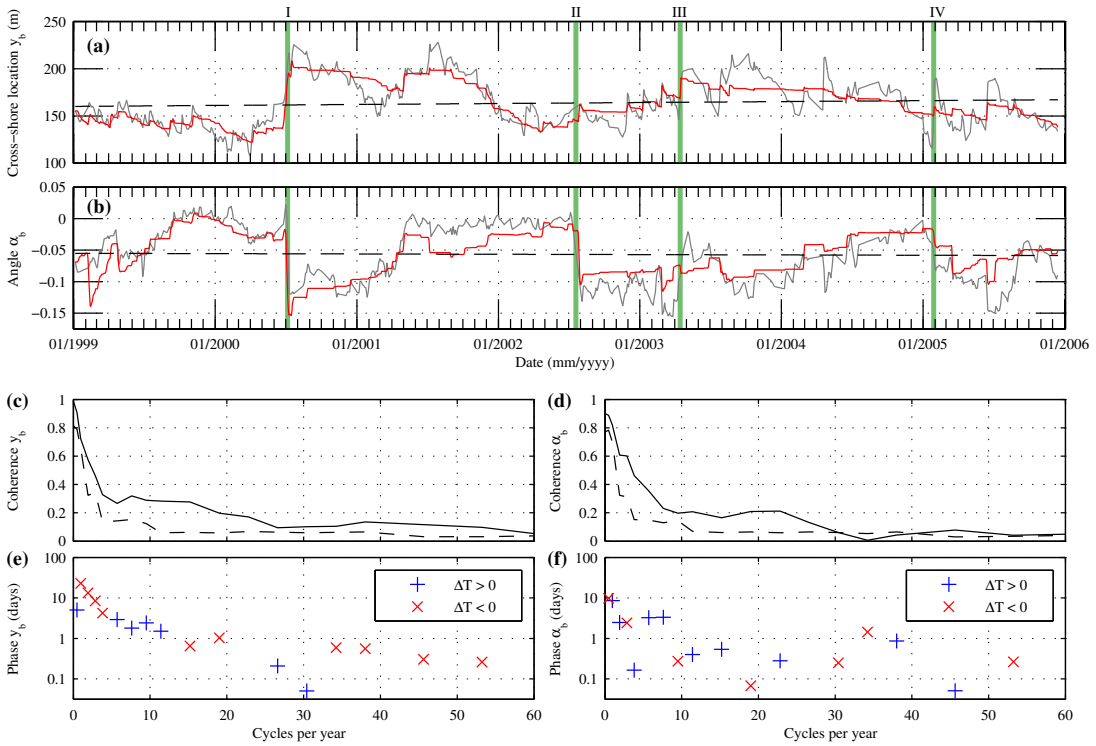

Figure 2.6.: *Panels (a, b): Modelled (red) cross-shore alongshore averaged barline position y_b (a) and barline angle α_b (b) with calibration performed using 7 years of measurements (represented in gray). Erosion and rotation events I, II, III and IV are represented by the green shaded areas. Panels (c, d): Coherence between modelled and measured signals (solid black) and 95 % significance level compared to red noise (dashed black) for y_b (c) and α_b (d). Panels (e, f): Phase shift in days between modelled and measured signals for y_b (e) and α_b (f). Blue pluses and red crosses stand for positive and negative time delays respectively.*

error, $RMSE_{y_b}$ is 12.97 m, corresponding to 0.52 standard deviation of the cross-shore location signal (see Table 2.2).

The rotation model accounts for 67 % of the overall barline angle variability and the root mean square error, $RMSE_{\alpha_b}$ (2.5×10^{-2} or 30 m over 1.2 km), corresponds to 0.58 standard deviation of the angle signal.

The models are able to reproduce quantitatively the short time scale events of large amplitude as well as the long time scale events (more than one year). The firsts are illustrated by the combined clockwise rotation and offshore migration of July 2000 (Event I) and the pivotal rotation event of July 2002 (Event II). The latter includes the slow onshore migration periods of January 1999 - April 2000, August 2001 - March 2002 and the slow counter-clockwise rotation events of April - November 1999, July 2000 - May 2001 and October 2003 - January 2005.

Despite the good agreement between the simulated and measured barline position and orientation, the variability and amplitude of short time scale events is often underestimated. Regarding the

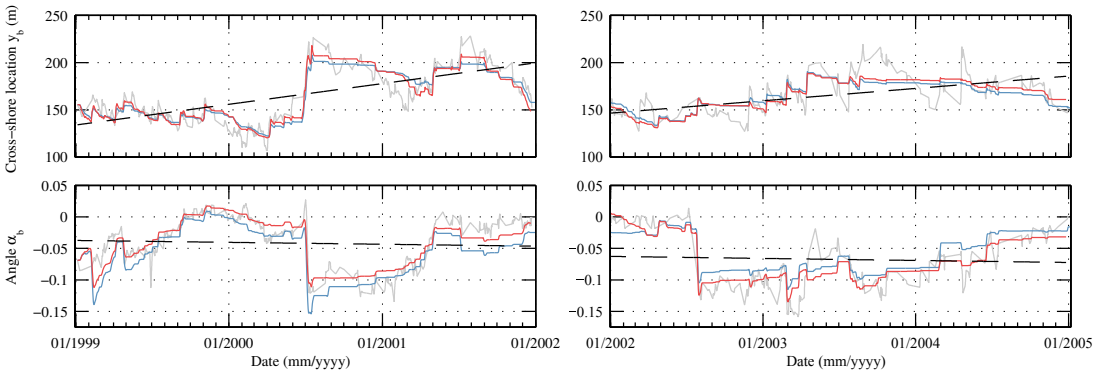

Figure 2.7.: *Left: 1999-2002. Right: 2002-2005. Top: cross-shore position y_b. Bottom: barline angle α_b. Gray: observations. Blue: 7-years hindcasts for period 1999-2006. Red: 3-years hindcasts for period 1999-2002 (left) and 2002-2006 (right). Dashed line: linear trends of the observations.*

cross-shore position of the bar, the modelled position follows the measured interannual fluctuations during the period March 2002 - December 2005, reproduces monthly variations in December 2003 - February 2004 but underestimates the offshore migrations of January and June 2005 and does not reproduce the offshore migrations of July 2003 and April 2004 (Event IV). Regarding the orientation of the bar, the counter-clockwise rotation event of April 2003 followed by a clockwise rotation of similar amplitude in August 2003 is largely underestimated in the model as well as the angle variations during the second half of 2005.

To quantitatively assess the quality of the models in simulating morphodynamic events on different time scales, the coherence and phase between the measured and modelled values for the barline cross-shore position and barline angle have been computed (see Figure 2.6, panels (c,d,e,f)). To evaluate the significance of the coherence, a thousand first order red noise time series have been generated for each of y_b and α_b. The determination of the significance level at 95 % follows *Thomson* [1990] and is usually used to assess the significance of climatic data spectral peaks [*Schulz and Mudelsee* 2002].

The coherence between measured and modelled signals (Figure 2.6, panels (c, d)) shows that the models account for more than 40 % of the barline cross-shore position and the barline angle fluc-

Table 2.2.: *Model skills for 7-years and five 3-years long time periods with calibrated cross-shore equilibrium parameters a_b and b_b.*

Time	$RMSE_{y_b}$	$R^2_{y_b}$	Bss_{y_b}	$RMSE_{\alpha_b}$	$R^2_{\alpha_b}$	Bss_{α_b}
1999-2006	13	0.73	0.73	0.025	0.67	0.66
1999-2002	11	0.87	0.87	0.017	0.82	0.82
2000-2003	12	0.82	0.81	0.020	0.81	0.81
2001-2004	14	0.72	0.69	0.022	0.80	0.80
2002-2005	13	0.60	0.59	0.019	0.81	0.80
2003-2006	14	0.55	0.55	0.022	0.63	0.63
Average	13	0.71	0.70	0.020	0.77	0.77

Table 2.3.: *Model coefficients for 7-years and five 3-years long time periods with calibration of the cross-shore equilibrium parameters a_b and b_b.*

Time	C_{y_b}	C_{α_b}	δ	a_b	b_b	α_0
1999-2006	0.52	9.6	0.059	0.061	-6.0	-0.028
1999-2002	0.76	7.0	0.056	0.066	-6.8	-0.013
2000-2003	0.54	12.3	0.052	0.065	-6.8	-0.015
2001-2004	0.43	15.8	0.042	0.060	-6.0	-0.011
2002-2005	0.51	11.1	0.056	0.058	-5.6	-0.037
2003-2006	0.61	11.6	0.054	0.063	-6.2	-0.045
Av. ± std	0.57 ± 0.13	11.5 ± 3.2	0.052 ± 0.006	0.062 ± 0.003	-6.3 ± 0.5	-0.024 ± 0.016

tuations for frequencies below 2.8 cy^{-1} (cycles per year) and 3.8 cy^{-1} respectively. In this range, the phase shifts between the modelled and measured values (Figure 2.6, panels (e, f)) vary from O(10 days) (yearly fluctuations) to O(1 day) (3 to 4-months fluctuations) for the bar migration. For the bar rotation, phase shifts remain below 10 days. The migration model mainly lags behind the data for interannual to seasonal fluctuations. The rotation model shows a complex behaviour where close frequency components are either delayed or ahead of the data. For fluctuations having a time period between 12 days and 4 months, the coherence signals of y_b and α_b take values below 0.4 but remain significant. Time shifts are below 5 days and for time periods below a month, they remain below 1.5 days.

These results confirm that both models show good performance in reproducing low frequency morphodynamic fluctuations (time periods longer than 3 to 4 months). Therefore they simulate a large amount of the overall variability of y_b and α_b since most of the variability of these signals is found in this range (see Figure 2.2). On shorter time scales, the models still produce significant outcomes, especially up to fortnightly time periods ($f < 26$ cy^{-1}, coherence around 0.2).

2.5.1.2. 3-year datasets

In order to assess the variability of the free parameters and the skill of the models, both the migration and rotation models were calibrated over five 3-year long data segments. The obtained skill scores and free parameters are presented in Tables 2.2 and 2.3 respectively.

Period 1999-2002 is characterised by large scale annual and interannual fluctuations that are well represented by the migration and rotation models. Therefore this time period obtains the highest skill for both models (see Table 2.2).

For the migration model, skill is on average similar to that of the full record (see Table 2.2). However the values of R^2 and *Bss* decrease for the last two periods. This can be related to the fact that contrary to the period 1999-2002, the cross-shore position during 2002-2006 exhibits large scale fluctuations on the timescale of O(1 month) superimposed on a very long term fluctuation with a characteristic time scale of several years. The model reproduces well this long term behaviour but fails to describe accurately the shorter ones (see Figure 2.7).

Except for the last time segment where the model does not reproduce accurately the amplitude of the angle fluctuations, the skills of the rotation model are excellent with R^2 and *Bss* values around

0.8 compared to 0.67 for the 7-year hindcast. These improvements are related to clear changes in the mean value of the simulated angle (see Figure 2.7), reflected by the adjustment of parameter α_0 between the three first and two last segments (see Table 2.3).

The robustness of the migration and rotation models is reflected by the stability of their free parameters over the five time periods (Table 2.3). Thereby, the values of C_{y_b}, a_b and b_b obtained for the 7-year hindcast differ within less than a standard deviation from the average of the values computed for the five 3-year segments. The same applies to parameters C_{α_b} and α_0 for the rotation model. The value of δ falls slightly above one standard deviation. In the 7-year simulation, the adaptation of α_0 induced a decreasing of the amplitude of the modelled bar angle fluctuations reflected by an increase of parameter δ.

As the models skills are comparable and the six free parameters remarkably stable for all runs, it can be observed in Figure 2.7 that using 3-year instead of 7-year time periods does not improve the performance of the model in simulating short period morphodynamic fluctuations. In agreement with the results of the coherence analysis in the previous section, this means that certain processes acting on short time scales are not included in the models formulations, such as the evolution of the alongshore variability linked to the incident wave period described in *Splinter et al.* [2011].

Interestingly, the ratio of $-b_b$ over a_b falls between 97 m and 105 m for the 3 and 7-year runs. This ratio corresponds to the asymptotic equilibrium position of the barline when the incident wave energy is zero (see Equation 2.1). In relation to the stability of a_b and b_b, this factor is also remarkably stable despite the difference of coverage of the barline position signal over the five time periods (see Table 2.1).

2.5.2. Forecasts

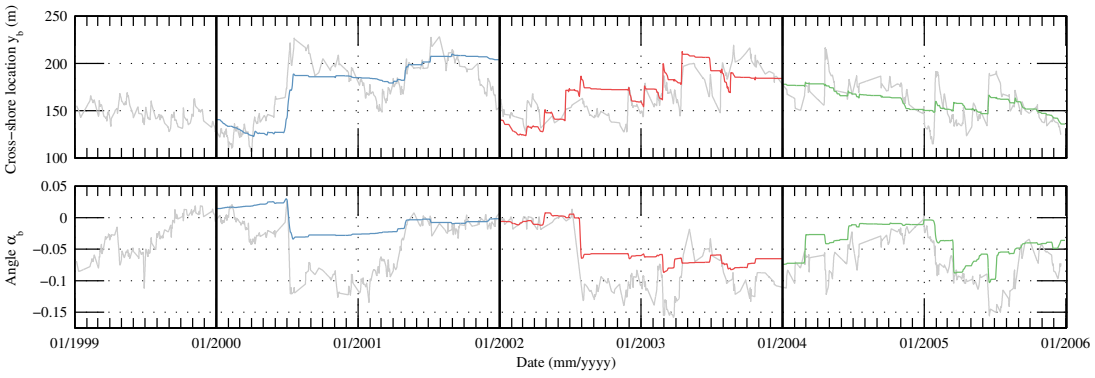

Figure 2.8.: *Top: Cross-shore alongshore averaged barline position y_b. Bottom: Barline angle α_b. Gray: observations. Colored: forecasts with 1-year training(blue), 3-year training (red) and 5-year training (green).*

To assess the ability of the models to simulate the cross-shore position and the angle of the barline during time periods when the barline state is unknown, four forecasting tests were performed using the 7-year dataset.

Table 2.4.: *Model skills for 2 years forecasts with increasing training periods.*

Training	$RMSE_{y_b}$	$R^2_{y_b}$	Bss_{y_b}	$RMSE_{\alpha_b}$	$R^2_{\alpha_b}$	Bss_{α_b}
1999-2000	18	0.66	0.82	0.049	0.62	-0.19
1999-2001	22	0.40	0.38	0.029	0.78	0.61
1999-2002	20	0.45	0.29	0.038	0.70	0.56
1999-2003	17	0.35	0.45	0.036	0.62	0.40
1999-2004	14	0.44	0.47	0.034	0.70	0.18

The models are calibrated on a time period (training period) where the forcing wave conditions and the barline state is known. Then the models are validated on the time period (evaluation period) following the training period. In the present paper, four different training periods of 1, 2, 3 and 4 years are considered and the evaluation period lasts two years. The models skills are presented in Table 2.4 and the results for three runs are plotted in Figure 2.8.

The Brier skill scores are positive for all the migration forecasts and for the rotation forecasts with training periods longer than 2 years. This results from the fact that the models are able to reproduce the 2-year trends of the barline position and angle during the evaluation periods.

Clockwise rotations (towards negative orientations) tend to be underestimated in the forecasts leading to lower *Bss* for the rotation model than for the bar migration one. However R^2 coefficients are significantly higher for the bar orientation (on average 0.68) than for its position (on average 0.46) indicating better qualitative simulation of rotation events despite counter-clockwise shifts and resulting underestimated amplitudes of rotation events.

2.6. Discussion

2.6.1. The concept of rotation applicable to embayed beach sandbars

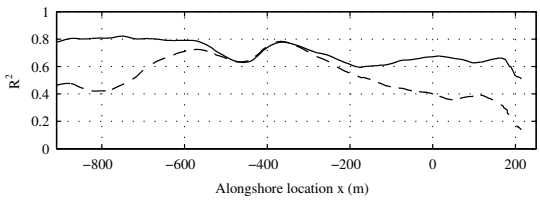

Figure 2.9.: *R^2 coefficient at every cross-shore transect of Tairua Beach between measured (Figure 2.2) and reduced 7-year barline profiles. Dashed line: barline profile reduced to its sole alongshore averaged cross-shore position, therefore alongshore uniform and based on y_b only. Solid line: barline profile reduced to its linear fit, therefore based on both y_b and α_b.*

Above considerations and the rotation model results indicate that the morphodynamic state of the bar at Tairua Beach can be described by its alongshore-averaged orientation, in addition to the classical parameters that are its alongshore averaged cross-shore position and its alongshore variability [*Plant et al.* 2006, *Splinter et al.* 2011]. Indeed, the barline orientation contributes significantly to

the overall behaviour of the sandbar as it accounts for approximately 20 to 30 % of barline variability at its extremities (see Figure 2.9).

As shown in section 2.5, the rotation of the barline can be associated with external wave climate parameters, such as the wave energy and the alongshore wave energy gradient along the bar. Indeed, these two external parameters, involved in the semi-empirical formulation of the rotation model presented in this paper (Equation 2.8) were able to hindcast 63 to 82 % (see section 2.5.1 and Table 2.2) and forecast 62 to 78 % (see section 2.5.2 and Table 2.4) of the overall variability of the orientation of Tairua Beach barline on a 7-year dataset of observations.

The dependance of the barline orientation dynamics on the alongshore gradient of wave energy suggests the strong influence of the beach geometrical settings on the domain of applicability of the bar rotation concept and its model. Embayed beaches hydrodynamic and morphodynamic patterns can be related to distinct geometrical settings [*Short* 1999, *Castelle and Coco* 2012; 2013]. According to these studies. the main parameters controlling the nearshore circulation patterns in the embayment are the ratio of the embayment length over the surfzone width and the shoreline curvature. In comparison to other embayed beaches, Tairua exhibits a small curvature (its time-averaged shoreline profile over 7 years shows a 12 m cross-shore distance between its extremities pointing seawards and its deeper central part). In addition, the beach shows a large ratio of embayment length over time-averaged surfzone width. *Castelle and Coco* [2012] evaluate it to 46.9. Due to the longer observation time in the present study, leading to a higher time-averaged value of H_s (0.85 m) and consequently a larger time-averaged surfzone width, this ratio decreases to 31. *Castelle and Coco* [2012] find that low curvature and high ratios (above 16 for straight beaches but much higher (above 30) for curved beaches) generate "normal circulations" (2 headland- and 4 or more other rip channels) as observed in Tairua [*Gallop et al.* 2011]. Low curvature and high ratio of embayment length over surfzone width are therefore the main constraints that allow hydro- and morphodynamic patterns similar to Tairua Beach to be observed. As such, they are necessary beach properties to fulfil to apply the barline rotation concept and model to other embayments.

According to *Castelle and Coco* [2012], another important parameter of an embayment geometry is its length, which at Tairua is 1.2 km. This value classifies Tairua in the category of beaches with embayment lengths between 1 and 4 km. In their study, *Castelle and Coco* [2012] explain that this range favours shoreline rotation induced by longshore transport due to the favourable compromise of a limited effect of the headland rips and a limited amount of sediment that needs to be transported along the shore. The relevance of the embayment length parameter concerning the barline rotation is therefore related to the relevance of the longshore sediment transport in this rotation. The success of the model, itself derived from a semi-empirical cross-shore migration model (Equation 2.2) and therefore not taking into account any effect of longshore currents, indicates that cross-shore processes are primarily involved in the rotation of the sandbar. However, the alongshore gradient of wave energy appearing in the model is also able to generate alongshore forcing in the water column. Therefore it is relevant to assess the role of this forcing in the generation of longshore currents.

A comparison of the alongshore forcing induced in the flow by the alongshore wave energy gradients with the alongshore forcing induced by the incident wave obliquity (not appearing in the model) shows if the gradients have any potential to induce specific flow patterns. The alongshore forcing in shallow water applied to the water column per unit length due to wave energy gradients is written

[*Longuet-Higgins and Stewart* 1964]:

$$F_x = F_{x,1} + F_{x,2}, \tag{2.12}$$

$$F_{x,1} = -\left(\frac{1}{2} + \sin^2(\theta)\right)\frac{\partial E}{\partial x}, \tag{2.13}$$

$$F_{x,2} = \cos(\theta)\sin(\theta)\frac{\partial E}{\partial y}, \tag{2.14}$$

$$\frac{\partial E}{\partial y} = -\frac{E\beta\gamma}{H_s}. \tag{2.15}$$

The first term $F_{x,1}$ describes the forcing induced by the alongshore wave energy gradient whereas the second term $F_{x,2}$ is the alongshore forcing due to oblique waves breaking in the surfzone. The cross-shore gradient of wave energy is approximated by the ratio of incident wave energy over the surfzone width ($H_s/\beta\gamma$). In the dataset, $F_{x,2}$ has a larger intensity than $F_{x,1}$ in 99.4% of the modelled conditions and they have opposite directions in 80% of the modelled conditions. This indicates that longshore currents are mainly driven by wave obliquity rather than by wave alongshore gradients and that for most conditions, alongshore gradients actually weaken the longshore currents and the underlying longshore transport. This confirms that longshore currents, mainly related to wave obliquity and ignored in the present model, are unlikely to be the primary drivers of the barline rotation at Tairua Beach and in embayed environments exhibiting similar flow patterns.

The limited role of longshore currents and transport is confirmed by the data. A commonly admitted process induced by longshore currents over a sandbar is the migration of its rip channels along its crest [*Falquès et al.* 2008]. This process can be observed between May 2001 and June 2002 in Figure 2.2. A complex alongshore migration of the sandbar rip channels is observed and indicates alongshore sediment transport, but this does not translate in any significant reorientation of the barline.

Further study is required to assess the exact role of longshore currents, but in the present case it appears to be weak and does not justify additional constraints on the embayment geometry regarding the application of the barline rotation concept. However, it is clear that the alongshore gradient of wave energy has a primary role. Therefore the geometrical settings yielding to this gradient are a major requirement for the model to be applicable at other locations. This means that the beach needs to exhibit headlands that are long enough compared to its embayment length in order to generate this gradient. To summarise, the relevance of the barline orientation as a parameter describing the morphological state of a sandbar and the applicability of the rotation model presented in this study are therefore restricted to single-barred embayed beaches exhibiting a low curvature, a high ratio of embayment length over surfzone width and headlands that are sufficiently long to induce alongshore wave energy gradients along the embayment.

2.6.2. Pivotal and cross-shore migration-driven rotation mechanisms

Two terms appear on the right hand side of the rotation model formulation (Equation 2.8) that can be related to different processes involved in the rotation of the barline. The first term is defined in

the present paper as R_α:

$$R_\alpha = C_{\alpha_b}\left[\sqrt{E}\left(\frac{\partial E}{\partial x} - \delta a_b(\alpha_b - \alpha_0)\right)\right] f_b(H_s, H_b) \tag{2.16}$$

This term computes the difference between the alongshore gradient of wave energy along the coastline and an equilibrium value for this gradient depending on the actual orientation of the barline $\alpha_b - \alpha_0$. The angle α_0 defines the equilibrium barline angle corresponding to a zero gradient of the wave energy. Barline migration here only acts through the morphodynamic damping factor (Equation 2.3) controlling the intensity of the rotation. Therefore, this term R_α can be related to an independent pivotal rotation process, which may occur during migration but is not coupled with it except in terms of intensity.

The second term in Equation 2.8 is defined as M_α:

$$M_\alpha = C_{\alpha_b}\left[\frac{1}{2\sqrt{E}}\frac{\partial E}{\partial x}(E - (a_b y_b + b_b))\right] f_b(H_s, H_b) \tag{2.17}$$

M_α is composed among other factors of the difference between the equilibrium wave energy and the actual incident wave energy and of the alongshore gradient of wave energy along the beach. Therefore it computes the amount of rotation that is related to the overall migration of the bar and induced by a differential progression of the cross-shore sections of barline when a wave energy gradient is observed in the alongshore direction. A brief summary of the action of this term is given in Table 2.5. The alongshore gradient in wave energy actually enhances (damps) the barline migration at the beach extremity where the wave energy is higher (lower).

A limitation of the physical meaning of this term is found during onshore migration conditions. This can be shown in the example of an alongshore uniform barline profile and an incident wave energy exhibiting a positive alongshore gradient such that the equilibrium position of the barline is located onshore of the bar at the north and at the bar location at the south. In this case, M_α computes a clockwise rotation by expecting the bar to migrate faster at the south (see Table 2.5). However, being already there at its equilibrium position, only the northern extremity will migrate, inducing an anti-clockwise rotation.

In the Tairua 7-year dataset, the pivotal rotation largely dominates the response of the barline. Figure 2.10 shows first that M_α is one order of magnitude below R_α. Then, the model skills are found to be almost identical when using the formulation with (Equation 2.8) or without (Equation 2.16) M_α (see Table 2.6). Neglecting the second term, M_α, in Equation 2.8 actually leads to an increase of parameter C_{α_b} (not shown here). This relates to the significant correlation ($R^2 = 0.72$) between R_α and M_α when $E > E_{eq,b}$ (see Figure 2.10). This indicates that the model compensates for the

Table 2.5.: *Qualitative effects of M_α on the sandbar rotation as a function of the barline migration direction and the alongshore gradient of incident wave energy.*

	$E > E_{eq,b}$ (offshore)	$E < E_{eq,b}$ (onshore)
$\frac{\partial E}{\partial x} > 0$	anti-clockwise	clockwise
$\frac{\partial E}{\partial x} < 0$	clockwise	anti-clockwise

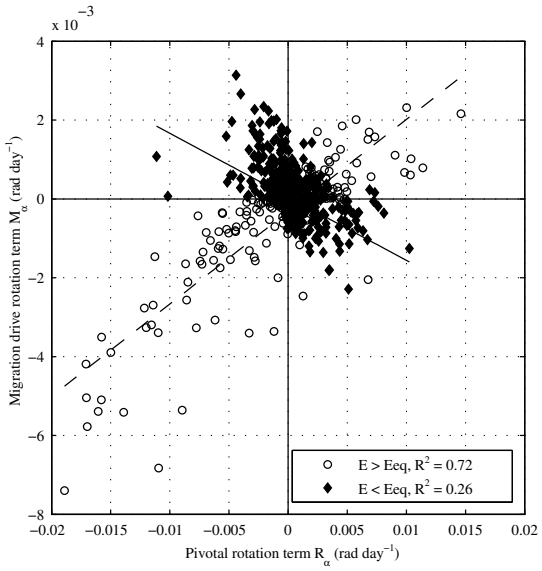

Figure 2.10.: *Second term M_α as a function of the first term R_α in the right hand side of Equation 2.8 when $E > E_{eq,b}$ (empty circle) and $E < E_{eq,b}$ (filled diamonds) with associated regression lines and coefficients .*

absence of M_α by increasing C_{α_b} to include the effect of events when $E > E_{eq,b}$. Additionally, this means that the contribution of M_α when $E < E_{eq,b}$ does not participate in the sandbar rotation description at Tairua.

The dominance of R_α in Equation 2.8 indicates that there is a weak or no coupling between the sandbar migration and rotation at Tairua Beach. This can be directly related to the weak correlation between the position and orientation signals already mentioned in section 2.3.2. Migration and rotation are thus likely to occur simultaneously because wave climate events with oblique incidence are likely to induce alongshore wave energy gradients (due to headland hindering or island hindering for instance). However the observations and the semi-empirical model show that if they are simultaneous they are only weakly coupled and strong migration can occur without rotation (from August 2001 until March 2002) and vice-versa (Event III in July 2002) (see Figure 2.2).

Table 2.6.: *Rotation model skills with for the 7-year and five 3-year long time periods. Subscript 0 and 1 stand for the rotation model without and with term M_α.*

Time	$RMSE_1$	$RMSE_0$	R_1^2	R_0^2	Bss_1	Bss_0
1999-2006	0.025	0.025	0.67	0.68	0.66	0.68
1999-2002	0.017	0.017	0.82	0.82	0.82	0.82
2000-2003	0.020	0.021	0.81	0.81	0.81	0.81
2001-2004	0.022	0.023	0.80	0.78	0.80	0.78
2002-2005	0.019	0.019	0.81	0.82	0.80	0.81
2003-2006	0.022	0.022	0.63	0.63	0.63	0.63

2.6.3. Characteristic response time

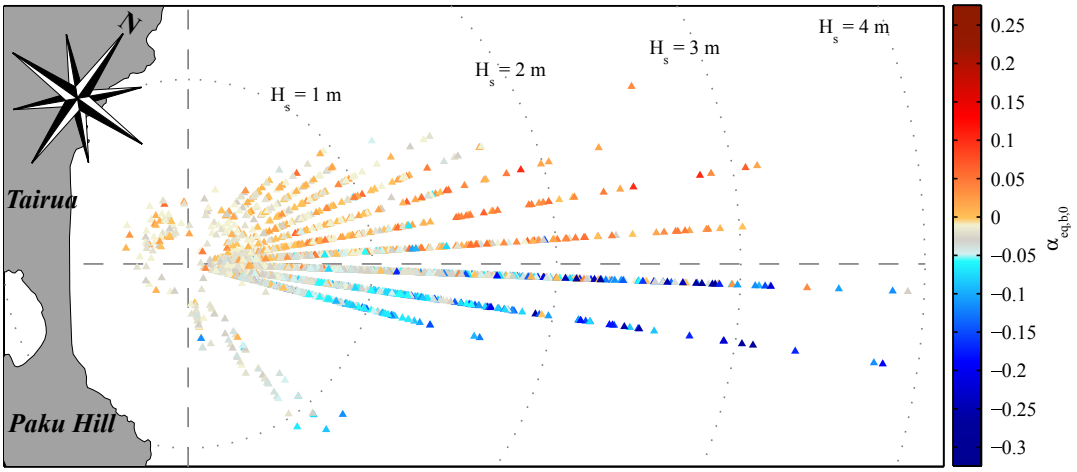

Figure 2.11.: *Equilibrium barline angle $\alpha_{eq,b,0}$ (colorscale centered on $\alpha_0 = -0.024$) as a function of the incident significant wave height $H_{s,0}$ (values indicated on the dotted circles) and wave angle (angular position of the markers). Angle 0 corresponds to the normal to the beach represented by the dashed line. Positive (negative) values of $\alpha_{eq,b,0}$ stand for equilibrium barline orientations seawards at the south (north) and shorewards at the north (south).*

The response time is a critical parameter of dynamic coastal systems. It provides insight into the temporal scale covering a system's dynamics. In particular, it describes if a system is likely to be in equilibrium with its forcing conditions depending on the characteristic time scale of the forcing variations. For example, it enables to understand if the frequency and chronology of energetic events play an important role in beach morphodynamics. Indeed if such events are separated by a time period shorter than a beach response time, it is likely that they will have partly superimposed consequences on this beach. Studying response times solely from data timeseries is difficult due to the non-linear character of the dynamics of the system. Here, the semi-empirical model developed for Tairua Beach is used for a systematic analysis since it can simulate the morphodynamic response of this coastal system as a function of its previous state and the external forcing conditions.

Instantaneous characteristic response times of the barline related to constant wave energy conditions E_0 can be obtained from the strongly non-linear Equations 2.6 and 2.8 by assuming that any slight change in the bar morphology in terms of migration and rotation does not affect the morphodynamic damping factor $f_{b,0}$ depending on E_0 and y_b. In addition, we assume that the variations of the second term M_α of Equation 2.8 induced by slight changes in y_b can be neglected . This hypothesis is acceptable in the present case since M_α has limited influence to the solution (see section 2.6.2). It may however not be applicable to other embayed beaches, especially if they show

different geometries. In these conditions Equations 2.6, 2.8 and 2.3 can be written:

$$\frac{\partial y_b}{\partial t} + C_{y_b} a_b \sqrt{E_0} f_{b,0} y_b = C_{y_b} \sqrt{E_0}(E_0 - b)) f_{b,0}, \tag{2.18}$$

$$\begin{aligned} \frac{d\alpha_b}{dt} + C_{\alpha_b} \sqrt{E_0} \delta a_b f_{b,0} \alpha_b = \\ C_{\alpha_b}\Big[\sqrt{E_0}\left(\delta a_b \alpha_0 + \frac{\partial E_0}{\partial x}\right) \\ + \frac{1}{2\sqrt{E_0}} \frac{\partial E_0}{\partial x}(E_0 - (a_b y_b + b_b))\Big] f_{b,0}, \end{aligned} \tag{2.19}$$

$$f_{b,0} = \min\left(\left[\frac{H_{s,0}}{H_b}\right]^p, 1\right) \tag{2.20}$$

where only y_b and α_b are varying. These first-order equations result in the following instantaneous characteristic times and equilibrium values:

$$\tau_{y_b} = \frac{1}{C_{y_b} a_b \sqrt{E_0} f_{b,0}}, \quad \tau_{\alpha_b} = \frac{1}{C_{\alpha_b} \delta a_b \sqrt{E_0} f_{b,0}}, \tag{2.21}$$

$$y_{b,0} = \frac{E_0 - b_b}{a_b} = y_{eq,0}, \tag{2.22}$$

$$\alpha_{eq,b,0} = \alpha_0 + \frac{1}{\delta a_b} \frac{\partial E_0}{\partial x}\left[1 + \frac{1}{2}\left(1 - \frac{E_{eq,b}}{E_0}\right)\right] \tag{2.23}$$

in which τ_{y_b} and τ_{α_b} are the instantaneous characteristic response times of the barline alongshore averaged cross-shore position y_b and orientation α_b respectively. $y_{b,0}$ is the equilibrium barline position corresponding to an incident energy E_0 (see Equation 2.1) and $\alpha_{eq,b,0}$ is the equilibrium barline orientation corresponding to an incident energy E_0 and its alongshore gradient.

As expected, the cross-shore position y_b evolves towards the equilibrium barline position $y_{b,0} = y_{eq,0}$ corresponding to E_0. The equilibrium value $\alpha_{eq,b,0}$ defined in Equation 2.23 has been computed for the 7 years of wave climate data at Tairua Beach assuming that M_α could be neglected, so that $\alpha_{eq,b,0}$ depends only on the alongshore gradient of wave energy. Results are presented in Figure 2.11 as a function of the incident wave conditions (H_s, θ). Here and in the following discussion, the free parameters of the models used to compute the different barline characteristics are the average values of the parameters obtained for the five 3-year time periods hindcasts (see Table 2.3). The results show that wave energy coming from the north (south) is likely to induce a positive (negative) orientation of the barline, corresponding to the southern (northern) extremity of the bar being moved seawards of the northern (southern) extremity respectively. In addition, the absolute value of the angle increases with the wave energy. However, the extreme values of $\alpha_{eq,b,0}$ are much larger for negative angles (around -0.3) than for the positive ones (approximately 0.1) which here can be related to the influence of Shoe Island (Figure 2.1) hindering the waves at the south of the beach.

The characteristic response times of the barline migration τ_{y_b} and rotation τ_{α_b} (Equation 2.21) are

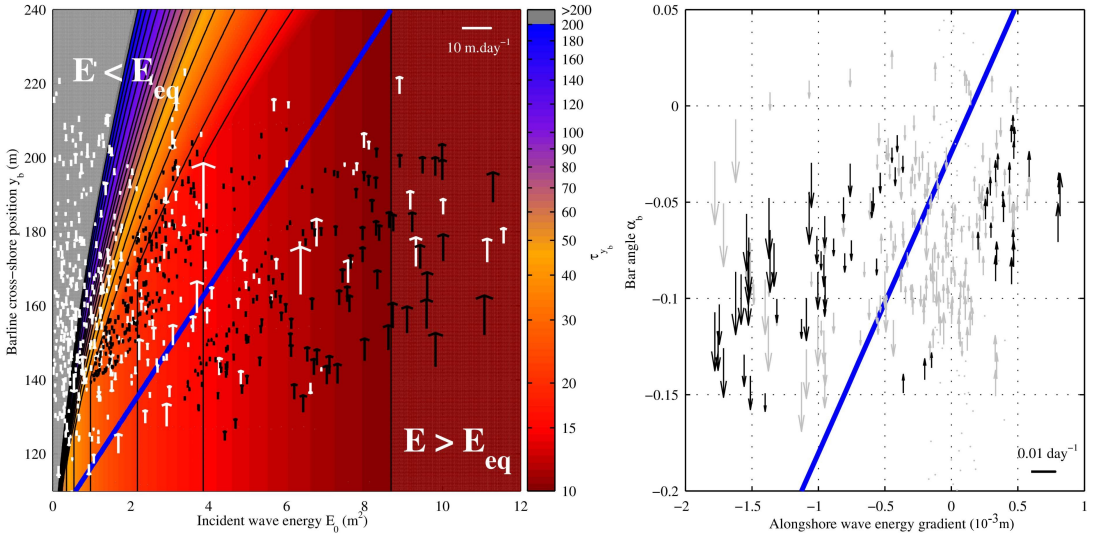

Figure 2.12.: *Left: Characteristic response time of the barline cross-shore position τ_{y_b} (colorscale) in days as a function of the incident wave energy E_0 and the barline cross-shore position y_b. The equilibrium cross-shore bar location $y_{b,0}$ (see Equation 2.22) is represented as a function of E_0 (blue line). Arrows indicate the measured (white) and computed (black) values of the migration rate (m/day) for the 7-years hindcast run. Only values above 0.8 m/day are shown. The horizontal white line in the upper right corner gives the arrow scale. Right: The blue line represents the equilibrium barline angle $\alpha_{eq,b,0}$ (see Equation 2.23) as a function of the alongshore gradient of wave energy. Arrows indicate the measured (grey) and computed (black) values of the rotation rate (day^{-1}) for the 7-year hindcast run. Only values above 0.005 day^{-1} (or 6 m per day over 1.2 km) are shown. The horizontal black line in the lower right corner gives the arrow scale.*

inversely proportional to the instantaneous bar morphodynamic damping factor $f_{b,0}$ and the incident significant wave height ($\sqrt{E_0} = H_{s,0}$). Remarkably, the characteristic time for the migration and the rotation of the barline are related by:

$$\frac{\tau_{\alpha_b}}{\tau_{y_b}} = \frac{C_{y_b}}{C_{\alpha_b}\delta} \tag{2.24}$$

The value of this ratio is 1.05, showing that the migration and the rotation of the bar occur on similar time scales. Figure 2.12 presents the instantaneous response time of the barline cross-shore position τ_{y_b} as a function of E_0 and y_b).

Response times vary from O(10 days) during energetic conditions or when the bar is located nearshore until O(100 days) during calm conditions or when the bar is located offshore. These values compare well with the response times found by *Plant et al.* [2006] on 2-months observations. For wave energy conditions above $E_{eq,b}$ corresponding to offshore migration conditions, $f_{b,0}$ is 1 and τ_{y_b} depends only on the incident wave energy (see Equation 2.21). Values of τ_{y_b} in these conditions remain below 35 days for significant wave heights above 1 m. On the graph representing y_b in Figure 2.6, this can be related to the steep slopes observed during offshore migration events compared to the mild slopes of the subsequent shoreward migration events.

Arrows in Figure 2.12 indicate the modelled and measured migration and rotation rates. The intensity and the direction of the rotation rates (right panel) agree reasonably well with a clear inversion across the line defining the equilibrium bar angle $\alpha_{eq,b,0}$ (see Equation 2.23 and Figure 2.11). The measured and computed rotation rates are increasing with increasing intensities of wave energy alongshore gradients as this increases the difference between the current and equilibrium barline angles. However for constant alongshore gradient of the wave energy (that is along the vertical in Figure 2.12, right panel), the increase in rotation rate expected for increasing differences between actual and equilibrium barline angles, observed for computed values (black arrows), is not clearly seen in the data (grey arrows). These differences can be due to the fact that the damping factor playing a significant role in the formulation of τ_{α_b} (Equation 2.21) can be different between the modelled and observed values as there is a difference between modelled and measured barline cross-shore positions.

The measured and modelled offshore migration rates displayed in Figure 2.12 (left panel) show also a good agreement in terms of direction and intensity, especially when the incident wave energy is higher than $E_{eq,b}$. In this case, the intensity of the modelled and measured migration rates increase when the difference between the incident and equilibrium wave energy increases. When $E < E_{eq,b}$, a number of arrows representing observations (white) are not pointing towards the equilibrium location of the sandbar (blue line), especially for intermediate values of the wave energy (E_0 between 2 and 4 m^2). This can be due to the method used here to compute the incident energy E_0 corresponding to each migration rate in which the wave energy is averaged in between two observations. Since the averaged time period between successive observation is approximately three days, it is likely that a number of E_0 values are underestimated when storms are occurring. As well, the wave model may slightly underestimate the value of certain storm peaks. In addition, white arrows in the area of characteristic time scales above 100 days show measured bar migration rates under low wave energy conditions that are clearly underestimated by the model (the corresponding modelled values are below 0.8 m/day and therefore not represented in the figure). The natural behaviour of the bar appears to be complex with onshore and offshore migration observed for similar values of y_b and E_0. This can be directly linked to the limitations of the migration model to simulate short time scale events and the fact that its formulation does not include a description of the barline alongshore variability. Indeed, these small scale migration events are possibly related to the morphodynamics of small scale barline features influencing the mean cross-shore position as mentioned in section 2.3.2 and shown by *Splinter et al.* [2011].

The models outcomes in Figure 2.12 can be directly related to the observations of *Wright and Short* [1984] (see their Figure 12), stating that each extreme and intermediate beach states may exist as equilibrium state in association with an appropriate set of conditions. In particular the applicability of this concept to the barline orientation shown in the present study confirms that this parameter is a relevant descriptor of the bar state in an embayed beach environment.

2.7. Conclusion

The behaviour of a subtidal bar at a single-barred embayed beach has been investigated extensively in order to evaluate and characterise the concept of sandbar rotation. Video imagery techniques

allowed to monitor the sandbar state at Tairua during seven years. These data showed qualitatively that the state of the bar can be described by a reduced approximation being the combination of its alongshore averaged cross-shore position and its overall orientation without taking into account small scale morphological features. Quantitatively, the orientation signal was found to contribute up to 30 % in the variability of the barline at its extremities. The barline position and angle showed both dominating fluctuations in the interannual range with significant variability in the interannual and annual range but were found to be only weakly correlated.

The barline rotation was modelled by using a semi-empirical approach which enabled to hindcast and forecast 7-year barline observations as a function of external wave conditions derived from WW3 CFSRR reanalysis hindcasts (NOAA). The model shows on average good to excellent skill. In particular, events with periods longer than 3 months are well simulated while events with shorter periods are only partly represented.

By construction, the barline rotation model compares the differences in bar cross-shore migration rates induced by cross-shore processes along the embayment. Therefore this model supports the hypothesis that barline rotation is induced by cross-shore processes. This is confirmed by the fact that the rotation is essentially driven by the alongshore gradient of wave energy. Such alongshore gradients of wave energy can also generate longshore currents. However, the comparison of the terms involved in the wave-induced alongshore forcing of the flow in the surfzone, and the observation of rip channels alongshore migration without subsequent barline rotation in the 7-year dataset, support the hypothesis of a weak involvement of longshore transport processes in the barline rotation. Nevertheless, due to the complexity of the longshore current generation in the embayment, further research is needed to assess the exact role of the longshore transport in the barline rotation.

Two rotation mechanisms have been inferred from the model formulation. First, a pivotal rotation mechanism is directly related to the alongshore gradient of wave energy and not necessarily associated to the overall migration of the barline. This pivotal rotation is largely dominant. Then, a migration-driven rotation mechanism consists of a rotation induced by a differential cross-shore migration of the barline along the beach during an overall migration. However, the contribution of this second process is one order of magnitude smaller than the intensity of the pivotal rotation mechanism at Tairua Beach and its relevance could therefore not be clearly assessed.

The models were applied for a systematic analysis of the sandbar response to external conditions. The extension of the breakpoint hypothesis controlling the equilibrium cross-shore position of the sandbar allows to introduce an equilibrium wave angle related to the gradient of wave energy along the beach. Migration and rotation characteristic times were found to be similar and depend on the incident wave energy and on a morphodynamic damping factor that compares the ratio of offshore incident wave height over the breaking wave height at the crest location. This factor that can be related to the wave energy dissipation over the bar that controls its morphodynamic activation during onshore events. Under these conditions, characteristic response times vary from 10 to several 100 days. During energetic conditions when the bar migrates offshore, the wave dissipation is saturated and the characteristic time remains below 35 days.

Whereas the present study focuses on the nearshore sandbar at Tairua Beach, the rotation of sandbars is a common feature of single-barred embayed beaches. This confirms that, in combination with other bar state descriptors such as the barline alongshore averaged cross-shore position and

its alongshore variability, the barline orientation is a relevant parameter of the description of the barline behaviour in such environment. However it must be noticed that the development of the model relates to the geometrical and environmental properties of Tairua Beach. This limits the domain of applicability of the model to single-barred embayed beaches located in a microtidal environment, exhibiting a limited curvature, a narrow surfzone width compared to its embayment length, and headlands that are sufficiently long to induce alongshore wave energy gradients along the embayment. Further investigation is required to extend the applicability of the models to other single-barred embayed beaches facing different tidal and wave conditions and showing different sedimentological and geometrical properties.

2.8. Acknowledgments

This study was funded by the DFG (Deutsche Forschungs-Gemeinshaft) International Research Training Group INTERCOAST (Integrated Coastal Zone and Shelf-Sea Research). Large scale bathymetric and topographic data were provided by the Land Information New Zealand government department (LINZ) and the National Oceanic and Atmospheric Administration (NOAA, USA) provided the 7-year wave climate hindcast dataset used in this study. Wave buoy data have been provided by the Bay of Plenty Regional Council (NZ) and the camera images by the Waikato Regional Council (NZ). In addition, the authors would like to acknowledge Dirk Immenga and the members of INTERCOAST and the University of Waikato who helped during the topographic, bathymetric and hydrographic surveys at Tairua Beach in 2011, George Payne for his essential work in maintaining the CamEra system at Tairua and Wietse van de Lageweg for the digitization and georectification of the barlines from the video dataset. The authors wish to acknowledge two anonymous reviewers for their helpful suggestions and comments. The data used in this study are available on PANGAEA (http://www.pangaea.de) using the doi of the present publication.

Chapter 3

Frequency response of a nearshore sandbar to varying wave conditions at single-barred embayed beaches.

3.1. Introduction

In this chapter, the models developed in chapter 2 are used to assess the response of the nearshore sandbar of a single-barred embayed beach to varying forcing frequencies. A harmonic analysis of the models response shows that both the bar cross-shore position and orientation follow the equilibrium values defined by varying external wave conditions at low frequencies (time periods above 3 years) whereas at higher frequencies, they both stabilize around steady configurations with a bar that is located at the outer edge of the surfzone for energetic wave events.

3.2. Harmonic analysis

3.2.1. Methodology

Wright and Short [1984] mention the relevance of studying the frequency response of beach systems to harmonic forcing external conditions. This enables to understand how beach profiles react to varying wave conditions and in particular if they are likely to describe all intermediate equilibria defined by the varying forcing conditions or if they would rather stabilize around an intermediate state. Such analysis can be performed here using the semi-empirical models.

The strict area of validity of the models is defined by the properties of the 7-year wave climate dataset used in the calibration and validation process and the ability of the models to simulate the observed morphodynamics during this period. Therefore according to the coherence study (see Figure 2.6), the confidence is high for forcing frequencies f_j between 0.3 and 3 cy^{-1} and reasonable for $3 < f_j < 20$ cy^{-1}. In the 7-year wave climate dataset, the wave energy reaches a maximum of 15 m^2, defining the confidence area for the bar cross-shore frequency response. However, in the following, the range of investigation is extended further in order to provide insight on the barline behaviour beyond the limitations induced by the conditions covered by the dataset.

Time varying signals of the incident wave energy $E_{i,j}$ are generated to evaluate the barline position

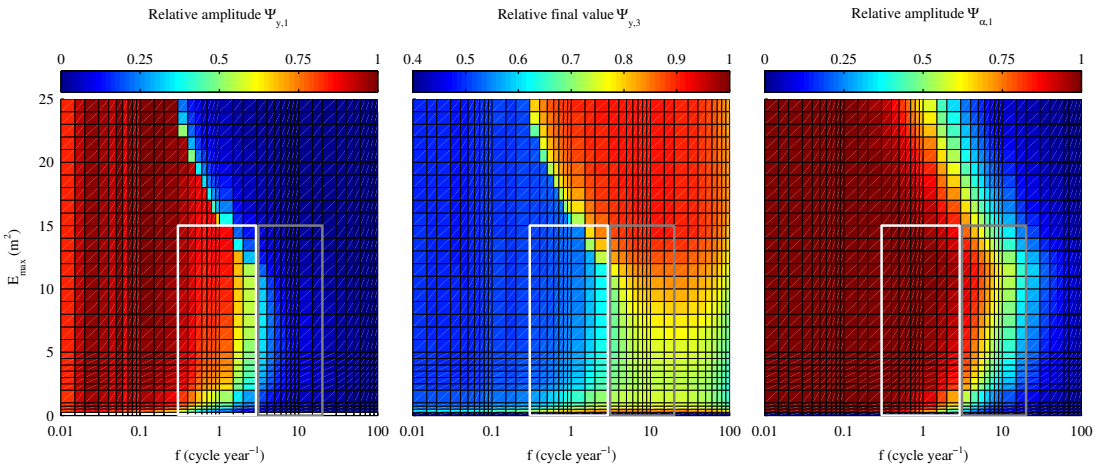

Figure 3.1.: *Relative amplitude of the cross-shore barline position response $\Psi_{y,1}$ (left), ratio $\Psi_{y,3}$ of the final mean position of the barline compared to the maximum reachable position $y_{eq,i}$ (middle) and relative amplitude of the barline angle response $\Psi_{\alpha,1}$ (right). All data are function of the wave forcing frequency f in cy^{-1} (x axis) and amplitude E_{max} in m^2 (y axis). The white rectangle represents the high confidence area. The gray rectangle delimits the area where the model performed reasonably well. Other areas have been extrapolated.*

response:

$$E_{i,j}(t) = E_{max,i}\left[\frac{1}{2} + \frac{1}{2}\sin\left(2\pi f_j t\right)\right] \tag{3.1}$$

with $E_{max,i}$ the wave energy amplitude taking values between 0 and 25 m^2 and f_j the signal frequency ranging from 0.01 to 100 cy^{-1} (period ranging from 100 years down to 3 days).

For each signal $E_{i,j}$, the migration model is run during a sufficiently long time period so that the response becomes stable in term of amplitude and frequency. This transition time is typically one to three months and increases to several years for very low values of E_{max} and f_j. The stable part of the response, Y_B, is analysed according to the following parameters:

$$\Psi_{y,1} = \frac{\max(Y_B) - \min(Y_B)}{y_{eq,i} - y_{eq,E=0}}, \tag{3.2}$$

$$\Psi_{y,2} = \frac{\phi(Y_B) - \phi(E_{i,j})}{2\pi f_j}, \tag{3.3}$$

$$\Psi_{y,3} = \frac{< Y_B > - y_{eq,E=0}}{y_{eq,i} - y_{eq,E=0}} \tag{3.4}$$

$\Psi_{y,1}$ is the ratio of the bar response amplitude compared to the maximum expectable amplitude defined by the difference between the bar equilibrium positions for $E = E_{max,i}$ ($y_{eq,i}$) and $E = 0$ ($y_{eq,E=0}$). $\Psi_{y,2}$ is the time delay between the forcing signal and the response computed from the difference between phases $\phi(Y_B)$ of Y_B and $\phi(E_{i,j})$ of $E_{i,j}$. $\Psi_{y,3}$ compares the average position $< Y_B >$ of the stable signal to the maximum offshore equilibrium position of the bar $y_{eq,i}$ corresponding to

$E_{max,i}$. These positions are compared to the equilibrium bar location at zero energy $y_{eq,E=0}$ so that $\Psi_{y,3} = 0$ corresponds to a final average position at $y_{eq,E=0}$ and $\Psi_{y,3} = 1$ to a final average position at $y_{eq,i}$.

For the barline angle, the computation of the response is simpler by considering $E_{i,j} = E_{max,i}$ constant and that the bar has reached its equilibrium cross-shore position $y_{eq,i}$. Then the forcing signal becomes the sum of the constant energy $E_{max,i}$ and a time-fluctuating term resulting from an alongshore-constant wave energy gradient:

$$F_{i,j}(x,t) = E_{max,i} + \nabla_x(F_{i,j})(t)\left(x - \frac{L}{2}\right), \tag{3.5}$$

$$\nabla_x(F_{i,j})(t) = G_{max}\sin\left(2\pi f_j t\right) \tag{3.6}$$

in which $F_{i,j}$ is the incident wave energy signal defined along time and alongshore dimensions, $\nabla_x(F_{i,j})$ is the alongshore wave energy gradient, constant along the beach and therefore only time dependant. L is the length of the beach so that x varies between 0 and L and the alongshore average value of $F_{i,j}$ is always $E_{max,i}$. G_{max} and f_j define the amplitude and the frequency of the alongshore gradient fluctuations respectively.

Since the alongshore average value of $F_{i,j}$ is always $E_{max,i}$ and the alongshore averaged position of the barline is $y_{eq,i}$, the right hand side term of Equation 2.8 becomes R_α (Equation 2.16) with H_s and H_b constant, reducing the model to a first-order linear equation. Then the harmonic response α_B, the transfer function $\underline{H}$ and the evaluation parameters can be computed as:

$$\underline{H} = \frac{\underline{\alpha_B}}{\underline{\nabla_x(F_{i,j})}} = \frac{\frac{1}{\delta a_b}}{1 + 2\mathrm{i}\pi f_j \tau_{\alpha_b,i}}, \tag{3.7}$$

$$\Psi_{\alpha,1} = \delta a_b |\underline{H}|, \quad \Psi_{\alpha,2} = \frac{\phi(\underline{H})}{2\pi f_j} \tag{3.8}$$

where the underline indicates complex numbers, $\mathrm{i} = (-1)^{\frac{1}{2}}$ and $\tau_{\alpha_b,i}$ is the constant characteristic time depending on $E_{max,i}$ and $y_{eq,i}$ (see Equation 2.21). $\underline{H}$ is the ratio between the complex amplitude of the angle response $\underline{\alpha_B}$ and the complex amplitude of the forcing alongshore wave energy gradient signal $\underline{\nabla_x(F_{i,j})}$. Similarly to Equation 3.4, $\Psi_{\alpha,1}$ is the ratio of the response amplitude over the maximum expectable amplitude defined by the difference between the bar orientations for $\max(\nabla_x(F_{i,j})) = G_{max}$ and $\min(\nabla_x(F_{i,j})) = -G_{max}$. $\Psi_{\alpha,1}$ is related to the amplitude of $\underline{H}$. $\Psi_{\alpha,2}$ is the time delay between the forcing signal and the angle response defined by the phase of $\underline{H}$, $\phi(\underline{H})$. $\Psi_{\alpha,3}$ is not considered as the symmetric properties of the forcing signal $\nabla_x(F_{i,j})$ drive it towards a long-term averaged value of α_0.

3.2.2. Results and discussion

Results for $\Psi_{y,1}$, $\Psi_{y,3}$ and $\Psi_{\alpha,1}$ are presented in Figure 3.1 and schematic representations of four extreme cases are presented in Figure 3.2. Although the non-linear harmonic response of the barline cross-shore position has been obtained by running the model and the linear harmonic response

of the barline angle has been computed theoretically, both responses have similar characteristics in terms of relative amplitude. At low frequencies ($f_j < 0.3$ cy^{-1} or time periods above 3 years), $\Psi_{y,1}$ and $\Psi_{\alpha,1}$ are close to 1, indicating that the bar reaches its equilibrium state for each intermediate forcing condition. As a result, for these low frequencies, the oscillations of y_b cause its final mean value to be the average of the minimum and maximum reachable values ($\Psi_{y,3} \simeq 0.5$). In Figure 3.2, at low-frequency wave energy fluctuations, the green area reached by the barline corresponds to the area defined by the minimum and maximum reachable values ($y_{eq,i}$ and $y_{eq,E=0}$) of the barline position (hatched area). Similarly, at low-frequency wave energy alongshore gradient fluctuations, the barline area covered by the barline rotation (yellow) equals the overall reachable area (dots) defined by $|\alpha_{eq,b,i}| \leq (\delta a)^{-1} \max(\nabla_x(F_{i,j}))$ (or $(\delta a)^{-1} G_{max}$, see Equation 3.7 with $f_j = 0$). At high frequencies ($f_j > 4$ cy^{-1} (period below 3 months) and $f_j > 40$ cy^{-1} (period below 10 days) for the migration and the rotation respectively), the bar response does not vary within the forcing frequencies anymore and is rather constant ($\Psi_{y,1}$ and $\Psi_{\alpha,1}$ are close to 0). The orientation of the bar remains approximately parallel to the shore. In Figure 3.2, for high-frequency wave energy alongshore gradient fluctuations, the barline rotation does not increase the extension of the area reachable by the barline (no yellow area). More interestingly, for high-frequency wave energy fluctuations, the barline mean position is then closer to the maximum reachable position ($\Psi_{y,3}$ ranging between 0.7 and 0.95) meaning that the barline does not recover during calm conditions. The phenomenon increases with the amplitude of the energy variations and is related to the fact that the conditions are varying rapidly enough so that the bar is active ($f_b >> 0$) only during the most energetic conditions. For these high frequencies, the green area reached by the barline during its cross-shore migration in Figure 3.2 is restricted to the seaward side of the theoretically reachable area (hatched area). This extreme case can be interpreted as a long-term evolution of the beach profile towards the dissipative state.

A transitional behaviour is observed at intermediate frequencies, for $0.3 < f_j < 4$ cy^{-1} for the migration and between $0.3 < f_j < 40$ cy^{-1} for the rotation. These frequency ranges correspond approximately to the ranges covered by the 7-year dataset of Tairua Beach. At low wave energy ($E_{max} < 15$ m^2),the transition from a barline position response describing all intermediate equilibria ($\Psi_{y,1} = 1$) to a stable response at the maximum reachable equilibrium value corresponding to E_{max} is gradual for increasing frequencies. The same transition of the barline angle response is also gradual but is initiated at higher frequencies ($f_j \simeq 3$ cy^{-1}). It appears therefore that the barline angle is more likely to respond to high frequencies than the barline cross-shore position, at least if we neglect the influence of the small scale barline features.

For high incident wave energy ($E_{max} > 15$ m^2), the transition of behaviour occurs abruptly for the barline cross-shore position. This can be related to the faster energy variations due to larger energy fluctuations within identical time periods. The inertia of the barline does not allow it to follow the changes in incident wave energy anymore (f_b switches rapidly from 0 to 1 and vice versa). For the barline angle, the transition starts at similar frequencies but is gradual. Indeed, in this case, only the pivotal rotation is considered and therefore the barline is theoretically always located at its equilibrium cross-shore position. As a result, f_b depends only on E_{max} (constant) and there is no threshold effect with increasing frequencies.

Phase shifts $\Psi_{y,2}$ and $\Psi_{\alpha,2}$ are not represented here as they are very small compared to the time periods of the forcing signals. Largest computed shift reached 100 days. The highest ratios of phase

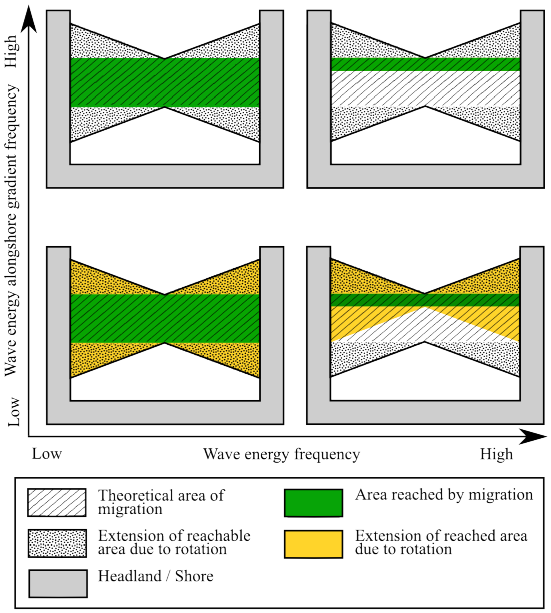

Figure 3.2.: *Schematic representation of the area reached by the nearshore sandbar of a single-barred embayed beach due to migration (green) and rotation (yellow) processes under harmonic forcing conditions for four characteristic cases. These cases are defined by low (high) frequencies of the wave energy and of its alongshore gradient fluctuations. The hatched and dotted areas represent the areas theoretically reachable by the barline and defined by the range of intermediate equilibria of the barline cross-shore position and orientation respectively.*

shifts over forcing time periods are between 10 % and 15 % and correspond to low ($E_{max} < 1$ m^2) or high ($E_{max} > 18$ m^2) amplitudes of the wave forcing in the range of biannual to interannual time periods. For other conditions, the phase shifts are close to zero.

3.3. Conclusion

Using the two calibrated and validated semi-empirical models developed in chapter 2, the barline response to harmonic forcing was investigated showing that the barline position and angle are only able to follow wave climate fluctuations down to 3-month time period for the former and 1-month time period for the latter. For fluctuations with shorter periods, the barline is likely to remain at a steady equilibrium location which in the case of high energetic events is located at the outer edge of the surfzone. In addition, the barline orientation would only weakly respond to high-frequency variations in the wave energy alongshore gradient.

Dissipative states are characterized by a mild beach slope and one to several nearshore parallel sandbar located far offshore. In agreement with the usual beach state theory, the outcomes of the harmonic analyses are consistent with the transition of the beach towards a dissipative state during periods characterised by a high frequency of storm events.

Chapter 4

Simple pocket beach rotation model derived from linear analysis

B. Blossier [(1)], K.R. Bryan [(2)] and C. Winter [(1)]

[(1)] MARUM, Center for Marine Environmental Sciences, University of Bremen, Leobener Strasse 28359 Bremen, Germany.
[(2)] Coastal Marine Group, Faculty of Science and Engineering, University of Waikato, Hamilton, New Zealand.

Published in peer-reviewed *Proceedings of the Coastal Sediments 2015*, World Scientific
DOI: 10.1142/9789814689977_0032, ISBN: 978-981-4689-97-7

4.1. Abstract

Coastal management along sandy beaches is directly related to the ability of decision makers to understand the behaviour of the upper profile of the beach. Using seven years of video images collected at Tairua Beach (NZ), we first characterise the behaviour of the beach shoreline by identifying two significant modes with a Principal Component Analysis. To relate these modes to external physical forcing conditions, we perform a Canonical Correlation Analysis and obtain two different contrasting modes. One mode describes a migration and is related to the ratio of peak over mean wave period. The other mode describes a combination of shoreline rotation and migration and is highly correlated to the amount of incident energy involved in alongshore sediment transport. This strong correlation is used as a basis to develop a semi-empirical model of the shoreline rotation at Tairua Beach. This model, calibrated on three years of observations, is able to describe accurately the measured shoreline orientation during four years.

4.2. Introduction

Forecasting the upper profile of a sandy beach is critical when assessing coastal flooding hazards. Coastal erosion and alongshore variability of the beach profile can potentially induce severe damage to the coastal dune system and eventually to nearby local dwellings. This becomes particularly true in coastal embayments. These areas are often under a significant anthropogenic pressure related

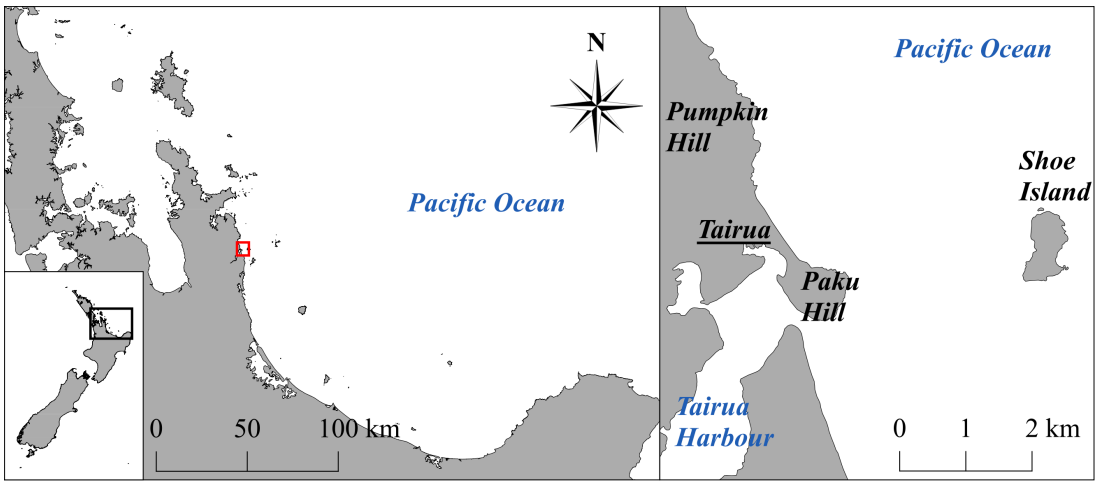

Figure 4.1.: *Geographical location of Tairua Beach (right) in New Zealand North Island, in the north of the Bay of Plenty (left).*

to their recreational attractiveness. Moreover, embayed beaches are very dynamic environments where the shoreline position can fluctuate significantly due to processes such as beach rotation.

In order to describe the position of a shoreline as a function of local external nearshore hydrodynamic parameters, different semi-empirical models have been developed in the past decade (e.g. *Yates et al.* [2009], *Davidson et al.* [2013]). These models simulate the cross-shore migration of a shoreline along several transects along an open coast [*Yates et al.* 2009] and a long embayed coastline (4 km) [*Davidson et al.* 2013].

Cross-shore migration is not the only large scale process encountered in embayed environments. *Ojeda and Guillén* [2008] and *Bryan et al.* [2013] observed shoreline rotation events at the temporal and spatial scales of migration events. Rotation occurs when an extremity of the embayed shoreline progradates while the other erodes. The phenomenon has usually been related to alongshore sediment transport. Following this hypothesis, *Turki et al.* [2013b] proposed a semi-empirical formulation showing encouraging results and relating the rotation of three beaches in Barcelona to the local alongshore component of the wave energy flux.

In contrast, *Harley et al.* [2011] reported that alongshore shoreline change may be caused by cross-shore hydrodynamic processes. The apparent change of orientation would therefore be due to local readjustments of the beach cross-shore profiles to alongshore varying wave conditions rather than the result of alongshore sediment transport.

Linear statistical analysis has been used extensively to characterise the behaviour of sand beaches [*Clarke and Eliot* 1982, *Miller and Dean* 2007a, *Harley et al.* 2011]. By decomposing the shoreline space-time signals into spatial modes and temporal functions, the characteristic morphodynamic behaviour described by these modes can be related to external forcing conditions. To do so, the correlation between the modes temporal functions and the forcing parameters timeseries is studied. In the present paper, we aim to describe the large scale behaviour of Tairua Beach using the statistical analysis of 7 years of shoreline observations. This analysis allows relating the rotation of the

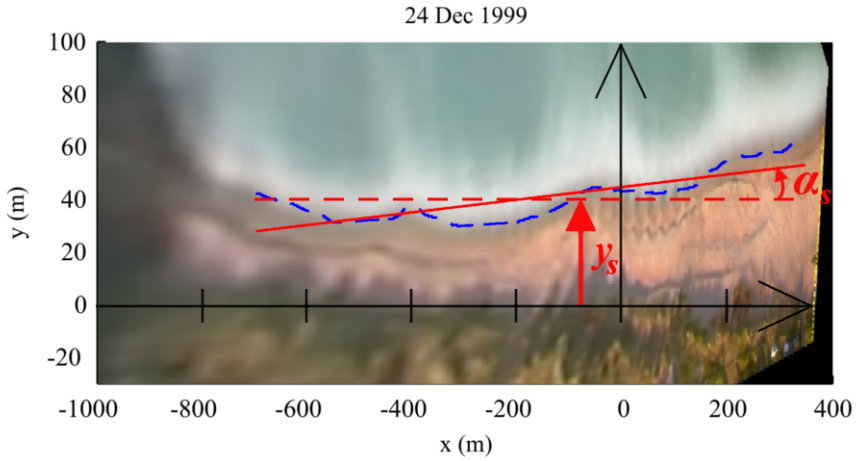

Figure 4.2.: *Digitized shoreline (blue dashed line) represented on the corresponding georectified image at Tairua Beach (24th of December 1999). Angle as and alongshore averaged cross shore position ys (red dashed line) are extracted from the linear fit (solid red line) to the measured shoreline.*

shoreline to the amount of wave energy involved in alongshore sediment transport. This leads to a calibrated and validated shoreline rotation model for Tairua Beach.

4.2.1. Location

Tairua Beach is located in New Zealand North Island, on the east of the Coromandel Peninsula (see Figure 4.1). The local coastal morphology is characterised by extinct volcanoes forming rocky shores intersected by numerous sandy pocket beaches.

Tairua beach is approximately 1.2 km long and embayed in between two headlands, Pumpkin Hill to the north and Paku Hill to the south. The sediment distribution is fairly uniform on the upper profile of the beach with a median grain size of approximately 300 μm. The average significant wave height in the Bay of Plenty is 1.4 m with 6 m observed during large storms and the tidal range is limited to 2 m. As a result the beach tends to exhibit intermediate to more reflective beach states characterised by a steep cross-shore profile and one subtidal bar [*Smith and Bryan* 2007].

The present paper focuses on two large scale morphodynamic processes concerning the shoreline, its cross-shore migration and its rotation previously described in *van de Lageweg et al.* [2013] and *Bryan et al.* [2013]. Smaller scale features have also been observed and studied at Tairua Beach such as beach cusps [*Almar et al.* 2008] and rip channels [*Gallop et al.* 2011, *van de Lageweg et al.* 2013].

4.2.2. Morphological data

A camera was set up on Paku Hill in 1999 as part of the Cam-Era network of the National Institute of Water and Atmospheric Research (NIWA, NZ). 600 images are averaged over 15 minutes every

hour of daylight. Seven years of images from 1999 to 2006 have been georectified on a 0.5 × 0.5 m grid following methodology in *Heikkila and Silven* [1997]. Shorelines have been extracted at 0.5 m above mean sea level (Figure 4.2) by comparing the ratio of the red and blue levels between sandy areas and water areas (see *Smith and Bryan* [2007]). Results are presented in Figure 4.3.

The morphology of the shoreline is highly dynamic and exhibits varied characteristic planform profiles such as curved shapes (April to June 2000), straight shapes (February to May 2005), or oblique shapes (November to December 1999, February to November 2003).

Significant cross-shore migration events can be observed. In July 2000 the shoreline eroded significantly. A similar event occurs in February 2005 with lower amplitude. Migration can also occur on longer time scales such as the shoreline progradation event observed between December 2001 and April 2002.

Rotation events appear clearly in the dataset. Compared to the 7-year mean shoreline orientation, the positive angle (Cartesian convention) of the shoreline in December 1999 (see shoreline angle as in Figure 4.2) decreases until March 2000, describing a clockwise rotation. Another clockwise rotation is observed due to the erosion at the shoreline southern extremity in March 2003. An anticlockwise rotation occurs during the last months of 1999 due to accretion at the southern extremity of the beach. The temporal evolution of as can be easily seen in Figure 4.7.

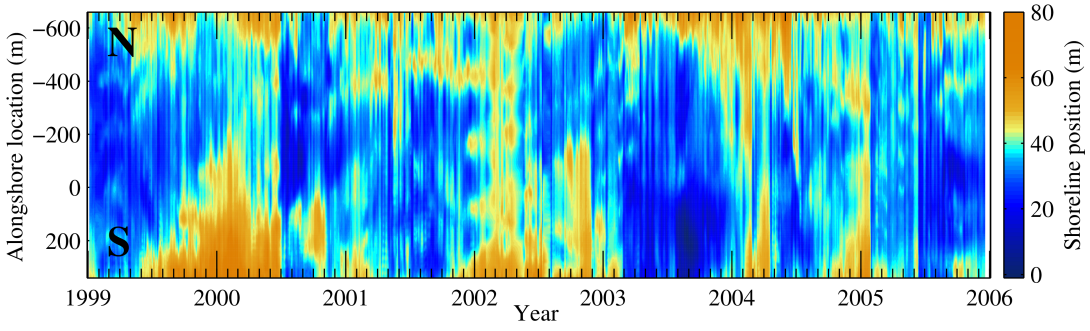

Figure 4.3.: *Shoreline cross-shore position (colorscale) extracted from video images during 7 years at Tairua Beach. S an N indicate the south and north of the beach respectively.*

4.2.3. Wave data

To compensate for a lack of long term wave measurements in the area, a SWAN wave model [*Booij et al.* 1999] was nested into the WaveWatch III CFSR Reanalysis Hindcast (0.5° output grid) computed by the National Oceanic and Atmospheric Administration (NOAA, US). Five nodes have been used to generate 2D spectral wave boundary conditions along the SWAN wave model domain boundaries. Moreover the CFSR wind field was included in the model.

The calibration and validation were based on the measurements of one offshore buoys deployed by the Bay of Plenty Regional Council in the south of the Bay and three 6-week periods of wave data measured at Tairua Beach at 8 m water depth in 2011 (not shown here).

4.3. Shoreline modes

4.3.1. Methods

4.3.1.1. Principal Component Analysis

Principal component analysis (PCA) is a linear analysis performed by diagonalising the covariance of a matrix describing a signal along two dimensions (here along time and space). By definition, the resulting eigenvectors are orthogonal and correspond to spatial profiles of the considered signal (here the shoreline) called PCA modes (or Empirical Orthogonal Functions (EOF)). The amount of variability of the original signal accounted by a specific mode is given by its corresponding eigenvalue. PCA is a purely mathematical method that does not take into account any information about the external conditions at the beach.

4.3.1.2. Canonical Correlation Analysis

Canonical Correlation Analysis (CCA) allows us to partially overcome the limitations of the PCA. CCA is also a statistical linear analysis decomposing a bi-dimensional signal into orthogonal modes. However, this analysis takes into account external forcing parameters, which in this case is the wave climate. The principle of the CCA is to decompose iteratively both the shoreline signal and the wave forcing signal into orthogonal modes by maximizing the correlation between the temporal functions corresponding to these modes.

In the present case, the spatial modes (CCA modes) are shoreline alongshore profiles (as in the PCA). The wave climate is described by a limited number of parameters and the wave climate modes are linear combinations of these parameters. Here, four parameters are used: the cross-shore and alongshore component of the wave energy available for sediment transport E_x and E_y respectively, the peak period Tp and the ratio of the peak period over the mean period Tp/Tm. These parameters have been integrated, supposing that it is the rate of change of the shoreline position that can be related to the external forcing parameters and not directly the position itself. Another approach would be to differentiate the shoreline signals in time. However, this led to lower correlations.

The fact that the CCA generates shoreline modes and wave climate modes so that the temporal functions associated with these modes exhibit the highest correlations does not mean that the shoreline modes contribute significantly to the overall variability of the original shoreline signal. In case of a significant contribution, CCA modes can be used to forecast shoreline behaviour (see *Larson et al.* [2000], *de Alegria-Arzaburu et al.* [2010]). Here, this is not attempted. Rather the study of the CCA modes allows building a semi-empirical rotation models for the shoreline at Tairua Beach.

4.3.2. Results and discussion

The four first shoreline PCA modes are presented in Figure 4.4. The two first PCA modes are significant with R^2 values (0.62 and 0.17 respectively) clearly above the 95 % level (0.04) (see PCA R^2

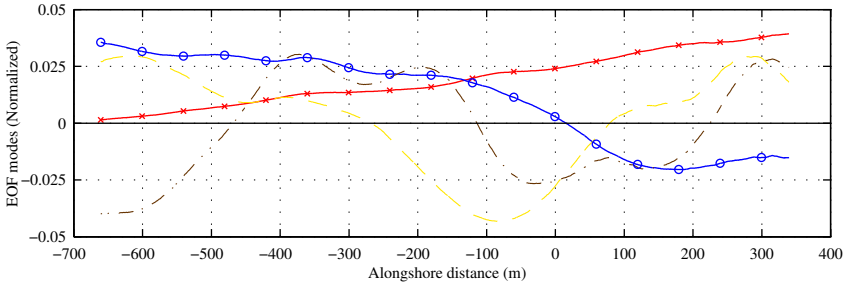

Figure 4.4.: *PCA modes for the shoreline at Tairua Beach. First mode: red line and crosses. Second mode: Blue line with circle. Third mode: yellow dashed line. Fourth mode: dash-dotted brown line.*

in Table 4.1). Together they account for more than 70 % of the overall variability of the measured signals.

Table 4.1.: *PCA modes R^2 coefficients, CCA modes correlation coefficients r and R^2 coefficients.*

Modes	1	2	3	4
PCA R^2	0.62	0.17	0.05	0.04
CCA r (*)	0.79	0.49	-	-
CCA R^2	0.21	0.06	-	-

* Only two modes are computed during the CCA as only the two first PCA modes are significant and used to generate the filtered signals used in the CCA.

Both modes describe combined rotation and migration processes. The first EOF represents a significant migration at the south of the beach ($x > 0$ m) and very limited changes at the north. Therefore beach progradation is associated with an anti-clockwise rotation and vice-versa. This mode accounts for 62 % of the shoreline variability. The second mode accounting for 17 % of the shoreline variability shows the opposite behaviour and exhibit a pivotal point towards the southern extremity of the beach ($x = 0$).

The PCA allows extracting migration and rotation modes, possibly mixed, that are significant in the overall behaviour of the shoreline at Tairua Beach. However, it is still very difficult to discover which physical external forcing parameters are involved in driving these modes. The CCA analysis is designed for this task. Its power is improved if the CCA analysis is performed not on the original timeseries, but on the combined signal from the first two modes of the PCA analysis. In this case, the CCA only generates two modes (see Figure 4.5).

The first mode represents a combined migration and rotation. As for the first EOF, shoreline progradation is associated with anti-clockwise rotation. Interestingly, the second mode describes a migration with no associated rotation meaning that all the rotation captured by the CCA is described by the first mode.

Although the correlation between the temporal functions associated to the CCA spatial modes and the temporal functions associated to the wave climate modes (not shown here) are significant (see CCA r in Table 4.1), this does not mean that the spatial modes are significantly contributing to the variability of the measured shoreline. However, this is the case at Tairua since the alongshore

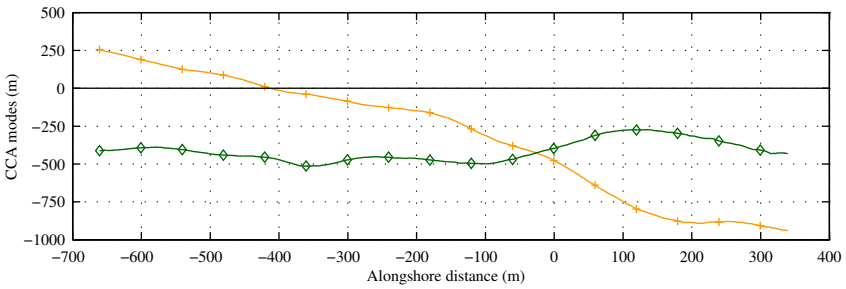

Figure 4.5.: *CCA modes for the shoreline at Tairua Beach. First mode: orange line and pluses. Second mode: green line and diamonds.*

averaged R^2 coefficients of the first and second mode (0.21 and 0.06 respectively) are above the 95 % significance level (0.04).

Figure 4.6 shows the CCA modes loadings, meaning the correlations between the temporal functions corresponding to the CCA modes and the wave climate parameters timeseries. It can be immediately observed that the first CCA mode of the shoreline is fully (-0.97) negatively correlated with E_y, indicating a strong relation between the amount of wave energy involved in the alongshore sediment transport and the shoreline rotation rate. The second mode is highly positively correlated (0.67) to the ratio (T_p/T_m), suggesting a possible difference of erosion related to swell and wind waves.

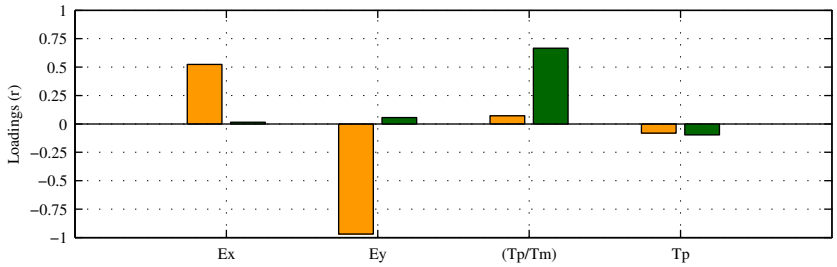

Figure 4.6.: *Wave climate parameters loadings for the shoreline CCA modes. First mode: orange bars. Second mode: green bars.*

As shown by *Larson et al.* [2000] or *de Alegria-Arzaburu et al.* [2010], CCA can be used to perform shoreline position forecasts. Indeed, since CCA associates spatial shoreline modes with wave climate modes, any wave climate can be projected onto these modes. The resulting corresponding temporal functions can be assimilated to the spatial mode temporal functions due to their high correlation and therefore be used to generate a forecast of the shoreline profile.

Several attempts were made in the present case, but the forecasting ability was not significant except in the case of shoreline orientation. This is due to the hypothesis of linearity assumed by the CCA. In the next section, a model is build using the linear relationship between E_y and the shoreline rotation rate underlined by the CCA.

4.4. Modelling shoreline rotation

4.4.1. Semi-empirical models formulations

Shoreline rotation in embayed beaches has already been described [*Ojeda and Guillén* 2008, *Bryan et al.* 2013] and modelled [*Turki et al.* 2013b]. This latter model is based on the hypothesis that the shoreline rotation rate can be related to the alongshore component of the wave energy flux. In agreement with this hypothesis, the CCA performed in the previous section suggests a linear dependency between the shoreline rotation rate and the alongshore component of the wave energy available for sediment transport E_y. This assumption can be expressed by:

$$\frac{d\alpha_s}{dt} = K^*(mE_y + n), \tag{4.1}$$

$$E_y = Ecos(\theta)sin(\theta), \tag{4.2}$$

$$K^* = \frac{1}{T_d L \sigma_{y_s}}, \tag{4.3}$$

where α_s is the shoreline orientation, E is the wave energy assimilated to the square of the significant wave height (m^2) and the peak incident wave angle θ. K^* is a constant inversely proportional to the length of the shoreline L (1200 m), the standard deviation of the shoreline σ_{y_s} and a characteristic time T_d equal to one day. Factors m and n are free dimensionless parameters of the model. In addition, the initial value of the shoreline angle α_{s,t_0} is also set as a free parameter. The numerical integration of the model is performed using a 4^{th} order Runge-Kutta scheme. Free parameters are computed using a particle swarm optimization algorithm [*Ebbesen et al.* 2012].

4.4.2. Results

The rotation model was first run to hindcast the full 7-year dataset of observations at Tairua Beach. Results are presented in Figure 4.7 and indicate that the hindcast is qualitatively and quantitatively good. The root mean square error *RMSE* (see Table 4.2) is below 50 % of the standard deviation of the measured angle timeseries, resulting in a high Brier skill score (*Bss*) of 0.79. The R^2 coefficient (0.79) shows the ability of the model to account for the angle fluctuations.

Table 4.2.: *Root mean square error (RMSE), R^2 and Brier skill score Bss for the shoreline angle 7-year hindcast (grey) and the 4-year forecast obtained using 3 years of training (see Figure 4.7).*

Time Period	*RMSE*	R^2	*Bss*
1999-2006	0.007	0.79	0.79
1999-2002	0.008	0.83	0.76

Then the ability of the rotation model to forecast the shoreline orientation was evaluated (see Figure 4.7). To achieve this, the model was trained over a 3-year time period from 1999 to 2002. The outcomes were assessed on the following 4 years of measurements (see Table 4.2).

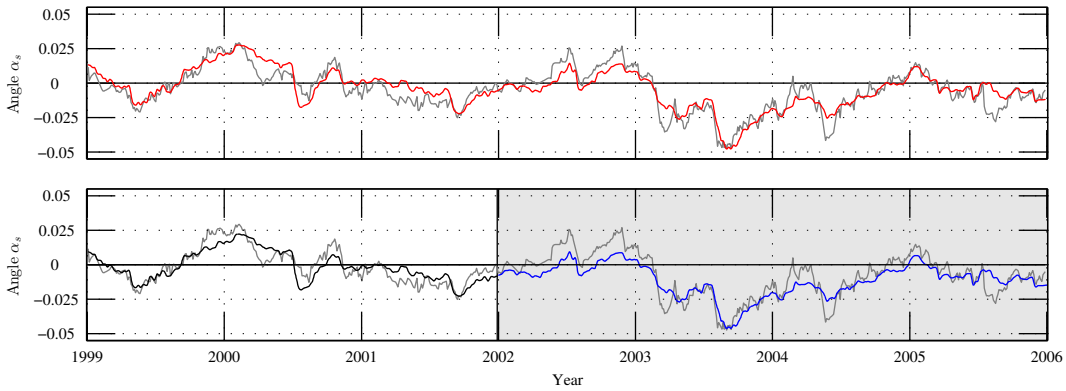

Figure 4.7.: *Top panel: 7-year hindcast of the shoreline rotation model for the shoreline orientation (red line). Bottom panel: 4-year forecast (blue line) of the shoreline orientation using 3 years of training (black line). The 4-year evaluation period for skill computation is shaded in grey. Grey lines represent observations.*

The model simulates accurately the evolution of the shoreline angle during the 4 years following the 3-year training period. The high R^2 coefficient (0.83) shows that the model can forecast relative orientation fluctuations. Moreover, it is able to describe the trend of the shoreline angle evolution, resulting in a low *RMSE* value (0.008) and a high Brier skill score of 0.76 similar to the value obtained for the hindcast. This shows the reliability of the model formulation to describe the rotation of the shoreline at Tairua Beach.

4.5. Conclusion

Linear statistical analyses such as PCA and CCA are efficient in characterising shoreline spatial modes. When using CCA, the modes are extracted by assuming linear relationships between these and the wave climate forcing parameters. Therefore, unless the processes described by the CCA modes depend linearly on the forcing parameters as it is the case for the shoreline rotation, the method does not lead to a reliable forecast of non-linear phenomena such as the cross-shore migration or the shoreline.

Nevertheless, these analyses improve the understanding of the overall system and allow making assumptions on the morphological behaviour of a beach system. At Tairua Beach, the alongshore component of the wave energy available for sediment transport controls the rotation of the beach shoreline. As an immediate result, a shoreline rotation model has been proposed, exhibiting high correlations with the observations and excellent Brier Skill Scores. The CCA also showed the significance of the ratio of peak over mean period suggesting the possible role of the swell in the erosion of the shoreline. Further work is therefore needed to investigate this effect on the shoreline morphodynamics.

4.6. Acknowledgements

The authors would like to thank Wietse van de Lageweg for the shoreline dataset that required a long and patient labour, Shawn Harrison for his precious ideas regarding the setting of the wave model and Christopher Daly for the assistance with video image georectification and for the wave data used to calibrate the SWAN model.

Chapter 5

Contrasting behaviour of an embayed beach shoreline and barline

B. Blossier [(1)], K.R. Bryan [(2)], C.J. Daly [(3)] and C. Winter [(1)]

[(1)] MARUM, Center for Marine Environmental Sciences, University of Bremen, Leobener Strasse 28359 Bremen, Germany.
[(2)] Coastal Marine Group, Faculty of Science and Engineering, University of Waikato, Hamilton, New Zealand.
[(3)] Department of Civil and Environmental Engineering, University of the West Indies, St. Augustine, Trinidad and Tobago.

In review at *Journal of Geophysical Research: Earth Surface*

5.1. Abstract

Using seven years of video imagery collected at the typical single-barred embayed beach Tairua Beach (New Zealand), the behaviour of the shore and nearshore sandbar of such beaches is investigated. Combining semi-empirical modelling with two methods of Principal Component Analysis (PCA), the dominant modes of the shore and bar system are extracted and related to physical processes. Simultaneous behaviours dominate the system, accounting for 87 and 97 % of the shoreline and barline cross-shore migration respectively. A contrasting mode describes opposed migrations of the shoreline and barline that relates to incident wave energies lower or larger than the equilibrium energies defined by the concomitant shoreline and barline positions. A joint mode accounts mainly for migrations of the barline and shoreline in identical directions and relates to wave energies falling in between the equilibrium energies. In addition, this second mode relates potentially to the embayed beach breathing process, suggesting its possible extension to nearshore sandbars and therefore the entire embayment. The simultaneous modes explain 55 an 33 % of the shoreline and barline rotation, rather described by two subsequent asynchronous modes. This agrees with the different drivers involved in the rotation of the shoreline (wave obliquity) and the barline (alongshore gradient of wave energy) in the models. Shore and bar different response times explain the observed desynchronisation of the migration and rotation which advocates for a strong limitation of coupling effects between shore and bar at the scale of the embayment, showing that simultaneity arises from identical or correlated drivers.

5.2. Introduction

In a context of economic growth accompanied by technical and social progress over the past century, the rising value of coastal areas has induced a significant increase in anthropogenic pressure along all coastlines [*Small et al.* 2000, *Small and Nicholls* 2003, *Nordstrom* 2004]. Embayed beach locations are of particular interest, for instance in New Zealand [*Healy and Soomere* 2008] or in northwest Morocco [*Mrini et al.* 2012], where rocky headlands can provide spectacular development sites. In between the headlands which partially limit the influence of wind and waves, coastal embayments provide ideal conditions for recreation. Therefore with the improvements of transport infrastructure, what were local small-sized settlements at the beginning of the last century have become popular recreational areas today.

Embayed beaches form due to the accumulation of sand in between headlands. Sand is supplied by local rivers, longshore transport mechanisms or comes directly from the continental shelf. Embayed beaches are common in natural settings as they account for 50% of the world's coastline [*Short* 1999]. They are also common in urban littoral areas either because cities have been initially built in sheltered bays, or because groynes and breakwaters, built to limit shoreline erosion or to create commercial and leisure harbours, constitute artificial headlands such as in Barcelona, Spain [*Ojeda and Guillén* 2008] or extend existing ones as in Tangier, Morocco [*Chaibi and Sedrati* 2009].

Various issues are related to the increase of anthropogenic impact on embayed beach shorelines. Enhanced by the fact that sediment supply has been reduced on many embayed beaches due to river damming (for instance in Tangier [*Chaibi and Sedrati* 2009]), the progressive construction of dwellings on the coastal dunes has progressively increased the risks related to flood hazards [*Bryan et al.* 2013]. Although embayed beaches are usually sheltered, complex hydrodynamic currents funnelled by the influence of headlands [*Short* 1999, *Dehouck et al.* 2009, *Gallop et al.* 2011, *Castelle and Coco* 2012, *Daly et al.* 2014] regularly cause fatal accidents [*Short and Hogan* 1994, *Brander* 1999]. The understanding of the underlying hydro- and morphodynamic processes is therefore critical for decision makers to design regulations protecting not only the littoral environment, but also private property and human life.

The morphodynamics of embayed beaches are the result of a combination of physical processes acting at different spatial and temporal scales. Micro-scale sediment transport induced by the local wave field and the underlying nearshore current leads to the emergence of features such as beach cusps (typical size around $O(10\text{ m})$) that relate to daily scales [*Almar et al.* 2008] or rip channels ($O(100\text{ m})$) that relate to weekly scales [*Castelle and Coco* 2012]. These features, evolving rapidly in time but little in space, are the most commonly publicly-recognised beach features. At larger scales ($O(1\text{ km})$), embayed beaches exhibit morphodynamic patterns at the scale of the embayment. These processes involve the shoreline area of the beach as well as the potential nearshore sandbars of the embayment [*Turki et al.* 2013b, *van de Lageweg et al.* 2013, *Blossier et al.* 2016]. Occurring usually on monthly to interannual timescales [*Ojeda et al.* 2011, *Splinter et al.* 2011], these processes may be less evident to the casual observer but are more hazardous to coastal infrastructure due to their larger spatial amplitude.

Large scale embayed beach morphodynamics depend on its type of profile. The beach profile is mainly controlled by the local grain size distribution and the external wave conditions. According

to *Wright and Short* [1984], fine sand and steep wave conditions drive the beach profile towards a dissipative state characterised by a mild slope and several nearshore sandbars parallel to the shore. Conversely, coarse sand and low wave heights favours shoreward cross-shore sediment transport driving the beach towards a reflective state characterised by a berm and a steep slope resulting from welding of the nearshore sandbars at the shoreline. The variation of external wave conditions related to the natural variability of the climate induces beach state transitions towards the dissipative or reflective state during which the morphodynamic patterns mentioned in the previous paragraph occur. In particular, at single-barred embayed beaches, the shoreline and the sandbars are found to migrate in the cross-shore direction during these transitions [*van Maanen et al.* 2008, *Ojeda and Guillén* 2008, *van de Lageweg et al.* 2013, *Blossier et al.* 2016].

In addition to the type of profile, embayed beach morphodynamics are also controlled by local geometrical settings. *Short* [1999] and *Castelle and Coco* [2012] defined typical flow circulations and morphodynamic patterns of embayed beaches and related them to their geometry. For this characterisation, *Castelle and Coco* [2012] uses the parameter δ^* of time-averaged surfzone width fitting in an embayment length. Low values ($\delta^* < 6$) are related to flow and morphological patterns dominated by the local geometry. In case of high beach curvature, the flow field exhibits a cellular circulation with one central rip whereas it is characterised by two headland rips for low beach curvature. High values of δ^* (above 16 for low beach curvature, more than 30 otherwise) are related to long embayments where the beach exhibits the patterns of an open beach. Typically, 4 or more rip channels are found along the shoreline of the embayment in addition to two headland rip channels. Intermediate hydrodynamic and morphodynamic patterns are found for intermediate values of δ^*.

In embayed environments characterised by a large value of δ^*, shorelines have been found to rotate (La Barceloneta (Spain), $\delta^* = 24$ [*Ojeda and Guillén* 2008, *Turki et al.* 2013b]; Collaroy-Narrabeen (Australia), $\delta^* = 33$ [*Harley et al.* 2011]; Tairua (New Zealand), $\delta^* = 31$ [*van de Lageweg et al.* 2013]). The rotation results from a contrasting evolution of the beach profile at the embayment extremities. Either the shoreline accretes at one side and erodes at the other, or the erosion (sedimentation) is more important at one extremity than at the other. *Clarke and Eliot* [1982] and *Turki et al.* [2013a] related shoreline rotation to alongshore sediment transport by performing a Principal Component Analysis (PCA) of upper beach sediment volumes and shoreline planform shapes respectively. *Turki et al.* [2013b] confirmed the role of alongshore sediment transport by simulating shoreline rotation using a semi-empirical model. Using a more comprehensive process-based model, *Castelle and Coco* [2012] confirmed the role of longshore currents and explained that shoreline rotation is favoured in embayed beached of intermediate lengths (1 to 4 km) due to a balance between the limited influence of the headlands and the limited amount of sand that needs to be transported along the shore. However, performing a PCA of shoreline shapes and upper beach sediment volumes respectively, *Harley et al.* [2011] and *Harley et al.* [2015] showed that varying cross-shore adaptations of the beach profile along the embayment related to alongshore varying wave energy conditions can also induce shoreline rotation. At single-barred embayed beaches, not only the shorelines were found to rotate for large values of δ^* but also the barlines (La Barceloneta, Bogatell (Spain) [*Ojeda et al.* 2011], Tairua Beach (New Zealand)[*van de Lageweg et al.* 2013, *Blossier et al.* 2016]). Using a semi-empirical model, *Blossier et al.* [2016] showed that the rotation of the barline could be associated with the cross-shore migration of the barline caused the wave breakpoint location varying

along the embayment due to alongshore gradients of wave energy induced by the headlands.

The shoreline and sandbars which form the main components of the beach profile are nearly always studied separately. Shorelines have been extensively studied because their location and the associated beach width are the primary parameters in evaluating flooding and erosion hazards. On the other hand, sandbar studies rather relate to their role as constitutive elements of the global beach morphology (e.g. the *Wright and Short* [1984] beach state model) and their consecutive influence on large scale coastal morphodynamic patterns. However, the shoreline and nearshore sandbars, as constitutive elements of the beach profile description, can strongly interact. Recent studies focus on intermediate sized morphological features such as rip channels. *Castelle et al.* [2010a;b] explained in-phase and out-of-phase patterns of shoreline and barline rip channels by looking at the areas of shoaling and breaking waves over the outer bar crest. *Price and Ruessink* [2011] showed the influence of the subtidal bar state on the intertidal bar state of a double-barred beach. At the single-barred Tairua Beach, *van de Lageweg et al.* [2013] showed a clear coupling between the intermediate sized features (O(100 m)) of the shoreline and barline when these were sufficiently close to each other (cross-shore distance below 130 m).

Different methods have been used to study the behaviour of embayed beaches such as observational studies [*Hsu and Evans* 1989, *Harley et al.* 2011; 2015], process-based modelling [*Castelle and Coco* 2012, *Daly et al.* 2014; 2015] and semi-empirical modelling [*Turki et al.* 2013b, *van de Lageweg et al.* 2013, *Blossier et al.* 2016]. Observational analyses attempt to find relations between natural forcing and morphodynamic patterns by means of statistical instruments. For example, the PCA decomposes morphodynamic temporal and spatial signals into spatial Empirical Orthogonal Functions (EOFs) and their associated temporal functions. As mentioned earlier, this has been used to characterise the behaviour of embayed beach shorelines, such as in *Clarke and Eliot* [1982] who found pivotal points describing alongshore sediment exchanges along Warilla beach (N.S.W, Australia) as nodal points of EOFs. *Miller and Dean* [2007b] attempted to describe the beach profile response to external hydrodynamic forcing by studying the cross-correlation of the temporal functions with the timeseries of nearshore parameters such as the wave height or the angle of incidence. *Harley et al.* [2011] and *Harley et al.* [2015] used the PCA to explain the relevance of cross-shore sediment transport in shoreline rotation. Nevertheless in the latter study, the authors emphasized on the difficulty of interpreting EOFs in terms of physical processes and indicated that a prior in-depth understanding of a study site is required in order to formulate an interpretation.

Semi-empirical modelling approaches allow the simulation of beach profile elements using a limited number of primary processes and require an accurate calibration of the secondary processes that supposedly remain constant at the considered location, at a relevant spatial and temporal scale. Compared to process-based modelling relying on an in-depth description of hydro- and morphodynamic processes, the semi-empirical approach reduces drastically the computation costs by focusing on the primary drivers of the considered morphological pattern. Such models have been proposed for nearshore sandbar migration [*Plant et al.* 1999; 2006, *Splinter et al.* 2011, *Blossier et al.* 2016], for shoreline migration [*Yates et al.* 2009, *Davidson et al.* 2010; 2013, *Jara et al.* 2015] as well as for shoreline rotation [*Turki et al.* 2013b] and nearshore sandbar rotation [*Blossier et al.* 2016]. In essence, migration models associate an equilibrium location of the shoreline (or barline) to the intensity of the incoming wave energy. In the case of nearshore sandbars, migration is limited by a factor which takes into account the amount of wave energy dissipated over the bar [*Splinter et al.*

2011, *Blossier et al.* 2016]. Shoreline rotation has been associated with the amount of wave energy involved in the alongshore sediment transport [*Turki et al.* 2013b, *Blossier et al.* 2015] whereas bar rotation has been shown to better relate to the alongshore gradient of wave energy along the embayment [*Blossier et al.* 2016].

The present paper aims at improving the understanding of the relation between the behaviour of the shoreline and the barline on single-barred embayed beaches at the scale of the embayment. Principal component analysis and semi-empirical modelling are combined to extract and explain the simultaneous and asynchronous behaviours of the shoreline and barline. On one hand, PCA provides a clear ability to divide variance between dominant patterns of variability, but has no ability to explain why those patterns occur. On the other hand, semi-empirical modelling can provide insight into the forcing related to the patterns extracted by the PCA. Our analysis of the barline and shoreline together will allow an understanding of how, and to what extent, they evolve interdependently (and can they be treated independently in, for example, modelling exercises). We undertake our combined analysis of shoreline and barline behaviour at Tairua Beach, a typical example of a single-barred embayed beach located in the north island of New Zealand. Seven years of video imagery data previously presented in *van de Lageweg et al.* [2013] are studied. First, shoreline and barline cross-shore migration and rotation are simulated using semi-empirical models. Then two different PCAs are performed on the observations as well as on the shoreline and barline profiles reconstructed using the models' outcomes. The migration of the shoreline and barline is found to be generally simultaneous but not strongly coupled, which means that their migration respond at the same time to the same forcing but the knowledge of the behaviour of one is not critical in forecasting the behaviour of the other. The rotation of the shoreline and barline is found to be more asynchronous. Characteristic response times of these processes are compared, showing that under energetic conditions the barline responds much more quickly than the shoreline even if, on average over the seven years, it responds at a slower pace due to limited wave breaking over its crest.

5.3. Study area and external conditions

5.3.1. Geological characteristics

Tairua Beach is an embayed beach located along the east coast of the New Zealand north island, in the Coromandel peninsula (Figure 5.1). This peninsula is a region of ancient volcanic activity [*Booden et al.* 2012] accounting for its rugged topography. Along the eastern coastline, rocky shores are intersected by numerous embayed beaches resulting from local sediment supply by rivers or by-passing effects.

Tairua beach is 1.2 km long with two headlands, Pumpkin Hill at the north and Paku Hill at the south, extending seawards approximately 600 m from the dune foot. The beach is partly hindered from waves by Shoe Island located 3 km east of Paku Hill [*Bryan et al.* 2013] and approximately 1 km long from north to south (see Figure 5.1).

Tairua beach is mainly impacted by easterly and north-easterly long-travelling swell and storm waves. Offshore significant wave heights may reach 6 m during storms but are only 1.4 m in av-

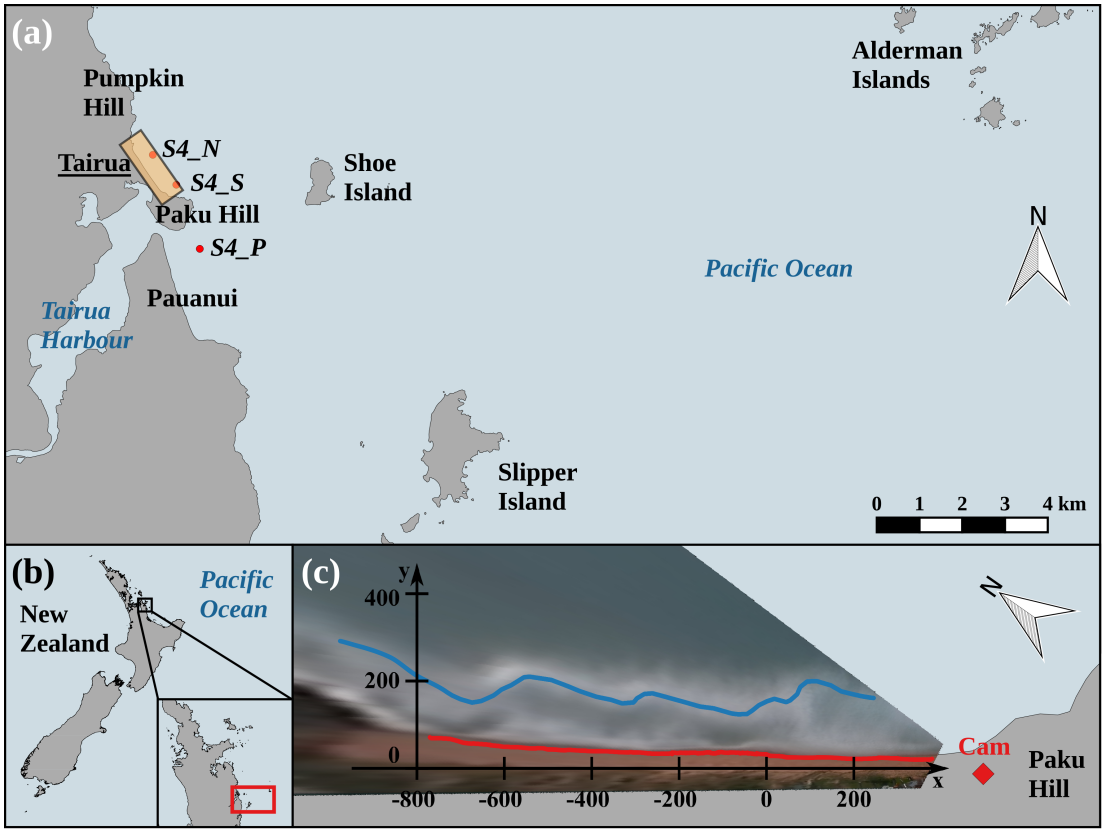

Figure 5.1.: *Location of Tairua (a) in the north island of New Zealand (b) in the Coromandel peninsula (b, inset, red rectangle shows extension of (a)). The yellow rectangle in (a) shows the area of study which is represented rotated and in detail in (c). The red dots* ***S4_N****,* ***S4_S*** *and* ***S4_P*** *show the locations of the instruments used to validate the wave model. An example of extracted barline (27/06/2003, blue) and shoreline (25/06/2003, red) is depicted in (c) over the georectified low tide image of the 27/06/2003 and the local reference frame used in the present study.*

erage. The beach is located in a micro-tidal environment with a tidal range varying between 1.2 and 2 m and is constituted of well-sorted medium sand ($d_{50} \approx 300$ μm). As a result, Tairua exhibits a single distinct shore-parallel sandbar and shows intermediate beach states mostly ranging from longshore bar and trough (LBT) to transverse bar and rips (TBR). The lower shoreface slope is approximately 0.02 [*Blossier et al.* 2016] whereas the upper beach slope is rather steep (≈ 0.2, see *Smith and Bryan* [2007]). Transient intertidal bars can appear along Tairua Beach shoreline but they are not taken into account in the present paper.

The beach exhibits regular successive progradation and retreat events as well as shoreline and barline rotations [*Bryan et al.* 2013, *van de Lageweg et al.* 2013, *Blossier et al.* 2016]. Smaller scale morphological features have also been observed such as beach cusps [*Almar et al.* 2008] and rip channels [*Gallop et al.* 2011]. A clear coupling between the small scale features of the barline and shoreline has been shown by *van de Lageweg et al.* [2013]. However these features are not the main concern of the present paper which rather focuses on the morphodynamics of the shoreline and

barline at the scale of the embayment.

5.3.2. Wave data in the Bay of Plenty

Reliable wave data at Tairua Beach are necessary to drive the semi-empirical models over the seven years of observations. There is no permanent wave buoy or other instrument deployed in the vicinity of Tairua Beach, but one buoy has been installed in 2003 90 km south of Tairua, 6 km southeast of Motiti Island in deep water by the Bay of Plenty Regional Council (BoPRC) and has provided continuous bulk wave spectrum parameters every hour since then.

To obtain the wave characteristics at Tairua Beach, a regional wave model was set-up and applied for the Bay of Plenty, nested within the global WaveWatch III hindcast model from the National Oceanic and Atmospheric Administration (NOAA). The main driver of the SWAN model is the new Climate Forecast System Reanalysis (CFSR) homogeneous dataset of hourly 0.5° spatial resolution winds from the National Centres for Environmental Prediction (NCEP). The model was calibrated using the data of the BoPRC buoy, resulting in a slight increase of the white capping dissipation to compensate for a slight overestimation of the significant wave heights.

To validate the model, observations were collected during three 6-week periods in March-April, August-September and October-November 2011 at three different locations in the vicinity of Tairua Beach, at 8 m depth. S4 instruments developed by InterOcean were used to measure the pressure and horizontal velocity above the sea floor. Two were deployed at the extremities of Tairua Beach and **S4_P** was deployed at the north of Pauanui Beach, located immediately south of Paku Hill (see their locations on Figure 5.1). At these locations, the modelled significant wave height H_s shows high R^2 coefficients ranging from 0.51 to 0.83 and low root mean square error (*RMSE*) ranging from 7 to 15 cm. The wave angle of incidence shows a R^2 coefficient of 0.27 at the BoPRC buoy for all wave conditions, increasing to 0.68 for H_s above 2 m [*Blossier et al.* 2016].

5.3.3. Shoreline and barline data

Since 1998, cameras have been installed at Tairua Beach (see Figure 5.1)) as part of the Cam-Era network developed and maintained by the National Institute for Water and Atmospheric Research (NIWA). The camera is mounted on Paku Hill and records hourly timex images resulting from the averaging of 600 images acquired over 15 minutes. In total, seven years of images are used in the present study covering the 1999-2005 time period.

The extraction of the shoreline and barline data has been performed in *van de Lageweg et al.* [2013]. The images were first undistorted and then georectified over a 0.5 x 0.5 m grid using the pinhole camera model calibrated with ground control points following *Heikkila and Silven* [1997]. Shorelines have been extracted by comparing the ratio of blue and red colours strongly varying at the interface between the water and sand areas following *Smith and Bryan* [2007]. Shoreline elevations have been defined by the corresponding tidal levels computed by the NIWA numerical model [*Walters et al.* 2001]. A correction has been applied to account for set-up, following *Bowen et al.* [1968]. The barlines have been extracted by fitting a second order polynomial to each cross-shore intensity pixel line of the rectified images and extracting the maximum intensity. The cross-shore

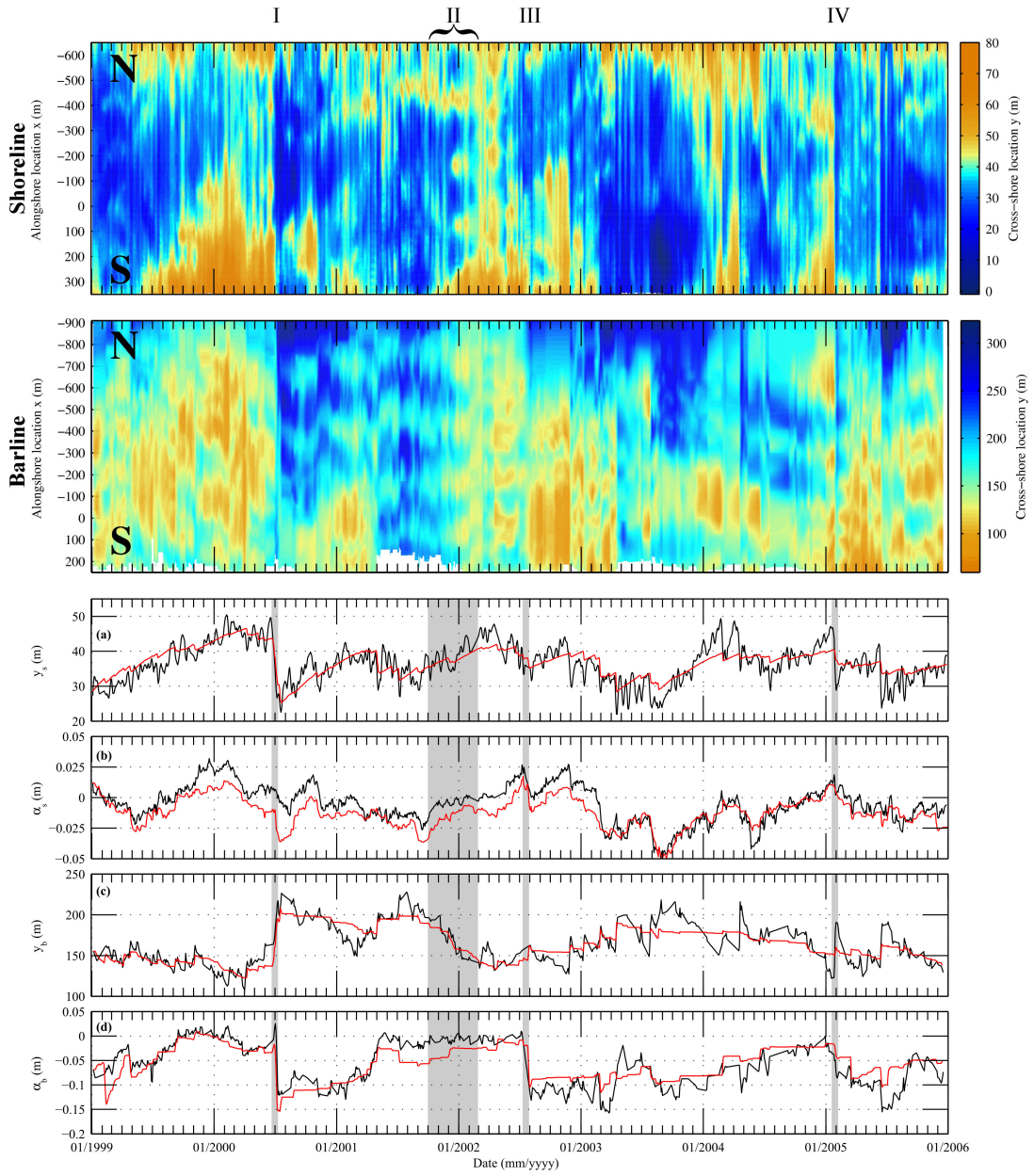

Figure 5.2.: *Panels (a) and (b): Shoreline (a) and barline (b) planform shapes derived from 7 years of camera imagery at Tairua Beach [van de Lageweg et al. 2013]. Colorscales are different for both panels. Brown is related to more reflective beach states (shoreline seawards and barline shorewards). Blues is related to more dissipative beach states (shoreline retreated and barline seawards). Panels (c-f): Observations (black lines) and semi-empirical models results (red lines) for the shoreline cross-shore position y_s (c), shoreline orientation α_s (d), barline cross-shore position (e) and barline orientation (f). Gray areas represent Events I, II, III and IV.*

errors in the dataset were assessed by *van de Lageweg et al.* [2013] to range from 2 to 12 m for the shoreline position. Following *van Enckevort and Ruessink* [2001] and *Ruessink et al.* [2009], a value of 10 m has been determined for the barline position [*Blossier et al.* 2016]. The digitized shoreline and barline planform shapes are presented in Figure 5.2, panels (a) and (b), in the local reference frame shown in Figure 5.1, panel (c).

Different morphodynamic behaviour of the shoreline and barline can be observed. At intermediate scales, rip channels emerge, grow and disappear for the barline (e.g. from September 2000 until July 2002) and the shoreline (e.g. from December 2001 until July 2002) with some possible coupling (January 2002) studied in *van de Lageweg et al.* [2013]. At the scale of the embayment, large migration and rotation events occur. To study these processes, the alongshore-averaged cross-shore position and the orientation have been computed for each extracted shoreline (y_s and α_s respectively) and barline (y_b and α_b respectively) by linearising each of them along x (panels (c-f) in Figure 5.2). Four events have been selected to illustrate the beach behaviour.

Event I and IV show transitions towards more dissipative states with strong erosion of the shoreline (15 to 25 m) and large offshore migrations of the barline (50 to 75 m). These events exhibit as well strong rotations of the barline in the counter-clockwise direction, mainly due to a larger offshore migration of the barline at the north compared to the south (see panel (b)). Shoreline rotation occur as well in the same direction but is very limited (-0.007 to -0.012 or 7 to 12 m over 1 km). Event II shows part of the transition of the beach towards more reflective states with progradation of the shoreline (15 m) and shoreward migration of the barline (50 m). During this event, the shoreline rotates in the clockwise direction (+0.025 or 25 m over 1 km) and the barline orientation does not change. Event III exhibits very little migration of the shoreline and barline, however large counter-clockwise rotations are observed for the shoreline (-0.025) and the barline (-0.125).

Other large scale morphodynamic processes can be observed such as the variability of the curvature of the shoreline and barline. The shoreline exhibits very low curvatures (e.g. February 1999, January 2002, June 2005) and larger curvatures (e.g June 1999 until June 2000, February to April 2004). The bar exhibits the same patterns with low curvatures (e.g March 1999, February to June 2002, January 2005) and larger curvatures (e.g. June 1999 until June 2000, June 2003 until January 2004). This observations can be related with caution to the embayed beach breathing mode presented in *Ratliff and Murray* [2014].

The complexity of the morphodynamic processes involved in Event I to IV shows the difficulty of assessing the potential dependance and interdependence of the migration, rotation and curvature. The present study focuses mainly on the migration and rotation processes as they can be described by means of semi-empirical models and dominate the behaviour of Tairua Beach as shown later section 2.5. The curvature is discussed in sections 5.5.2.3 and 5.6.4.

5.4. Methodology

5.4.1. Semi-empirical models

Four semi-empirical models based on existing literature are used in the present study to simulate the morphodynamics of Tairua Beach in terms of alongshore-averaged cross-shore position and orientation of both the beach shoreline and barline. The first model describes the cross-shore position of the beach shoreline and is based on the formulation of *Yates et al.* [2009]. However, rather than using different free coefficients for the accretion and erosion of the shoreline, only one coefficient is used. As the model was found not to be able to describe long-term trends with these settings, the shoreline position y_s is decomposed as a part described by the model y_s' and a linear trend, similar to *Davidson et al.* [2013]:

$$y_s = b_s.t + e_s + y_s', \tag{5.1}$$

$$E_{eq,s} = a_s.y_s' + d_s, \tag{5.2}$$

$$\frac{dy_s'}{dt} = C_{y_s}\sqrt{E}(E - E_{eq,s}) = C_{y_s}\sqrt{E}(E - a_s.y_s' - d_s) \tag{5.3}$$

where b_s and e_s are the linear trend coefficients, $E_{eq,s}$ is the equilibrium energy linearly depending on the current position of the shoreline y_s' with coefficients a_s and d_s. E is the incident wave energy at time t and C_{y_s} is a calibration coefficient.

Combining Equations 5.1, 5.2 and 5.3 leads to the following model for y_s:

$$\frac{dy_s}{dt} = C_{y_s}\sqrt{E}(E - a_s.y_s - d_s + a_s b_s t + a_s e_s) + b_s, \tag{5.4}$$

$$= C_{y_s}\sqrt{E}(E - a_s.y_s + a_s b_s t + c_s) + b_s, \tag{5.5}$$

$$c_s = a_s e_s - d_s \tag{5.6}$$

where the migration rate depends now on four free coefficients C_{y_s}, a_{y_s}, b_s and c_s.

The second model describes the rotation of the shoreline and its formulation is based on the results of a statistical linear analysis [*Blossier et al.* 2015] showing a clear relationship between the shoreline rotation rate and the amount of wave energy available for alongshore sediment transport [*Komar and Inman* 1970]. These observations are in agreement with the model of *Turki et al.* [2013b] and therefore the present shoreline rotation model is a simplified formulation of their model assuming an equilibrium orientation of the beach shoreline perpendicular to the incoming wave direction θ. The formulation of *Turki et al.* [2013b] is:

$$\frac{d\alpha_s}{dt} = 2\frac{K}{L^2 h^*}\rho_w g H_{b,0}^2 c_{g,b}\sin(\theta - \alpha_s)\cos(\theta - \alpha_s), \tag{5.7}$$

with α_s the shoreline orientation, K a coefficient accounting for the sediment properties, L the length of the beach, h^* the closure depth, ρ_w the water density, g the gravity acceleration, H_b the breaking

wave height and $c_{g,b}$ the wave group celerity at breaking. Linearly expanded to the first order for small values of α_s, using wave height values at 8 m depth and neglecting the variations of the wave group celerity, the formulation is simplified to:

$$\frac{d\alpha_s}{dt} = C_{\alpha_s} E\left[\sin(\theta)\cos(\theta) - \alpha_s \cos(2\theta)\right], \tag{5.8}$$

with C_{α_s} a free parameter of the model.

The barline parameters are modelled by the semi-empirical models developed and validated in *Blossier et al.* [2016]. The barline cross-shore migration is described by:

$$E_{eq,b} = a_b.y_b + b_b, \tag{5.9}$$

$$f_b(H_s, H_b) = \min\left(\left[\frac{H_s}{H_b}\right]^p, 1\right), \tag{5.10}$$

$$\frac{dy_b}{dt} = C_{y_b}\sqrt{E}(E - (a_b.y_b + b_b))f_b(H_s, H_b) \tag{5.11}$$

with y_b the cross-shore position of the barline, $E_{eq,b}$ the corresponding equilibrium wave energy, f_b a morphodynamic damping factor related to the morphodynamic activation of the bar and depending on the ratio of breaking wave height at the bar crest (H_b) over the offshore significant wave height at 8 m depth, p a coefficient equal to 8 and C_{y_b}, a_b and b_b free coefficients of the model. The breaking wave height H_b over the bar crest follows:

$$h_{y_b} = \beta(y_b - \langle y_s \rangle) + h_{bar}, \tag{5.12}$$

$$H_b = \gamma h_{y_b} \tag{5.13}$$

with β the mean slope of the lower beach profile set to 0.023, $\langle y_s \rangle$ the time- and alongshore-averaged position of the shoreline, h_{y_b} the water depth above the bar and h_{bar} the averaged height of the sandbar set to 1 m. These values are based on eight 150 m-spaced and 600 m long beach profiles measured in April, May and July 2011 at Tairua Beach. γ is the wave breaking parameter set to 0.73 [*Battjes and Stive* 1985].

The barline rotation rate is described by the following formulation obtained by differentiating Equation 5.11 along the alongshore dimension x (see *Blossier et al.* [2016]):

$$\begin{aligned}\frac{\partial \alpha_b}{\partial t} = C_{\alpha_b}\Big[\sqrt{E}\left(\frac{\partial E}{\partial x} - \delta a_b(\alpha_b - \alpha_0)\right) \\ + \frac{1}{2\sqrt{E}}\frac{\partial E}{\partial x}(E - (a_b y_b + b_b))\Big] f_b(H_s, H_b)\end{aligned} \tag{5.14}$$

where C_{α_b}, δ and α_0 are free parameters of the model and the values of a_b and b_b are determined during the calibration of the migration model (Equation 5.11).

The calibration of the barline migration and rotation models is extensively described in *Blossier et al.* [2016]. The present paper provides the calibration and validation of the shoreline models in

section 5.5.1.

5.4.2. Empirical orthogonal functions

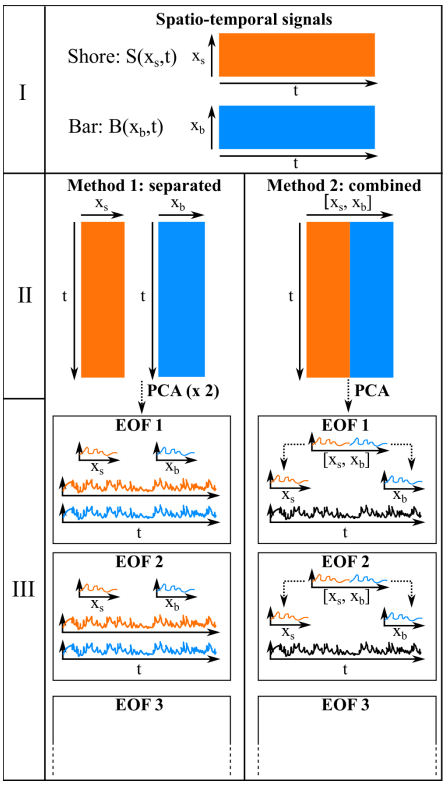

Figure 5.3.: *Description of the two methods used in the present paper to perform the PCA on the shoreline and barline signals. I: shoreline and barline signals as depicted in panels (a,b) in Figure 5.2. II: normalisation of the signals and, in case of the second method, stacking of the shoreline and barline arrays. III: Extraction of the modes with their EOFs and associated time functions. Method 1: the shoreline and barline are associated to their own EOFs with their own associated temporal functions. Method 2: EOFs and their temporal functions are extracted for the couple {shoreline-barline}. Then for each mode, the spatial EOFs accounting for both the shoreline and barline are split to relate either to the shoreline or to the barline. The temporal EOF is common to both signals.*

Principal Component Analysis is used here in order to characterise the behaviour of Tairua Beach shoreline an barline and reveal possible interdependencies between these processes. PCA decomposes a time and space signal described in an array S such as the shoreline and barline signals presented in panels (a,b) in Figure 5.2, into modes consisting of one Empirical Orthogonal Function (EOF) and one associated temporal function. The EOFs are the eigenvectors (P) resulting from the singular value decomposition of the covariance matrix C of signal S (Equation 5.15). The temporal functions in F are obtained by projecting the original signal S onto the spatial EOFs (P) (see Equation 5.16). The eigenvalues λ_i in the diagonal of Λ provide the contribution c_i of each mode i to

the overall variance of the original signal (Equation 5.16).

$$C = S^t S, \qquad \Lambda = P^{-1} C P, \tag{5.15}$$

$$F = SP, \qquad c_i = \frac{\lambda_i}{\sum \lambda_i}, \tag{5.16}$$

In the present study, two different approaches are used to perform this analysis. The first method is used to characterise the individual behaviour of the shoreline and barline. The PCA is performed on the shoreline and barline signals separately, resulting in two sets of independent modes for the shoreline and for the barline with each their corresponding EOF and related time function (Method 1, Figure 5.3). In this paper, the corresponding EOFs are named separated EOFs. In the second method, the modes are extracted for the shoreline and barline simultaneously by performing the analysis on an array S in which the shoreline and barline signals are normalized and stacked along the alongshore dimension. This results in modes consisting each of one EOF accounting for both the shoreline and barline signals and one associated temporal function. The EOFs are split so that two sets of EOFs corresponding to the shoreline and barline are obtained. These EOFs couple for each mode shares the same temporal functions. Therefore these EOFs describe simultaneous evolution of the shoreline and barline timeseries (Method 2, Figure 5.3). In this paper, they are named combined EOFs.

5.4.3. Significance of empirical orthogonal functions

The rule of thumb proposed by *North et al.* [1982] is commonly used to determine if the modes extracted by the PCA are significant at the 95 % level or if they are degenerated, meaning that one significant mode can be represented by the sum of several successive modes (see *Hannachi et al.* [2007], *Reeve et al.* [2008], *Wilks* [2011], *Karunarathna et al.* [2012]). In theory these modes would have the same eigenvalue. The rule of thumb proposes a formulation of the error in the computation of the eigenvalues and states that modes are degenerated if the spacing between successive eigenvalues falls within this error. The error δ_{λ_i} for eigenvalue λ_i is given by:

$$\delta_{\lambda_i} = \sqrt{\frac{2}{N*}} \lambda_i \tag{5.17}$$

where N* is the number of independent samples of the dataset (related to the total number of samples N by the autocorrelation coefficient of the timeseries). A mode is significant if:

$$\lambda_i - \lambda_{i-1} < \delta_{\lambda_i} \tag{5.18}$$

In addition to the rule of thumb, a Monte-Carlo approach based on surrogate data is used here. It is assumed that the beach morphodynamics behave as a red noise in time, which is confirmed by comparing the spectra of beach characteristics (see shoreline position and orientation spectra in Figure 5.4, for the barline see *Blossier et al.* [2016]) to a red noise spectrum (not shown here). Then for each time step, the spectral decomposition of the beach shoreline (or barline) is computed.

Phases are randomly shifted and a new profile is generated by performing an inverse Fourier transform resulting in a full set of profiles $S'(x,t)$ spectrally equivalent to the observed profiles $S(x,t)$. The red noise based surrogate signal S_n is then generated by:

$$S_n(x,t+\Delta t) = r_1(x)S(x,t) + S'(x,t+\Delta t) \tag{5.19}$$

where Δt is the dataset sampling time and $r_1(x)$ is a vector of the first autocorrelation coefficient (in time) at each transect. 1000 surrogate signals S_n are generated. The 95 % level of significance is determined along each transect x_i by computing the 95 % percentile of the $R^2(x_i)$ coefficients computed between measured ($S(x_i,t)$) and generated ($S_n(x_i,t)$ signals.

5.5. Results

5.5.1. Semi-empirical model results

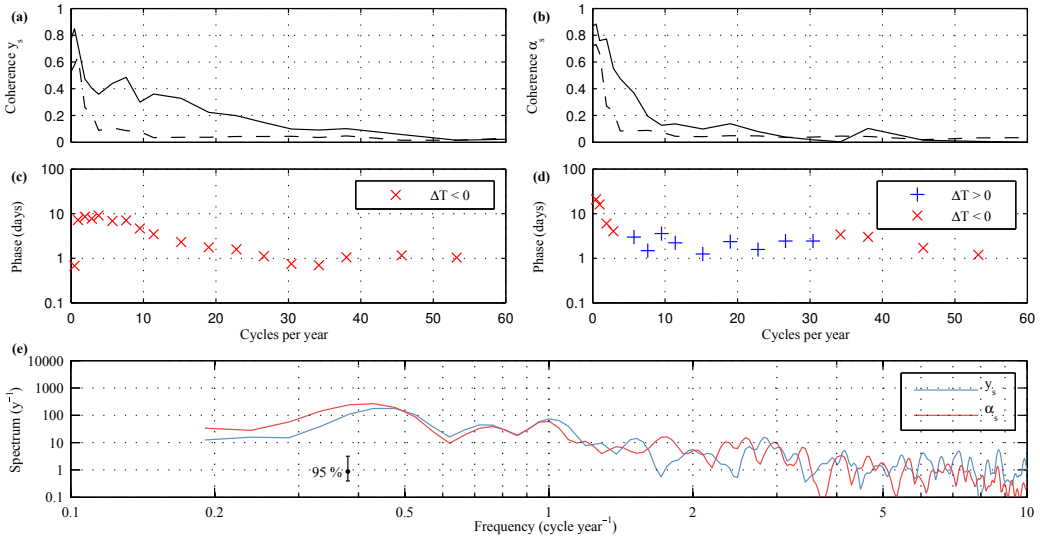

Figure 5.4.: *Panels a, b: Coherence between modelled and measured signals (solid black) and 95 % significance level compared to red noise (dashed black) for y_s (a) and α_s (b). Panels c, d: Phase shift in days for y_s (c) and α_s (d). Blue pluses and red crosses stand for positive and negative time delays respectively. Panel e: Lomb-Scargle spectra for y_s (blue) and α_s (red) computed using 8 DOFs (95 % confidence interval given by the error bar).*

First the four semi-empirical models presented in section 5.4.1 were applied to the shoreline and barline datasets. The models' performance was evaluated using two different approaches following *Blossier et al.* [2016]. First they were calibrated using the entire 7-year dataset and the hindcasts were compared to the observations. Then they were trained over 1 to 5 years of data and the skill of the forecasts is evaluated on the two successive years.

Table 5.1.: *Model skills for 7-year calibrated cross-shore equilibrium parameters.*

Time	Min	Max	σ	*RMSE*	R^2	*Bss*
y_s	24.4	50.3	5.4	2.7	0.73	0.72
α_s	-0.05	0.03	0.01	0.011	0.71	0.49
y_b	108.3	227.8	24.9	13.0	0.73	0.73
α_b	-0.16	0.02	0.04	0.025	0.67	0.66

The hindcasts of the semi-empirical models calibrated over the 7-year dataset are presented in Figure 5.2. The four models (shoreline migration and rotation, barline migration and rotation) do hindcast the overall variability of the Tairua beach bar and shoreline behaviour. 73 % of the variability of the shoreline and barline cross-shore positions and 71 and 67 % of the variability of the shoreline and barline orientations are explained respectively (see Table 5.1). Brier skill scores between 0.6 and 0.8 are good according to the classification of *van Rijn et al.* [2003].

The abilities of the models differ regarding the frequency of observed fluctuations. For the four different beach parameters, the interannual and annual behaviour (period in the range of 1 to 3 years) is well described, since most of the signal variability in each of the four series is located in this range (Figure 5.4 and *Blossier et al.* [2016]). On the other hand, the models do not perform as well regarding short-period fluctuations, with the rotation models performing slightly better than the migration ones. Long-term trends, possibly related to fluctuations with periods longer than the dataset duration, could not be simulated in the case of the shoreline migration model. Indeed, using the initial formulation of *Yates et al.* [2009] with only one free coefficient C_{y_s} for both the erosion and accretion, led either to a net accretion of the shoreline or a clear underestimation of the shoreline cross-shore position fluctuations after 2002. Therefore, a free coefficient b_s was implemented to take this into account (see Equation 5.1).

A coherence analysis between the measured and modelled beach characteristic parameters, presented in Figure 5.4 for the shoreline, confirms the frequency dependent skill of the semi-empirical models. Similar analysis was performed in *Blossier et al.* [2016] for the barline models. All model results are significantly correlated with observations for fluctuations with time periods above 2 weeks. Coherence values above 0.4 related to good model performances are found for fluctuations with time periods longer than 6 weeks and 10 weeks for the shoreline position and orientation respectively, longer than 13 weeks and 18 weeks for the barline position and orientation respectively.

Table 5.2.: *Models skills for 2 years forecasts with increasing training periods.*

Training	y_s		α_s		y_b		α_b	
	RMSE	R^2	*RMSE*	R^2	*RMSE*	R^2	*RMSE*	R^2
1999-2000	33.0	0.01	0.012	0.75	18.4	0.66	0.049	0.62
1999-2001	11.7	0.07	0.012	0.25	21.6	0.40	0.029	0.78
1999-2002	2.9	0.69	0.016	0.91	19.6	0.45	0.038	0.70
1999-2003	3.1	0.67	0.007	0.75	16.6	0.35	0.036	0.62
1999-2004	2.8	0.70	0.008	0.63	13.9	0.44	0.034	0.70

A validation of the models is performed using five different periods ranging from 1 to 5 years for calibration, assessing the model skill on the 2 successive years. Results in terms of root mean square

error *RMSE* and R^2 coefficient are provided in Table 5.2. The four models perform well for 3 years of training or more. In this case, root mean square errors are systematically below the standard deviations of the observed parameters and R^2 coefficients ranges from 0.35 to 0.91.

5.5.2. Empirical orthogonal mode analysis

5.5.2.1. Method 1: separated modes

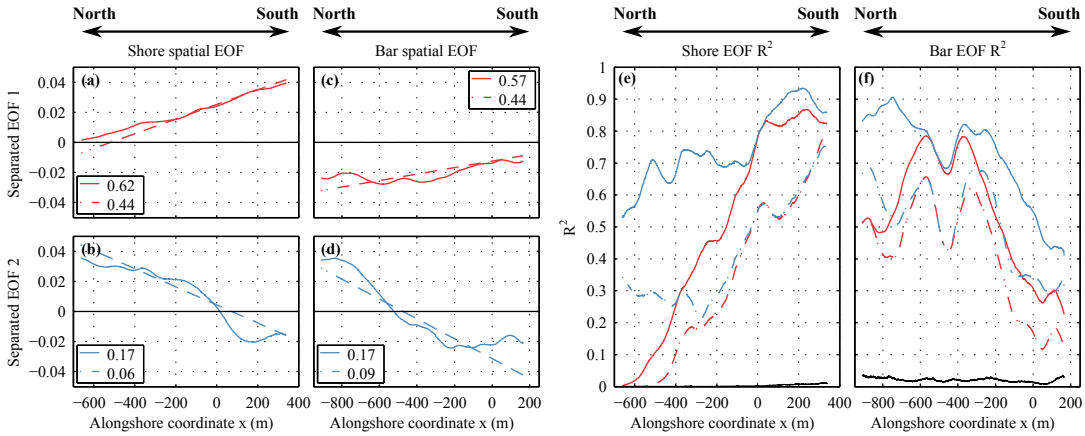

Figure 5.5.: *First (red) and second (blue) EOFs computed for the shoreline (a,b) and the barline (c,d). Solid lines are related to observed data. Dashed lines are related to modelled data. The values of R^2 coefficients at each transect between observations and signals reconstructed using one (red) or two (blue) EOFs are presented for the shoreline (e) and the barline (f). The overall contribution of each EOF to the variability of the observed signals is provided in the legends of a, b, c and d. Black lines indicate the 95 % level using the Monte-Carlo method described in section 5.4.3. Negative (positive) values of x stand for the north (south) of Tairua Beach respectively.*

Empirical orthogonal analysis was applied first independently to the 7-year shoreline and barline datasets following method 1 described in section 5.4.2. The resulting spatial EOFs are represented in Figure 5.5 (panels (a-d)). The analysis of the contribution of each EOF to the variability of the original signal at each transect (panels e, f) showed that only the first two EOFs are significant at the 95 % level for both the barline and for the shoreline and are thus exclusively shown in Figure 5.5. Their significance was confirmed by the rule of thumb of *North et al.* [1982].

The first and second mode related to the shoreline dataset account for 62 and 17 % of the shoreline variability respectively (Figure 5.5, panels (a,b)). The two spatial EOFs are oblique, indicating that the two modes account for a part of the rotation of the shoreline. The alongshore-averaged value of these EOFs is non-zero, being positive (negative) for a positive orientation of the first (second) EOF respectively. The first EOF shows a large amplitude at the south of the beach (x = 400 m) while it is zero at the north (x= -600 m). This means that most of the variability of Tairua Beach shoreline is found at its southern extremity, while the morphodynamics of the northern extremity appear in the second mode. In this case, the amplitude of the EOF is larger at the north. The zero value is found

close to x = 0 m, that is close to the center of the beach, indicating that only a limited migration occurs during rotation events described by this second shoreline mode.

The first and second modes related to the barline dataset account for 57 and 17 % of the barline variability respectively (Figure 5.5, panel (c, d)). Compared to the shoreline modes, the first spatial barline EOF is more parallel to the average coastline orientation (zero-slope). This EOF exhibits a limited positive slope with an alongshore-averaged negative value. Equivalently, associated with negative values of its corresponding temporal EOF, this mode then exhibits limited negative slopes for alongshore-averaged positive values, in opposition to the first shoreline mode. As a result, the bar is found to be more dynamic at the northern extremity of the beach and a slight rotation occurs when the bar migrates. The high variability of the northern extremity is confirmed by the profile of the second spatial EOF exhibiting as well a larger amplitude at the north compared to the south. In this case, a zero value is found at about x = -550 m, and the alongshore-averaged position of the mode is close to zero. Therefore the mode describes a pivotal rotation not associated with any barline migration.

The contributions of each mode to the overall beach variability given along each transect along the shore (see Figure 5.5, panels (e, f)) confirm the previous statements. Indeed, the first shoreline mode explains around 85 % of the shoreline variability at the southern extremity (x between 0 and 375 m). Its contribution decreases almost linearly down to 0 % at the northern extremity (x = -650 m). On the contrary, the second mode does not contribute significantly to explaining the shoreline behaviour at the south but explain up to 60 % of the shoreline behaviour at the north. In total, the modes account for 79 % of the overall shoreline variability.

In the case of the barline, there is not such a clear difference between north and south. The first mode catches 50 % of the barline variability at the north and only 25 % at the south. However most of the barline variability is located in the central part of the beach, for $x$between -700 m and -200 m. There the first mode explains between 60 and 78 % of the barline variability. Interestingly, the second mode, describing mainly a rotation of the barline, does not explain any of the variability in the central part of the beach but accounts for up to 40 % (20 %) of the variability at the northern (southern) extremity of the bar respectively.

The PCA has also been applied to the model outcomes to assess their ability to simulate the dominant modes of an embayed beach. The results are presented in Figure 5.5 (dashed lines). The PCA provides only two modes in this case as the modelled signal is a superposition of a migration and rotation, therefore represented by only two characteristic profiles. There is a good agreement between the spatial modes based on the observations and those based on the models. Trends and alongshore averaged values agree well. Slight differences are found in the shoreline first mode for which the model-related EOF crosses zero at x = -400 m, resulting in a zero contribution to the overall shoreline variability for x < -400 m. In addition, the second barline mode shows a smaller amplitude at the north than at the south contrary to the mode based on observations. As a result this mode does not explain more barline variability at the north than at the south of the beach.

The main difference between the model-based and data-based modes is their overall contributions to the shoreline and barline variability. They necessarily describe less variability as they do not account for spatial alongshore variability by construction. The contributions decreases from 79 % down to 52 % for the shoreline and from 74 % down to 53 % for the barline. Decreases of about 25 % (50 %)

of the contributions of the first (second) modes to the overall shoreline and barline variability are observed respectively. Whereas the decrease of representativity is relatively alongshore uniform for the barline (between 20 and 30 %), it is mainly concentrated at the north of the beach for the shoreline and especially related to a lower contribution of the second shoreline mode.

5.5.2.2. Method 2: combined modes

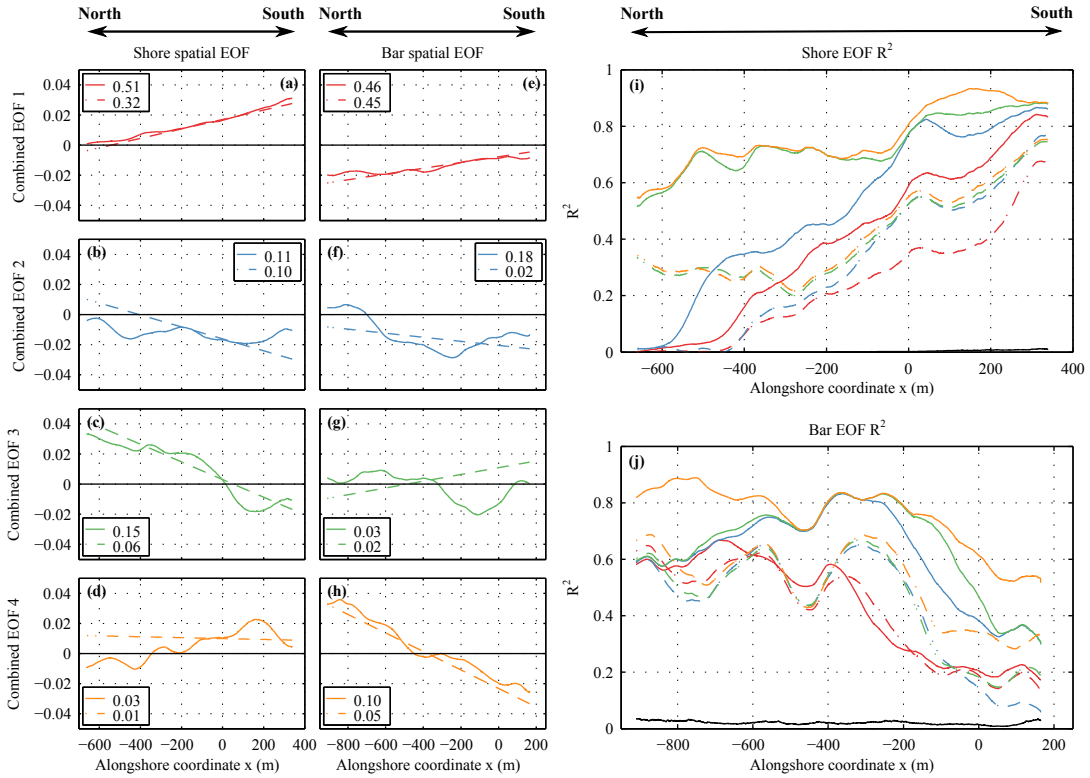

Figure 5.6.: *First (red), second (blue), third (green) and fourth (orange) EOFs computed for the shoreline (a,b,c,d) and the barline (e,f,g,h). The values of R^2 coefficients at each transect between observations and signals reconstructed using one (red), two (blue), three (green) and four (orange) EOFs are presented for the shoreline (i) and the barline (j). The overall contribution of each EOF to the variability of the observed signals is provided in the legends of a, b, c, d, e, f, g and h. Solid lines are related to observed data. Dashed lines are related to modelled data. Black lines indicate the 95 % level using the Monte-Carlo method described in section 5.4.3.*

In this section, the PCA is performed on the shoreline and barline simultaneously so that their spatial EOFs share the same temporal modes as described in section 5.4.2, method 2. This method allows for the dynamic shoreline and barline patterns that occur simultaneously to be characterised, which is useful because morphodynamic patterns that occur simultaneously are potentially coupled, meaning that the barline dynamics and its current state potentially influence the shoreline dynamics and vice versa. This potential coupling is discussed in section 5.6.

The 4 first spatial EOFs as well as the R^2 coefficients between the observations and the reconstructed shoreline (and barline) using 1, 2, 3 or 4 modes are presented in Figure 5.6. The *North et al.* [1982] rule of thumb indicates that the five first EOFs are relevant but considering the comparison of the R^2 values to the 95 % significance level (see Figure 5.6, panels(i, j)), we only discuss the first four in the present study.

The first spatial EOF is comparable to the first spatial EOFs extracted with method 1 (see previous section). For both the shoreline and the barline, the EOF shapes are indeed very similar, describing progradation of the shoreline and shoreward migration of the barline both accompanied by clockwise rotation (and vice versa). However the amount of variability explained by the first modes decreased from 62 to 51 % for the shoreline and from 57 to 46 % for the barline. This is due to the second method, which extracts the main simultaneous beach fluctuations. The non-simultaneous variability of the beach is decomposed into the subsequent modes.

This is particularly clear with the third and fourth modes. These combined modes are characterised by a strong contribution either to the shoreline or the barline and a non-significant contribution to the other beach line. The third mode explains 15 % of the shoreline variability and only 3 % of the barline variability. On the contrary, the fourth mode does not significantly account for the shoreline variability (3 %) but explains 10 % of the barline variability. By comparing the relevant profiles of the third and fourth modes to those extracted separately in the previous section, it appears that the shoreline profile of the third mode can be associated with the second shoreline mode extracted with the first method. Similarly, the barline profile of the fourth mode can be associated to the second barline separated mode.

The association of these modes is confirmed by the profiles of the R^2 values (Figure 5.6, panels (i, j)) showing that the third mode contributes to explaining the shoreline behaviour at the northern extremity of the beach in the same way as the second shoreline mode extracted using method 1. Similarly, the fourth mode contributes to explain the behaviour of the barline at its extremities such as the second mode of the barline extracted separately. The variability explained by the third combined mode decreased from 17 % to 15 % for the shoreline while the variability explained by the fourth combined mode decreased from 17 % to 10 % for the barline.

The second combined (method 2) mode explains a significant amount of variability of both the shoreline (11 %) and barline (18 %) but cannot be related to the modes extracted using method 1. This mode is associated with the retreat or progradation of the shoreline without rotation. Regarding the barline, the second mode describes a complex pattern of mixed “landward migration, landward curvature, clockwise rotation” related to the negative alongshore-averaged value, central deepening and negative slope of the EOF shape. Conversely, this mode can also describe “seaward migration, seaward curvature, counter-clockwise rotation” when the associated temporal EOF is negative. It is interesting to consider this second mode in contrast to the first mode describing a dominant opposing behaviour of the shoreline and barline. Indeed, the second mode describes a joint behaviour since seaward and landward migrations are simultaneous. In general, the mode improves the description of the shoreline variability all along the beach whereas it contributes to the barline variability at the south between x = -650 m and x = 180 m. The combination of the first and second modes extracted with the second method leads to a description of the beach variability close to what was explained by the first two modes extracted using method 1.

The four first model-related modes extracted with method 2 are significant according to the criterion of *North et al.* [1982] except for the second one concerning the barline area. This means that, for the barline, this mode is possibly degenerated with the third mode. However both modes explain very little of the barline variability (2 %). The comparison to the EOF analysis of the observations shows good agreement between the shapes of the first, third and fourth EOFs. In the two latter cases, the agreement is found for the areas where the corresponding data-based modes account for significant variability of the shore-bar system. These areas are the shoreline for the third mode and the barline for the fourth. As for the separated PCA, the variability explained by the model-related modes is lower than for the observations but still significant, decreasing from 51 to 32 % and from 46 to 45 % in the case of the first shoreline and barline mode respectively. It decreases from 15 to 6 % for the third shoreline mode and from 10 to 5 % for the fourth barline mode.

The second mode, which is significant for explaining the beach variability, is not well reproduced by the models. This means that the models are able to describe qualitatively and quantitatively the simultaneous opposing behaviours of the shoreline and barline (mode 1) as well as the non-simultaneous part of their behaviour (mode 3 and 4), but not the joint behaviour related to the overall progradation or retreat of the beach.

5.5.2.3. Modes projections

In order to get a better physical understanding of the PCA decomposition on the barline and shoreline signals, and to compare the spatial EOFs extracted for the shoreline and barline using methods 1 and 2, the squared correlations between the spatial EOFs computed in sections 5.5.2.1 and 5.5.2.2 and three normalized “idealized" orthogonal vectors (ideal shoreline/barline profiles) are presented in Figure 5.7. These three vectors represent an alongshore uniform profile, an oblique profile with zero mean and a hyperbolic cosine-shaped profile with zero mean. Therefore their time variation would represent a migration, a rotation and a breathing [*Ratliff and Murray* 2014] respectively. These profiles have been selected as they represent the most common behaviour of embayed beach shoreline and barline found in the literature, correspond to the model abilities (migration and rotation simulation) and preliminary observations (see section 5.3.3).

The degree to which each of the ideal shapes in panels a-c represent the EOFs in Figure 5.5 (panels (a-d)) and Figure 5.6 (panels (a-f)), is assessed by regressing each EOF against each ideal shape. For example, the R^2 (plotted in panels (d)) is high for the first separated EOF of the shoreline (yellow bar) because this EOF is most similar to the migration shape. The value of R^2 between the model-related EOFs and the breathing profile (lower part of panel f) is always zero since the shoreline and barline signals reconstructed from the models are each based on only two profiles representing a migration and a rotation. In this section, the third mode extracted using method 1 on the observations is considered. However only the shoreline-related third mode is significant according to the rule of *North et al.* [1982]. A discussion on the significance of this EOF is given in section 5.6.4.

The EOFs extracted with method 1 (separated EOFs) decompose the shoreline (yellow bars) and the barline (green bars) signals into first migration (EOF 1, panel (d)), then rotation (EOF 2, panel (e)) and finally breathing (EOF 3, panel (f)) with the contribution of these mechanisms to the overall

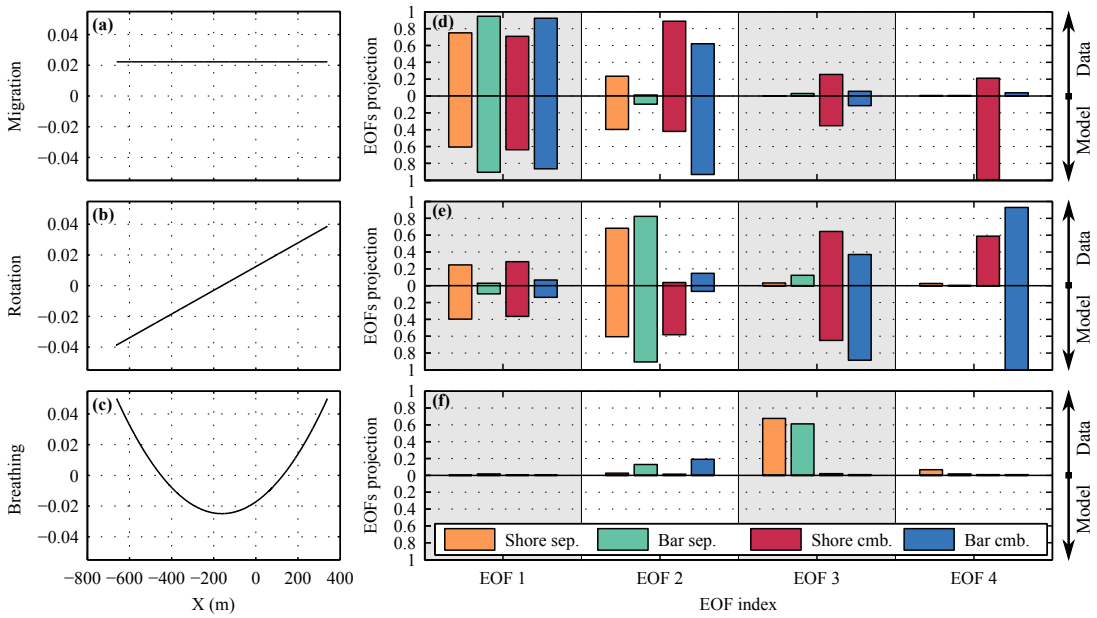

Figure 5.7.: *Left column: three normalized orthogonal ideal alongshore shapes (left column)) related to a migration (top), a rotation (middle) and a breathing (bottom) of the shoreline or barline (presented here for the barline). Right column: R^2 coefficients between the 4 first spatial EOFs obtained with both first and second methods (Figure 5.3) and the three ideal shapes. Orange and red bars represent the R^2 values for the shoreline EOFs extracted separately (method 1) or in combination with the barline (method 2) respectively. Green and blue bars represent the R^2 values for the barline EOFs extracted separately or in combination with the shoreline respectively. Bars above zero stand for data-related EOFs and bars below zero stand for model-related EOFs.*

beach variability decreasing from one to the next. However it is important to notice a significant amount of rotation in the first EOF and of migration in the second EOF related to the shoreline EOF 1, yellow bar, panel (e) and EOF 2, yellow bar, panel (d) respectively). Migration clearly dominates the beach behaviour, followed by the rotation and the breathing. The symmetry of the yellow and green bars between the lower and upper parts of panels (d) and (e) confirms the good agreement between the data- and model-based modes regarding the migration and the rotation of the shoreline and barline.

In agreement with the results presented in section 5.5.2.2, the R^2 coefficients of the first modes extracted with method 1 and 2 are very similar between the two methods of extraction, showing equivalent migration and rotation (yellow and green bars similar to red and blue bars in Figure 5.6, EOF 1, panels (d, e)), confirming the association of the first separated and combined modes. As well, the symmetry of the red and blue bars for the first EOF show that the related processes are well represented in the modelled shoreline and barline.

The second mode extracted with method 2 is dominated by shoreline and barline migration (EOF 2, panel (d)). This mode is poorly represented by the model as mentioned in section 5.5.2.2 (no symmetry of the red and blue bars for EOF 2).

The third mode extracted with method 2 and relevant for the shoreline (red bar, EOF 3, panel (e)) and the fourth mode extracted with the same method and relevant for the barline (blue bar, EOF 4, panel (e)) contain mostly rotation even if some migration is found in case of the shoreline (red bar, EOF 3, panel (d)). The symmetry of these bars show the good agreement between the model- and data-related EOFs. The regression coefficients also emphasize the similarity between the second shoreline EOF extracted with method 1 (EOF 2, yellow bars) and the third shoreline EOF extracted with method 2 (EOF 3, red bars). The same occur for the second barline EOF extracted with method 1 (EOF 2, green bars) and the fourth barline EOF extracted with method 2 (EOF 4, blue bars). This confirms the potential association of these modes already mentioned in section 5.5.2.2.

5.6. Discussion

5.6.1. Model performance

The discussion of the performance of the barline migration (Equation 5.6) and rotation (Equation 5.14) models, assessed using standard evaluation parameters such as the root mean square error, the R-squared coefficient and the Brier Skill score is not repeated here as these have been extensively analysed in *Blossier et al.* [2016]. That study showed that the barline models are able to simulate the behaviour of the barline position and angle from interannual fluctuations (2-3 years) down to 4 to 6 month fluctuations, which is a range actually corresponding to the largest amount of variability of the two signals. Short-term fluctuations potentially associated with the morphodynamics of small scale features such as rip channels are not well reproduced.

The performance of the shoreline models in this study is slightly better compared to the barline models. Indeed, the coherence between observations and models is above 0.4 over a larger frequency range, from the interannual scale down to 4 to 10-week time period fluctuations. Root mean square errors are slightly above half the standard deviation of the shoreline signals, which is comparable to the barline model. As a result, the models obtain fair to good Brier Skill Scores (0.72 and 0.49 for 7-year calibration for the position and the orientation of the shoreline respectively).

The comparison of the model- and data-related modes confirms the ability of the models to simulate most of the variability of Tairua Beach shoreline and barline. Indeed, despite the limitations of the models not being able to simulate intermediate scale features and therefore the shoreline and barline alongshore variability, a general good agreement of the spatial EOFs related to the dominant modes (see Figures 5.5 and 5.6) was found in sections 5.5.2.1, 5.5.2.2 and 5.5.2.3. In addition, the corresponding temporal EOFs agree well with positive and significant (95 % level) correlation coefficient above 0.51 (see Table 5.3). In terms of migration and rotation, the agreement is particularly good for the first EOFs (using either method 1 or 2), as shown by the projections in Figure 5.7, as well as for the second EOFs using method 1 and the third shoreline and fourth barline EOFs using method 2.

However, the models do not simulate reliably the second mode extracted with the second method describing simultaneous shoreline and barline migrations in the same direction. Even though the migration they both represent corresponds relatively well to the migration described by the cor-

responding data-based EOFs (red and blues bars in Figure 5.7, EOF 2, panel (d)), the modelled shoreline EOF contains approximately 60 % of rotation that does not appear in the data-based EOF (see EOF 2, panel (e)). On the contrary, the modelled barline EOF describes less rotation than the data-based EOF and is not significant according to the rule of *North et al.* [1982]. In addition, the data-based barline EOF exhibits a significant curvature (see Figure 5.7, EOF 2, blue bar, panel (f)) that can not be simulated by the model.

The reliability of the models, their robustness (shown by their high skill in forecasting shore- and barline parameters) and their ability to catch and simulate the dominant fluctuations of the cross-shore position and orientation of the shoreline and barline was shown by their good skills and a good agreement between the data- and model-based spatial and temporal EOFs. This enables now to associate the physical processes described in their formulations to the EOF patterns and characteristics in the next sections.

5.6.2. Dominant behaviour

5.6.2.1. Simultaneous behaviour

The PCA using method 1 revealed two dominant modes for both the shoreline and barline at Tairua Beach. These modes describe mixed migration and rotation (their shapes exhibit non-zero alongshore average values and non-zero slopes in the alongshore dimension). The first modes contain a significant amount of migration with average alongshore values larger or equal to the difference between the cross-shore positions of the extremities. Conversely, the rotation largely dominates the second modes with a cross-shore distance between extremities much larger than the averaged cross-shore position.

The modes extracted jointly using the second method are similar to the modes that were extracted separately. From the shapes of the spatial EOFs, it was possible to associate the first combined EOF (method 2) with the first separated EOFs (method 1) in section 5.5.2.2. As well, the third (and the fourth) combined EOFs were associated with the second separated shoreline (barline) EOF respectively. The validity of these associations is confirmed by the good agreement between the corresponding associated temporal EOFs (see Figure 5.8).

These associations enable us to understand the way in which the morphodynamics of the barline and shoreline are connected. The first separated EOFs of the shoreline and barline (see Figure 5.5, panels (a) and (c)) were decomposed over the two first combined modes (see Figure 5.6, panels (a, e, b, f)). The first combined mode (panels (a) and (e)) shows a simultaneous contrasting behaviour with opposed migration directions of the shoreline and the barline and is named *contrasting mode* hereafter. This mode can be associated with the transition of the beach towards more reflective or dissipative states. The second mode (panels (b) and (f)) exhibits a simultaneous joint behaviour of the shoreline and barline with identical migration directions and is referred to as the *joint mode* hereafter. The direction of rotation is the same for the barline and shoreline for the two contrasting and joint modes.

This decomposition of the first modes extracted separately over the two first modes extracted jointly can be related to the amount of variability they explain (62 % compared to 51 and 11 % for the

shoreline, 57 % compared to 46 and 18 % for the barline). In more detail, the contribution of the joint mode in the first separated modes can be observed in the corresponding temporal functions (see Figure 5.8). When the joint mode temporal function (panel (b)) is positive, the shoreline and barline positions defined by the corresponding EOFs are shifted landwards (Figure 5.6, panels (b, f)). This corresponds to the first separated barline temporal function (blue line, panel (a) in Figure 5.8) to be above the contrasting mode temporal function (i.e. landward shift, see Figure 5.5, panel (c)). Similarly, the first separated shoreline temporal function (red line, panel (a) in Figure 5.8) is located below, indicating a landward shift as well (Figure 5.5, panel (a)). On the contrary, when the joint mode temporal function is negative, the shoreline and barline positions defined by the contrasting EOF are shifted seawards. This corresponds to the first separated barline temporal function to be below (seaward shift) the contrasting mode temporal function and the first separated shoreline temporal function to be above (seaward shift).

These observations show that the simultaneous behaviour is dominant at Tairua Beach, as it is described by the first modes extracted separately with method 1 and alternatively by the two first modes extracted with method 2. The majority of the simultaneous behaviour is for the bar and shoreline to move seawards and landwards simultaneously and vice versa. In addition, a significant part of the simultaneous behaviour corresponds for the barline and shoreline to migrate in the same direction.

5.6.2.2. Simultaneous migration

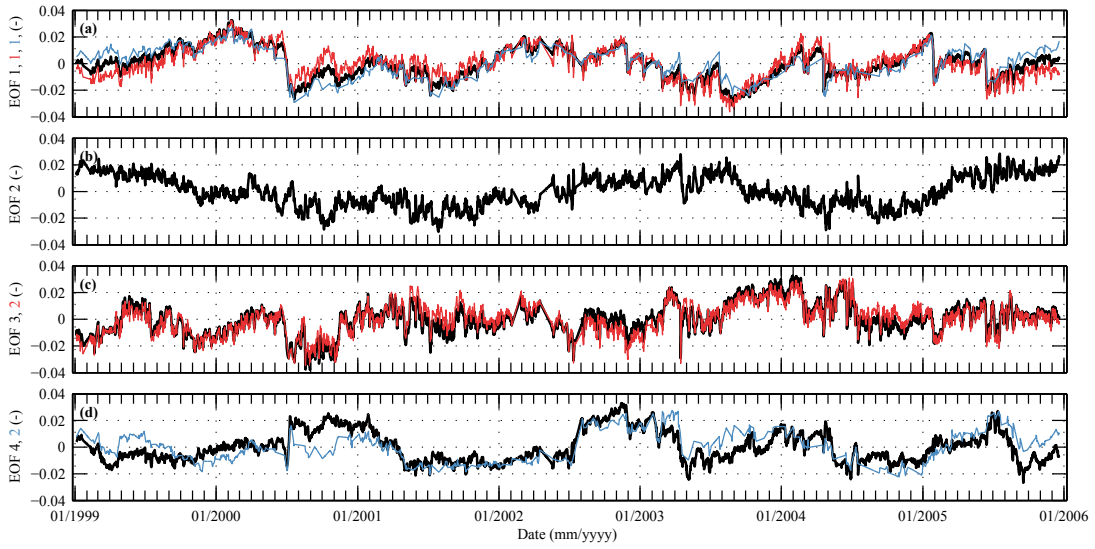

Figure 5.8.: *Temporal EOFs. Black line: Combined (method 2) shore- and barline temporal EOFs ((a): first EOF, (b): second EOF, (c): third EOF, (d): fourth EOF). Red line: Shoreline temporal EOFs (method 1) ((a): first EOF, (c): second EOF). Blue line: Barline temporal EOFs (method 1) ((a): first EOF, (d): second EOF)*

The migration explained by the contrasting and joint modes can be explained by the equilibrium

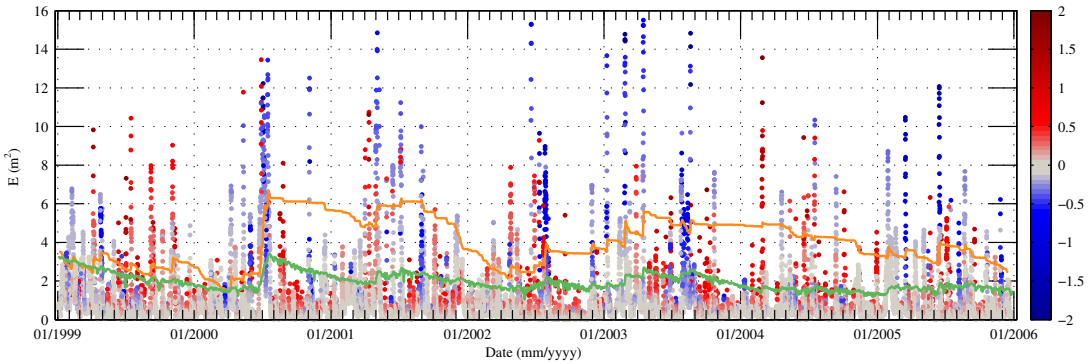

Figure 5.9.: *Orange line: Barline equilibrium energy $E_{eq,b}$. Green line: Shoreline equilibrium energy $E_{eq,s}$. Dots: Incident wave energy at 8 m depth. Colors indicate the corresponding amount of energy available for alongshore sediment transport.*

theory and the related model formulations presented in section 5.4.1, despite the poor representation of the joint mode by the models. The contrasting mode describe barline seaward migration associated with shoreline erosion. According to the migration models' formulations (Equations 5.5 and 5.11), this corresponds to the situation when incident wave energy is higher than the equilibrium energies corresponding to the concomitant barline and shoreline positions ($E > E_{eq,s}$ and $E > E_{eq,b}$). Conversely, the contrasting mode can also describe landward barline migration associated with shoreline progradation, corresponding to an incident energy that is lower than the equilibrium energies ($E < E_{eq,s}$ and $E < E_{eq,b}$). In the same manner, the joint mode describes an overall landward or seaward migration of both the shoreline and barline corresponding to incident wave energy values falling between the equilibrium energy values for the bar and the shoreline (e.g. the equilibrium relationships (Equations 5.5 and 5.11) predict that the bar would move shorewards and the shoreline erode at the same time if $E_{eq,s} < E < E_{eq,b}$).

These relations between the contrasting or joint mode, the incident wave energy and the equilibrium energies shown in the formulations of the models are confirmed by the repartition of the incident wave energy above, below or in-between the concomitant equilibrium energies $E_{eq,s}$ and $E_{eq,b}$ over the 7-year time period covered by the dataset. The equilibrium energies computed by the models are presented in Figure 5.9 as well as the corresponding incident wave energies. Modelled wave energy corresponding to $E > E_{eq,s}$ and $E > E_{eq,b}$ occurs only 7 % of the time but they account for 35 % of the overall wave energy at Tairua Beach during the 7-year period . 85 % of the time, wave energy values fall below $E_{eq,s}$ and $E_{eq,b}$. This accounts for 44 % of the overall wave energy. In total, it is therefore 79 % of the overall incident wave energy that is above or below the equilibrium energies and is likely to drive the contrasting behaviour described by the contrasting mode. Regarding the joint mode, in most cases, $E_{eq,s} < E_{eq,b}$, leading to the most common situation for which $E_{eq,s} < E < E_{eq,b}$. 8 % of the time, the wave energy values correspond to this case, accounting for 20 % of the overall wave energy. When the beach approaches the reflective state and the barline is very close to the shoreline, it is possible to observe $E_{eq,b} < E_{eq,s}$, for instance in early 1999. However this situation is unlikely to happen at Tairua, occuring less than 0.2 % of the time and accounting for less than 1 % of the overall incident wave energy). Therefore in total, 20 % of the incoming wave energy at

Table 5.3.: *Correlations (r) between model- and observation-based temporal EOFs. Bold values are larger than 0.50.*

EOF nb.	Shore	Bar	Shore & Bar
1	**0.83**	**0.88**	**0.88**
2	**0.59**	**0.79**	**0.69**
3	0.05	-0.08	**0.51**
4	-0.04	0.05	**0.68**

Tairua Beach is likely to drive the joint behaviour described by the joint mode.

Using these observations, the ratio of wave energy likely to drive the contrasting mode (79 %) over the wave energy likely to drive the joint mode (20 %) is very similar to the ratio of the variability explained by the contrasting mode (shoreline: 51 %, barline: 46 %) over the variability explained by the joint mode (shoreline: 11 %, barline: 18 %). Thus, this validates the approach of associating the migration described by the contrasting and joint modes with the characteristics of the incident wave energy and concomitant state of the beach described above.

The dominant contrasting and joint modes describe most of the observed cross-shore migration patterns. Indeed, the correlation between the cross-shore positions of the shoreline and barline obtained from the data and computed using the combination of the contrasting and joint modes show that these account for 87 and 97 % of the shoreline and barline migration respectively. Even though the barline and shoreline cross-shore positions can be described to a large extent by the contrasting and joint modes, they do not necessarily migrate at the same rate. In particular, the semi-empirical models described by Equations 5.5 and 5.11 lead for steady conditions of wave energy E_0, wave angle θ_0 close to zero to the following response times:

$$\tau_{y_s} = \frac{1}{C_{y_s}\sqrt{E_0}a_s}, \tag{5.20}$$

$$\tau_{y_b} = \frac{1}{C_{y_b}\sqrt{E_0}a_b f_b}, \tag{5.21}$$

$$\frac{\tau_{y_b}}{\tau_{y_s}} = \frac{C_{y_s}a_s}{C_{y_b}a_b f_b} \approx 0.18\ \tau_{y_s}, \text{ for } f_b = 1. \tag{5.22}$$

with τ_{y_s} and τ_{y_b} the shoreline and barline migration response times respectively.

The response time of the shoreline position (Equation 5.20) ranges from above 170 days ($H_s <$ 1 m) to below 45 days ($H_s >$ 4 m). When the bar is fully activated, which means $H_s > H_b$ and $f_b = 1$, the bar migrates five times more quickly than the shoreline towards its equilibrium position (Equation 5.22). This is always the case for seaward migration as the breaking point is located seawards of the sandbar which is therefore fully activated. However the influence of the damping morphodynamic factor (f_b, Equation 5.10) during calm conditions leads to much slower response. In practice, the response time of the barline in the model is longer than the shoreline response time in 69 % of the evaluated time steps. This difference in behaviour is illustrated by the fact that the contrasting and joint modes explain almost all the barline migration (97 %), but 13 % of the shoreline migration is not explained. 8 % is actually described by the third combined EOF,

accounting for these differences.

The fact that the models, not dynamically coupled, simulate a large amount of the variability described by the contrasting mode (see Figure 5.6, panels (a,e)) advocates in favour of a weak coupling of the shoreline and barline in terms of migration, at the scale of the embayment, during transitions towards more reflective or dissipative states. Regarding the joint mode, despite its mitigated simulation by the models (see Figure 5.6, panels (b, f)), the equilibrium theory involved in the models formulations provides a possible explanation for its origin. Even if this advocates for weak coupling as well, it is difficult at the current stage of the research to provide strong arguments supporting this hypothesis.

5.6.2.3. Simultaneous rotation

The orientation (slope) of the contrasting and joint modes' EOFs can also be explained by the equilibrium theory and the related models formulations presented in section 5.4.1. Indeed, these models' (Equations 5.8 and 5.14) associate shoreline rotation to the amount of wave energy contributing to alongshore transport ($E_y = Ecos(\theta)sin(\theta)$) and barline rotation to alongshore wave energy gradients ($\nabla_x(E)$). Therefore the distributions of E_y and $\nabla_x(E)$ for conditions corresponding to the activation of the contrasting and joint modes are studied here.

For $E > E_{eq,s}$ and $E > E_{eq,b}$, conditions associated to the contrasting mode, the distributions of E_y and $\nabla_x(E)$ are shifted from half a standard deviation towards negative values noticeable by the dominance of blue dots above $E_{eq,b}$ in Figure 5.9. According to the rotation models' formulations (Equations 5.8 and 5.14), this associates barline seaward migration and shoreline erosion to clockwise rotation. For $E < E_{eq,s}$ and $E < E_{eq,b}$, conditions also associated to the contrasting mode, the average values of the distributions of E_y and $\nabla_x(E)$ are close to zero, with however a significant positive skewness for the E_y values that can be related to the large number of red dots below $E_{eq,s}$ in Figure 5.9. This relates shoreline progradation to counter-clockwise rotation. For $E_{eq,s} < E < E_{eq,b}$, conditions corresponding to the joint mode, the characteristics of the distributions of E_y and $\nabla_x(E)$ do not enable the association of any specific rotation direction to the simultaneous progradation of the shoreline and landward migration of the sandbar. This can be related to the small amount of rotation explained by the joint mode (Figure 5.7, EOF 2, red and blue bars, panel (e)).

The simultaneous modes (contrasting and joint) account together for 55 and 33 % of the shoreline and barline rotation respectively. This behaviour is almost completely described by the contrasting mode accounting in particular for clockwise rotation occurring under energetic erosive conditions induced by extreme events and shoreline counter-clockwise rotation occurring during calm accretionary events. As for the cross-shore migration, the good ability of the rotation models (Equations 5.8 and 5.14), not dynamically coupled, to simulate the rotations described by the contrasting mode advocates in favour of a weak coupling of the shoreline and barline rotation at the scale of the embayment. In addition, the remaining variability in the rotation signals (45 % and 67 % for the shoreline and barline respectively) is described separately by the third and fourth joint modes, showing that the shoreline and barline rotations are more independent and are likely to be driven by different processes (see section 5.6.3).

5.6.3. Barline and shoreline rotation related to different drivers.

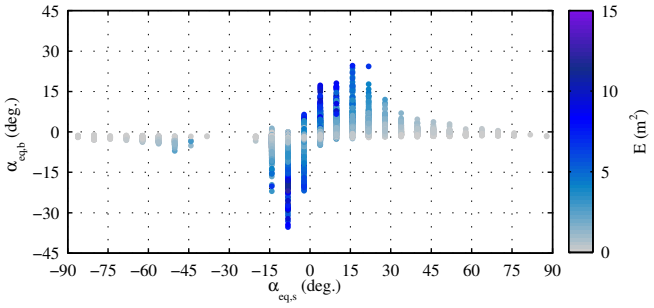

Figure 5.10.: *Equilibrium orientation of the barline $\alpha_{eq,b}$ (see Equation 5.24) on the vertical axis as a function of the equilibrium orientation of the shoreline (see Equation 5.23). Values are given in degrees. The colorscale indicates the intensity of the incident wave energy.*

Considering the good skill of the rotation models (Tables 5.1 and 5.2), their formulations (Equations 5.8 and 5.14) are used to evaluate process differences between the barline rotation and shoreline rotation that would explain their separation over the third and fourth mode using the combined PCA (method 2).

Under steady wave conditions defined by the incident wave energy E_0 and wave angle θ_0, it is possible to define equilibrium angles $\alpha_{eq,s}$ and $\alpha_{eq,b}$ for the shoreline and barline respectively:

$$\alpha_{eq,s} = \theta_0, \tag{5.23}$$

$$\alpha_{eq,b} = \alpha_0 + \frac{1}{\delta a_b}\frac{\partial E_0}{\partial x}, \tag{5.24}$$

These two quantities are represented in Figure 5.10 with their corresponding incident wave energy. $\alpha_{eq,s}$ relates directly to the wave angle of incidence, in agreement with *Turki et al.* [2013b], *Turki et al.* [2013a] and *Blossier et al.* [2015] whereas $\alpha_{eq,b}$ relates to the alongshore wave energy gradient, in agreement with *Bryan et al.* [2013] and *Blossier et al.* [2016]. Figure 5.10 shows that the wave energy strongly influences the relationship between the two equilibrium angles. At high energies ($E > 10$ m^2), they are significantly correlated ($R^2 = 0.65$) with $\alpha_{eq,b}$ being approximately twice $\alpha_{eq,s}$. At intermediate energies ($5 < E < 10$ m^2), the angles are similarly correlated ($R^2 = 0.65$) but $\alpha_{eq,b}$ is only approximately 1.5 times $\alpha_{eq,s}$. For lower energies, ($2.5 < E < 5$ m^2), the correlation remains significant ($R^2 = 0.61$) and the average ratio of $\alpha_{eq,b}$ over $\alpha_{eq,s}$ decreases to 0.73. For E between 1 and 2.5 m^2, $R^2 = 0.57$ and the average ratio of $\alpha_{eq,b}$ over $\alpha_{eq,s}$ is only 0.23. For incident wave energy below 1 m^2, there is no significant correlation and $\alpha_{eq,b}$ falls between -9 and 5°.

These observations lead to the conclusion that the relation between $\alpha_{eq,s}$ and $\alpha_{eq,b}$ depends strongly on the wave energy. In other words, high wave energy conditions induce larger alongshore wave energy gradients in the embayment (and therefore larger $\alpha_{eq,b}$) for similar values of incident wave angle (and therefore similar $\alpha_{eq,s}$). As such, the obliquity of the barline equilibrium angle can be high even for low wave angles of incidence. The absolute value of $\alpha_{eq,b}$ can reach more than 15° (30°)

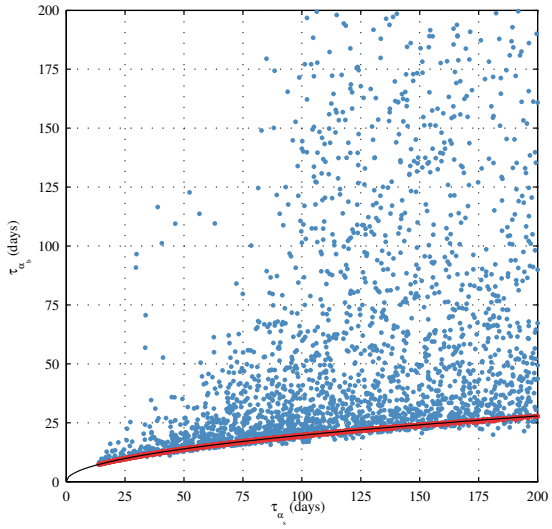

Figure 5.11.: *Red and blue dots represent the response time of the barline orientation τ_{α_b} as a function of the shoreline orientation τ_{α_s}. Red dots correspond to a damping factor $f_b = 1$ and a limited wave incidence $|\theta| < 10°$. The black line represents the relation between τ_{α_b} and τ_{α_s} for $f_b = 1$ and $\theta = 0$ (see Equation 5.27).*

for wave angle of incidence between -5 and 5° (-10 and 10°) respectively. Therefore strong rotations of the bar can be observed during storms even at low angles of incidence. This is the case for Event I and IV (Figure 5.2) during which high waves (H_s = 3.8 and 3 m respectively) and low angle of incidence ($\theta \sim$ -5° and -2° respectively) induce large alongshore negative gradients of wave energy (-3 and -1.2 m) driving large clockwise rotation of the barline while clockwise shoreline rotation occurs but is very limited. On the contrary under low wave conditions, the alongshore wave energy gradient remains low, therefore leading to a rotation of the bar towards α_0 (see Equation 5.24) during calm landward migration conditions (see in Figure 5.2 year 1999, August 2000 - February 2001, year 2004).

Not only are the barline and shoreline equilibrium angles different, but also their characteristic response times towards these equilibria. The formulations of these response times is given by:

$$\tau_{\alpha_s} = \frac{1}{C_{\alpha_s} E_0 \cos(2\theta_0)}, \tag{5.25}$$

$$\tau_{\alpha_b} = \frac{1}{C_{\alpha_b} \sqrt{E_0} f_b \delta a_b}, \tag{5.26}$$

$$\tau_{\alpha_b} = \frac{\sqrt{C_{\alpha_s}}}{C_{\alpha_b} \delta a_b} \sqrt{\tau_{\alpha_s}} \approx 1.97 \sqrt{\tau_{\alpha_s}}, \text{ for } f_b = 1 \text{ and } \theta_0 = 0. \tag{5.27}$$

with τ_{α_s} and τ_{α_b} the shoreline and barline response times respectively. Their values are represented in Figure 5.11. Equation 5.27 provides the relation between τ_{α_s} and τ_{α_b} when the wave angle of incidence is close to zero and the bar morphodynamic damping factor f_b is 1 (see black line and

red dots in Figure 5.11). For these conditions, the barline orientation responds much more quickly than for the shoreline. Oblique wave angles can even increase this difference (blue dots below the black line). However the bar morphodynamic damping factor is frequently smaller than 1, leading to much larger values of τ_{α_b}. In the models, $\tau_{\alpha_b} > \tau_{\alpha_s}$ for 65 % of the evaluated time steps, showing that the barline is less active than the shoreline in general (blue dots above the black line).

Studying the rotation models formulations enabled us to explain the results of the PCAs. Shoreline and barline rotation are driven by different processes that are the amount of energy available for alongshore sediment transport (E_y) and the alongshore gradient of wave energy ($\nabla_x(E)$). These processes are partially correlated as they usually drive the shoreline and the barline both towards positive (or negative) equilibrium angles (Figure 5.11). This partial correlation, as well as the fact that high energy events are mainly associated to negative angle of incidence at Tairua Beach (Figure 5.9) explains the rotation extracted by the contrasting mode. However, the fact that the average ratio between the shoreline and barline equilibrium angles is strongly influenced by the intensity of the incident wave energy, and that in addition the shoreline and barline rotations exhibit different response times contribute to their consequent desynchronisation. This appears in the separation of the two processes over the third and fourth EOF extracted with the joint method (method 2). This advocates for a weak coupling between the two processes that, if existing, does not constitute a primary parameter of the rotations.

5.6.4. Breathing mode

Ratliff and Murray [2014] studied long-term embayed beach shorelines behaviour by modelling alongshore sediment transport between headlands using the model developed in *Ashton et al.* [2001] and *Ashton and Murray* [2006]. They introduced a new mode called breathing that relates to fluctuations in the curvature of the shoreline between positive, zero and negative values. This justified in section 5.5.2.3 the choice of the third arbitrary vector having a hyperbolic cosine-shaped profile. In Figure 5.7, the third shoreline and barline EOFs extracted independently with method 1 correlate significantly with this breathing profile. In addition, regarding the shoreline mode, there is a clear similarity with the third mode EOF extracted by *Short and Trembanis* [2004] at Narrabeen Beach (Australia) and mentioned in *Ratliff and Murray* [2014]. The third shoreline and barline EOFs as well as the amount of variance they explain per beach transect are presented in Figure 5.12 despite the fact that the third barline mode is not significant according to the rule of *North et al.* [1982].

The interpretation of these EOFs in the present context is rather difficult with regards to the limited amount of explained variability (shoreline: 5 %, barline: 7 %). In addition, for the barline, most variability is explained at the south of the beach ($x >$ -100 m) and none is explained at the northern extremity ($x <$ 600 m) (see panel (d)), therefore not agreeing with the breathing process supposed to modify the beach mostly at the center of the embayment and at its extremities. On the other hand, the shoreline mode describes exactly this pattern with 15, 20 and 5 % of variability explained at the northern extremity, at the center and at the northern extremity of the embayment respectively (see panel (c)). The temporal function corresponding to the shoreline third mode (Figure 5.12, panel(e), red line) is dominated by interannual and annual fluctuations.

Regarding the modes extracted using the second method, the joint barline and shoreline EOFs

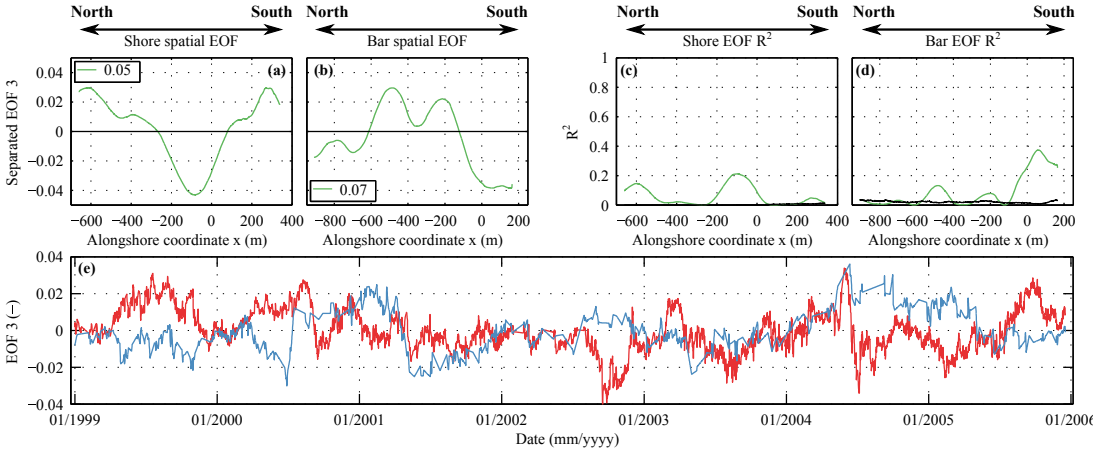

Figure 5.12.: *Third EOFs (green line) computed separately (method 1) for the shoreline (a) and the barline (b). The increase of R^2 coefficients between observations and signals at each transect due to the third mode compared to the two first modes (see blue curves in Figure 5.5, panels (e, f)) is represented by the green lines in panels (c) and (d). The overall contribution of each mode to the variability of the observed signals is provided in the legends of (a), and (b). Black lines indicate the 95 % level using the Monte-Carlo method described in section 5.4.3. Negative (positive) values of x stand for the north (south) of Tairua Beach respectively. Panel (e): Corresponding temporal functions for the shoreline (red) and the barline (blue).*

(EOF 2, Figure 5.6, panels (b, f)) show shapes that could be related to a breathing process. Their correlation with the hyperbolic cosine-shaped profile in Figure 5.7 is weak because these EOF shapes are flattened at the centre of the embayment. However the choice of the hyperbolic cosine-shape in section 5.5.2.3 is arbitrary and could be discussed. The two EOFs are close to zero at the beach extremities, therefore the corresponding modes have low amplitude at these locations. On the other hand, they have larger amplitudes in the central part of the beach, thus corresponding to the fluctuations in curvature related to the breathing process.

The fact that the joint mode is particularly difficult to simulate with the migration and rotation models could relate to the fact that breathing is induced by local headland-hindering effects on the alongshore sediment transport that are not taken into account in their formulations. In addition, the temporal function associated to the joint mode (Figure 5.8) exhibits interannual fluctuations with time periods of 3 to 4 years. This potentially agrees with the characteristic time scales found by *Ratliff and Murray* [2014] for low-angle wave climate, condition which is compatible with Tairua Beach wave climate where 8 % of the wave simulated over 7 years exceed an angle of 45° with the normal to the beach. Interestingly, the association of the joint mode to the breathing potentially extends this process to the entire system shoreline-barline that would appear to be synchronised, therefore inducing an overall change of the beach shape.

5.7. Conclusion

A combined approach using semi-empirical models and Principal Component Analysis has been used in order to characterise and understand the behaviour of shoreline and barline morphodynamics at the embayment scale in a typical example of a single-barred embayed beach environment.

The semi-empirical models have been calibrated and validated using shoreline and barline data extracted from seven years of video images obtained at a typical single-barred embayed beach, Tairua Beach. They showed high skill and reliable forecasting properties in terms of classical evaluation parameters such as root mean square error, correlation and Brier Skill Score, suggesting that they capture the processes responsible for the dominant dynamics of the system. As well, the PCA extracted similar modes from the dataset and the modelled data, confirming the models' abilities to represent the embayed beach's dominant behaviour.

Two PCA methods have been used to extract the dominant patterns of the shoreline and barline morphodynamics first separately and then jointly. Two shoreline and two barline significant independent modes were extracted using the first method, showing the domination of migration over rotation dynamics. Then, four modes extracted using the second method described the combined migration and rotation that appeared as interrelated processes.

This second method provides more insight into the beach behaviour by extracting shoreline and barline modes sharing the same temporal functions, meaning that their inter-relationship can be studied. In this case, the two first modes described a simultaneous behaviour of the shoreline and barline, whereas the third and fourth mode related independently to the shoreline and barline respectively, exhibited the asynchronous behaviour of the beach.

The two first combined modes dominate the behaviour of Tairua Beach and explain most of the observed alongshore-averaged cross-shore migration. The first mode called *contrasting mode* describes the migration of the shoreline and barline in opposed directions so that the shoreline accretes while the barline moves shorewards and vice versa. This mode can be associated to beach state transitions towards more reflective or more dissipative states and dominates the simultaneous behaviour. The second simultaneous mode, called *joint mode*, describes the shoreline and barline migration in the same direction.

The semi-empirical model formulations related to the shoreline and barline cross-shore position equilibrium theories allow insight into the wave conditions that cause these simultaneous modes to be activated. Indeed, opposed migration behaviour can be related to wave energy conditions above or below both the shoreline and barline equilibrium energies, whereas the migration in identical directions is likely to be related to wave energies falling in between the equilibrium energies, likely to occur when the barline migrated far offshore after energetic events.

Interpretations of the simultaneity of the contrasting and joint modes suggest that the shoreline and barline migration may be coupled processes. However the semi-empirical models advocate against this hypothesis by not using any instantaneous shoreline (barline) parameter in the barline (shoreline) model respectively. Migrations occur simultaneously essentially because they answer to the same forcing parameter, the intensity of the incident wave energy. A slight desynchronisation was observed due to the different response times of the shoreline and barline. If the weakness of

the coupling was clearly assessed for the contrasting behaviour, potential coupling associated to the joint mode, not well simulated by the models, cannot be excluded.

In opposition to the joint mode, the contrasting mode extracted a significant amount of simultaneous rotation which could be explained by the formulations of the semi-empirical rotation models and the wave climate properties suggesting a weak coupling between the shoreline and barline. In addition to the simultaneous modes, the joint PCA separated over the third and fourth mode the asynchronous rotation of the shoreline and the barline respectively. Using the rotation models, this separation could be explained by the different drivers involved. The shoreline was found to rotate due to the amount of wave energy available for alongshore sediment transport whereas the barline rotates because of the alongshore wave energy gradient along the embayment. A wave energy varying relationship between the two drivers as well as different resulting response times controlled the separation of the rotation process over simultaneous and asynchronous modes. This confirmed that rotation of the shoreline and barline are largely independent (which supports our choice of formulation in the rotation models).

In addition to these spatial analyses provided by the PCAs, the models provided insights about the response time of the beach shoreline and barlines. Under energetic conditions, in both cases of the migration and rotation, the barline responds more quickly than the shoreline under energetic conditions. However due to the limitation on the sandbar morphodynamics occurring when waves are not breaking in a large proportion over its crest, its response time during calm conditions is usually longer than the shoreline response time. This contributes to the desynchronisation of the rotation and migration signals of the shoreline and barline, supporting the hypothesis of a weak coupling involved in the migration described in the contrasting mode and the overall rotation process.

Finally, the third shoreline separated mode and the joint mode could be potentially associated to the breathing mode described in *Ratliff and Murray* [2014]. This hypothesis would explain the weak ability for the models used in the present study to simulate the joint mode as they do not account for local headland hindering critical in simulating the breathing. This potential association would extend the applicability of the breathing mode to the whole beach system including nearshore sandbars. However further research is needed to assess this potential extension.

If the present study shows that the overall behaviour of a single-barred embayed beach does not exhibit a strong coupling between the shoreline and the barline, this does not mean that this coupling does not exist. It appears clearly as a secondary process at the scale of the embayment over the considered time period. However, it could actually improve the description of the shoreline and barline migration and rotation by the semi-empirical models which, *in fine*, simulated approximately 70 % of the overall shoreline and barline cross-shore position and orientation. In addition, the present study assumes no sediment transport imbalance during the observation period. If net import or export of sediment would occur at the embayment, the shore-bar system could migrate in the cross-shore direction, which is not allowed in the models. Further research is needed to investigate the sediment balance at the embayment and its effects on the shore-bar system.

5.8. Acknowledgments

The present research was funded through the DFG (Deutsche Forschungsgemeinschaft) International Research Training Group INTERCOAST (Integrated Coastal Zone and Shelf-Sea Research). Wave buoy data were kindly provided by the Bay of Plenty Regional Council. The CamEra system was installed by the Waikato Regional Council. The authors would like to thank George Payne (NIWA) for providing the images and maintaining the system and Wietse van de Lageweg for digitizing the shoreline and barline data used in the present paper. As well, the authors want to acknowledge Dirk Immenga for his precious assistance in collecting local wave data and beach profiles at Tairua Beach in 2011. The data used in this study are available on PANGAEA (http://www.pangaea.de) using the doi of the present publication.

Chapter 6

Conclusion

This thesis investigated the behaviour of the shoreline and the barline of intermediate single-barred embayed beaches at the scale of the embayment. Video imagery techniques allowed the collection of a 7-year dataset of images at Tairua Beach, New Zealand. The resulting extracted shoreline and barline locations [*van de Lageweg et al.* 2013] were an extremely valuable support to the present work. To complete this morphological dataset, a high resolution process-based wave model has been developed in order to study the relation between observed morphodynamics and the wave field patterns in the embayment. A combination of statistical analyses and semi-empirical modelling conducted along this thesis allowed to answer the research questions formulated in section 1.3.

How significant is sandbar rotation at single-barred embayed beaches and how does it relate to external conditions?

Previous studies mentioned the relevance of the cross-shore location, orientation and curvature of the shoreline as parameters of a reduced description of embayed beach shorelines [*Clarke and Eliot* 1982, *Short and Trembanis* 2004, *Ojeda and Guillén* 2008, *Ojeda et al.* 2011, *Turki et al.* 2013b;a, *Ratliff and Murray* 2014]. Regarding the barline, studies focused mainly on its cross-shore migration [*Plant et al.* 1999, *Hoefel and Elgar* 2003, *van Maanen et al.* 2008, *Pape et al.* 2010a;b, *Ruessink et al.* 2009] and its alongshore variability due to the development of morphological features such as rip channels [*Plant et al.* 2006, *Splinter et al.* 2011, *de Schipper et al.* 2014]. Before this work, bar rotation was mainly mentioned in observational studies [*Ojeda et al.* 2011, *van de Lageweg et al.* 2013]. The present thesis demonstrated the relevance of the orientation as a descriptor of the state of the barline of an intermediate single-barred embayed beach, together with its cross-shore position and alongshore variability.

Spectral analyses showed that both the migration and rotation signals of Tairua Beach were dominated by interannual and annual fluctuations. More importantly, migration and rotation were weakly correlated, suggesting the relative independence of both processes.

A semi-empirical model has been developed based on the formulation of the shoreline migration model of *Yates et al.* [2009]. First, the barline migration was simulated by adding to this model a morphodynamic factor accounting for wave breaking over the bar crest. Then, using the assumption that the barline rotation was driven by cross-shore mechanisms, the model was differentiated along the alongshore dimension to account for the variations of cross-shore barline migration along the embayment. The model was extensively calibrated and validated on the 7-year dataset, not only confirming that the rotation of the barline is likely to be driven by cross-shore processes, but also relating the rotation of the barline to the alongshore gradient of wave energy along the embayment.

Indeed, this gradient defines an equilibrium barline angle towards which the barline orientation is driven.

The derivation of the rotation model extracted two rotation mechanisms. The first mechanism is called *pivotal rotation*. The migration rate is directly proportional to the imbalance between the alongshore gradient of wave energy in the bay and an equilibrium gradient corresponding to the concomitant orientation of the barline. The consequent pivotal rotation results from a migration of the barline extremities in opposite direction and can therefore occur without any overall bar migration. The second term describes a *migration-driven* rotation which results from the interaction between the migration of the barline (due to an imbalance of its equilibrium energy defined by its cross-shore position and the simultaneous wave energy conditions) and the alongshore gradient of wave energy that accelerates or slows down this migration at the bay extremities. At Tairua, the pivotal mechanism is strongly dominant. Further research needs to address the relevance of the migration-driven process at other embayed beaches.

Finally the analyses of the characteristic response times related to the migration and the rotation of the barline described by the models showed that both processes exhibit similar response times that depend on the morphodynamic damping factor. Under offshore migration conditions, these characteristic times fall below 35 days whereas they vary between 10 and several 100 days during calm accretive conditions.

Which external drivers can be related to the migration and rotation of an embayed beach shoreline?

Shoreline rotation at embayed beaches is usually associated with longshore transfers of sediment [*Clarke and Eliot* 1982, *Short* 1999]. Recently, *Turki et al.* [2013b] and *Ratliff and Murray* [2014] showed that modelling approaches based on longshore transport processes and ignoring cross-shore processes were able to explain the rotation of embayed beach shorelines. However, *Harley et al.* [2011] and *Harley et al.* [2015] showed by means of principal component analyses (PCAs) that alongshore varying wave conditions along the embayment are able to drive alongshore varying adaptations of the beach cross-shore profile. A differential evolution of the beach cross-shore profiles towards more reflective or more dissipative beach states along the embayment would therefore appear as a rotation of the shoreline.

In order to assess which external driver controls the rotation of the shoreline at Tairua Beach, a PCA was first conducted on the 7-year dataset, extracting two dominant modes representing 79 % of the overall variability of Tairua Beach shoreline. These modes, mixing migration and rotation processes, were re-used in a canonical correlation analysis (CCA) to be related to wave climate parameters. The two modes, reshaped by the CCA, accounted respectively for shoreline migration and for shoreline rotation, even if the second mode also included some migration.

The outcomes of the CCA showed a significant relation between the cross-shore migration of the shoreline and the ratio of peak period over mean period, suggesting a relevant role of the swell in the process. In addition, the CCA also showed a strong relation between the second mode mainly accounting for rotation and the amount of wave energy available for alongshore sediment transport. As a result, a simple shoreline rotation model was designed using this assumption, showing good

skills and therefore confirming the role of the wave obliquity and incident longshore currents and sediment transfers in the rotation of the shoreline at Tairua Beach.

How are the behaviours of the shoreline and the sandbar of a single-barred embayed beach interrelated at the scale of the embayment?

The interdependence of the shoreline and barline of a single-barred embayed beach were evaluated by combining the results of chapter 2 and chapter 4 in terms of modelling with two methods of PCA applied to both the shoreline and barline 7-year dataset.

The first PCA method showed the dominance of migration over rotation in both shoreline and barline morphodynamics. The second method showed that, not only dominant, the migration observed at Tairua Beach could be described by two simultaneous modes. The first mode represented shore and bar migrations in opposite directions and was therefore named *contrasting* mode. On the opposite, the second mode named *joint* mode described the migration of the shoreline and barline in the same direction, shorewards or seawards.

The first mode was associated with wave energy conditions above or below the equilibrium energies defined by the concomitant shoreline and barline positions in the model formulations. Consequently the contrasting mode is related to beach state transitions towards more reflective or more dissipative states. The interpretation of the joint mode in terms of wave energy was more difficult. However, regarding the shape of its spatial EOFs, this mode could be associated with caution to the embayed beach breathing mode described in *Ratliff and Murray* [2014], which would agree with the limited ability of the models to describe its dynamics.

Despite being simultaneous, the shore and bar migrations were described separately in the semi-empirical models. Therefore it appeared that this simultaneity was more related to the fact that the forcing parameter of the migrations is identical in both cases (the wave energy) than to a physical coupling.

The rotations of the shoreline and barline are only partially represented by the simultaneous modes. Instead they are mainly described separately in the subsequent third and fourth modes. This could be related to the fact that these rotations obey to different drivers, namely the wave obliquity for the shoreline and the alongshore gradient of wave energy for the barline, whose correlation depends on the concomitant wave energy. Similarly to the migration, the rotations of the shoreline and barline appear therefore as largely independent processes, that can however occur simultaneously due to the partial correlation between the obliquity of the incident waves and the alongshore gradient of wave energy in the embayment.

The analysis does not conclude that there is no coupling between the shoreline and the barline of a single-barred embayed beach. However, within the assumption that the amount of sediment is constant within the embayment, if there is such coupling, it is likely to be a secondary process as most of the shoreline and barline variability can be explained by independent semi-empirical models. This coupling possibly appears through the joint mode, potentially describing a breathing of the beach, and not well simulated by the models.

Chapter 7

Outlook and perspectives

7.1. Thesis outlook

In this thesis, the analyses of single-barred embayed beach morphodynamics were performed by means of statistical and semi-statistical tools. Semi-empirical modelling used key processes to focus on a limited number of parameters that describes the state of the sandbar or the shoreline (chapters 2 and 4). PCAs and CCAs allowed the extraction of dominant modes of the shoreline and barline variability (chapters 4 and 5). Combined, these tools enabled a reliable interpretation of these dominant modes to be given by relating them to the key processes used in the semi-empirical models (chapter 5).

However, these approaches are limited by the possible correlations between the forcing variables, especially when little is known about the details of the underlying processes. This is a major matter of concern regarding the rotation of the shoreline and barline of single barred embayed beaches. While studies relate shoreline rotation to cross-shore sediment transport and profile adaptation [*Harley et al.* 2011; 2015], the work of this thesis relates shoreline rotation to longshore sediment transport (chapter 4), in agreement with [*van de Lageweg et al.* 2013, *Turki et al.* 2013a;b]. In addition, it was shown in chapter 2 that the rotation of the barline was likely to be induced by cross-shore processes. To clarify between these different processes, a process-based approach can be used to compute the sediment transport patterns over the embayment and assess the balance between cross-shore and longshore transport gradients at the shoreline and the barline. Section 7.2 describes such an approach applied to Tairua Beach together with the measurements that have been undertaken there in March 2014 in order to get insights into the flow patterns in the embayment.

In addition, the research presented in this thesis is mainly based on a morphological dataset collected at Tairua Beach, New Zealand, over seven years. Therefore, the present work focuses on medium-term morphodynamic processes and concerns beaches that exhibit geometrical settings similar to Tairua Beach embayment, with a shoreline sufficiently long to exhibit open coast nearshore flow circulations, and with headlands able to induce alongshore gradients of wave energy in the embayment.

The concept of the rotation of embayed beaches nearshore sandbars developed in chapter 2 was found to depend mainly on the alongshore gradient of wave energy. It would be interesting to investigate how this gradient relates to the geometry of the embayment in order to define more accurately the domain of application of the barline rotation model. Furthermore, additional morphological data of single-barred embayed beaches exhibiting different geometries would allow the concept of barline rotation to be extended to embayments where the rotation may not necessarily be induced by the alongshore gradient of wave energy. This could be the case in very small embay-

ments where the hydrodynamics and morphodynamics are controlled by the headlands (see *Castelle and Coco* [2012]).

In chapter 5, the statistical analyses combined to the outcomes of the semi-empirical models simulating the migration and the rotation of the shoreline and barline concluded that the shoreline and barline are weakly coupled on the monthly to annual scale. However, the joint mode extracted by the principal component analysis described simultaneous shoreward and seaward cross-shore migrations of the shore and bar that could not be well explained by the model. This mode, potentially related to a breathing of the beach, could therefore also relate to a coupling between the shoreline and barline positions. Given the low-frequency of its fluctuations, a longer dataset would allow to analyse its dynamics. Such dataset would also enable to study the effect of potential sediment bypassing at the headlands that could also result in a coupled cross-shore translation of the shoreline and barline. Work is actually currently being done in order to extend the Tairua Beach dataset (see *Biausque et al.* [2016], *in review*).

To finish, this thesis, together with other recent works among which [*Ojeda and Guillén* 2008, *Ojeda et al.* 2011, *Price and Ruessink* 2011, *Turki et al.* 2013a], shows that video imagery is a powerful tool to investigate nearshore morphodynamics. Section 7.3 describes the implementation of such video system on the North Frisian island Sylt (Germany) in order to evaluate the dynamics of its coastline.

7.2. A process-based modelling approach to study sediment paths in the embayment

7.2.1. Morphodynamic modelling

A numerical model was initially developed to compute the wave field over the Bay of Plenty to support the analyses of the camera images in chapters 2, 4 and 5. To study the relationship between the incident wave conditions and the sediment transport paths in Tairua Beach embayment, this model is developed further to account for morphodynamics.

The model includes yet tides and waves by being nested in the NIWA tidal model in terms of water levels (*Stanton et al.* [2001], https://www.niwa.co.nz/services/online-services/tide-forecaster) and in the WaveWatch III Ocean Wave hindcast model (NOAA) for wind and waves.

The tide and wave models are both constituted of nested grids in order to obtain a high grid resolution at Tairua Beach. The extent of the largest grid of each model is shown in Figure 7.1 (panel (a)). Calibration for tides has been performed using water level data collected at three tidal gauges (Korotiti, Tauranga and Lottin, see Figure 7.1, panel (a)) available through LINZ Data Service (Land Information New Zealand). The comparison of the measured and modelled amplitude and phase of the seven main tidal constituents in the Bay of Plenty (M2, N2, S2, K2, K1, O1, P1) shows the good skill of the model (Figure B.1 in appendix B). Similarly, the agreement between measured and modelled wave parameters (significant wave height H_s, peak period T_p, mean period T_m, angle of incidence θ) at the BoPRC buoy **B** is good as shown in Figure B.2 (appendix B).

The validation of the wave model has been done at Tairua Beach using wave data measured in 2011

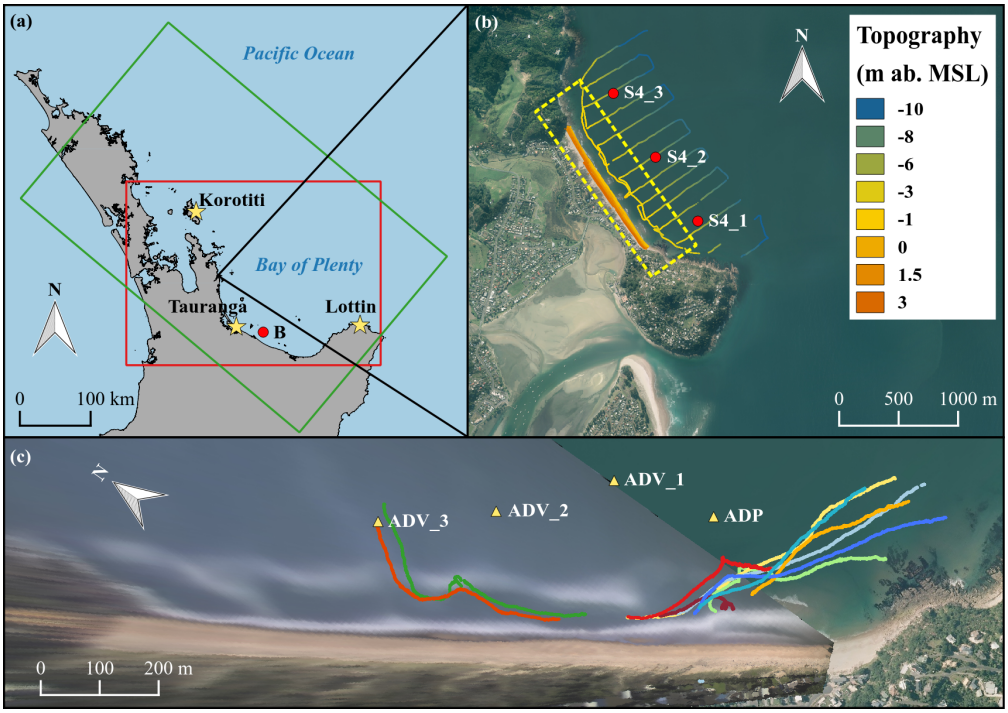

Figure 7.1.: *(a): Tidal model extent (green rectangle) and SWAN wave model extent (red rectangle) over the Bay of Plenty, New Zealand North Island. Three tidal stations (yellow stars) and the location of the BoPRC wave buoy (red circle) are represented. (b): Aerial view of Tairua Beach. The location of three S4 wave measurement devices is given (red circles) as well as the topography measured the 26th of March, 2014. (c): Drifters tracks (colored lines) measured the 27th of March, 2014 between 8:00 and 8:40 NZST over a corresponding georectified image of Tairua Beach. The location of one ADP and three ADV is given (yellow triangles). The area of panel (c) is represented by the yellow dashed rectangle in panel (b). Aerial imagery from Waikato Regional Aerial Photography Service (WRAPS), 2012 via LINZ Data Service.*

[*Daly* 2013]. Results were given with more detail in section 2.3.3 and a comparison of significant wave height and mean wave period between measured and modelled values is given in Figure B.3. Examples of wave and current velocity fields computed at Tairua Beach are presented in Figure B.4. However at this stage the model needs further validation data to simulate accurately the transport of sediment in the bay.

7.2.2. Measurement campaign

A measurement campaign has been conducted in March 2014 to gather the data necessary for the validation of the Tairua morphodynamic model. Seven instruments measuring currents and pressure were deployed in the embayment for four days (three S4 (InterOcean) at locations **S4_1**, **S4_2** and **S4_3**, one Acoustic Doppler Profiler (ADP, Sontek) at location **ADP** and three Acoustic Doppler Velocimeter (ADVs, Sontek) at locations **ADV_1**, **ADV_2** and **ADV_3** (see Figure 7.1). One of the objective of this array of instruments is to catch the main circulations in the embayment. To allow

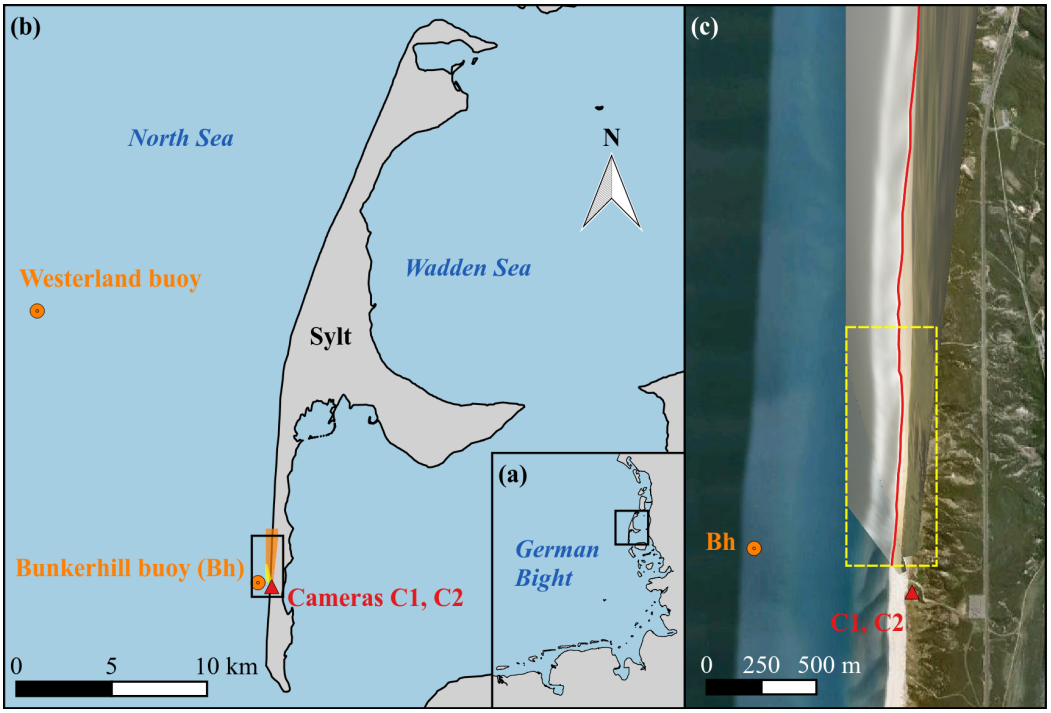

Figure 7.2.: *(a): Location of Sylt in the German Bight (b): Location of cameras **C1** and **C2** (red triangle) and wave buoys (orange circles) on the western shoreface of Sylt. Camera coverage is shown by the yellow and orange areas (c): Example of georectified images from **C1** and **C2** and digitised shoreline (red line) the 21st of June, 2014. Underlying imagery from Google Earth.*

for the modelling of the area, a single-beam bathymetric survey has been conducted during the campaign, supplemented by several topographic surveys of the intertidal area (see Figure 7.1, panel (b)).

In addition, Lagrangian drifters following the design of *MacMahan et al.* [2009] and used in recent studies of nearshore currents [*Reniers et al.* 2009, *McCarroll et al.* 2014, *Winter et al.* 2014] have been deployed in the embayment to measure surface currents. The tracks of ten drifters deployed at low tide are shown in Figure 7.1 (panel (c)). The underlying georectified image enables to locate the nearshore sandbar position, showing that the drifters exit the surfzone at the bar bay where the water depths over the sandbar crest are the deepest.

7.3. Development of a camera system in Sylt, Germany

The use of video imagery techniques in coastal sciences has developed significantly over the past decade, allowing for the study of nearshore morphological features in energetic areas such as the surfzone where it is particularly difficult to deploy in-situ instrumentation. The outcomes of the present work encourages the development of such systems to improve the global understanding of nearshore morphodynamics. For this reason, a video monitoring system installed in Sylt in 2009

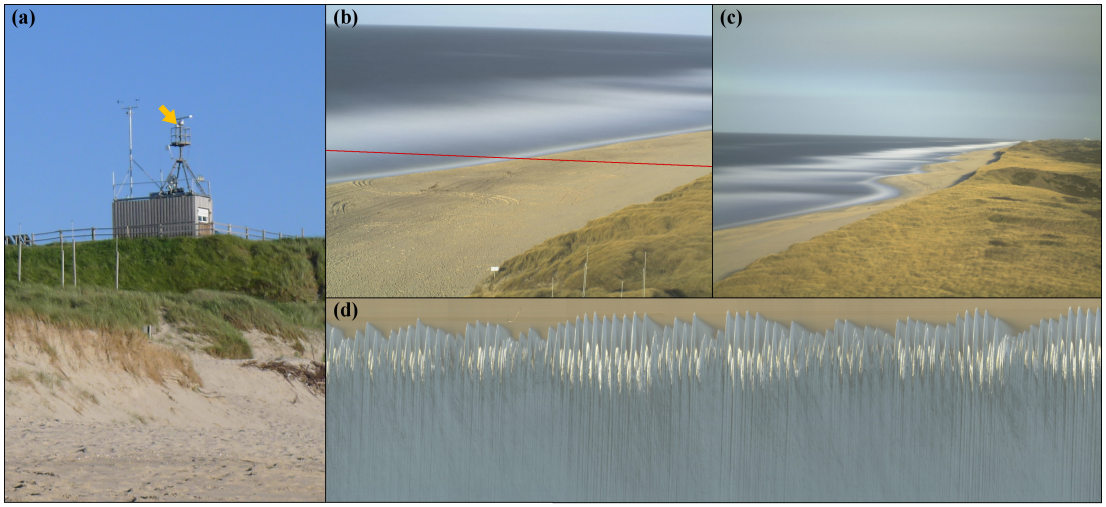

Figure 7.3.: *(a): Location of cameras **C1** and **C2** (yellow arrow). (b, c): Example of 10 minutes averaged images from camera **C1** (b) and camera **C2** (c). (d): Swash area of a timestack image from camera **C1**. Time increases horizontally, towards the right edge of the image. The bottom (top) edge is located seawards (towards the dune foot) respectively. The stacked pixel line is shown in (b) (red line).*

has been upgraded in 2014.

Sylt is a North Frisian island located near the border between Germany and Denmark, at the north of the Wadden sea (see Figure 7.2). The western shoreface is exposed to wind and storm waves from the North Sea, with a tidal range varying between 1.8 and 2.2 m. This coast experienced recurrent erosion over the last centuries (see historical coastline positions in *Thiede and Ahrendt* [2000]). The beach shoreface regularly exhibits two parallel nearshore sandbars whose dynamics are potentially strongly involved in sediment transport patterns and in the underlying erosion of the coastline.

A video monitoring system appears therefore as an appropriate way of monitoring the long-term evolution of the beach profile. Two cameras are located on a coastal dune at approximately 25 m above sea level, offering a horizontal resolution of 6 m at 1 km distance (see cameras **C1** and **C2** and region of interest (yellow dashed rectangle) in Figure 7.2 and cameras mounting in Figure 7.3, panel (a)). Each camera provides hourly time averaged images (Figure 7.3, panels(a, b)) as well as timestack images (one pixel line extracted every 0.25 s during 20 minutes and stacked) allowing for the measurement of the wave propagation celerity and swash excursion (Figure 7.3, panels(d)). In combination with the wave data measured directly offshore of the sandbars and further offshore (Bunkerhill and Westerland buoy respectively, see Figure 7.2), the camera system will enable to study the dynamic behaviour of Sylt western beach shoreface.

Bibliography

Adger, W. N., T. P. Hughes, C. Folke, S. R. Carpenter, and J. Rockström (2005), Social-Ecological Resilience to Coastal Disasters, *Science*, *309*(5737), 1036–1039, doi:10.1126/science.1112122.

Albino, J., J. A. Jiménez, and T. C. Oliveira (2015), Planform and mobility in the Meaípe-Maimbá embayed beach on the South East coast of Brazil, *Geomorphology*, pp. 110–122, doi:10.1016/j.geomorph.2015.09.024.

Almar, R., G. Coco, K. R. Bryan, D. Huntley, A. Short, and N. Sénéchal (2008), Video observations of beach cusp morphodynamics, *Marine Geology*, *254*(3-4), 216–223, doi:10.1016/j.margeo.2008.05.008.

Almar, R., B. Castelle, B. Ruessink, N. Sénéchal, P. Bonneton, and V. Marieu (2010), Two- and three-dimensional double-sandbar system behaviour under intense wave forcing and a meso-macro tidal range, *Continental Shelf Research*, *30*(7), 781–792, doi:10.1016/j.csr.2010.02.001.

Archetti, R., and C. Romagnoli (2011), Analysis of the effects of different storm events on shoreline dynamics of an artificially embayed beach, *Earth Surface Processes and Landforms*, *36*(11), 1449–1463, doi:10.1002/esp.2162.

Ardhuin, F., E. Rogers, A. V. Babanin, J.-F. Filipot, R. Magne, A. Roland, A. van der Westhuysen, P. Queffeulou, J.-M. Lefevre, L. Aouf, and F. Collard (2010), Semiempirical Dissipation Source Functions for Ocean Waves. Part I: Definition, Calibration, and Validation, *J. Phys. Oceanogr.*, *40*(9), 1917–1941, doi:10.1175/2010JPO4324.1.

Ashton, A., A. B. Murray, and O. Arnoult (2001), Formation of coastline features by large-scale instabilities induced by high-angle waves, *Nature*, *414*(6861), 296–300, doi:10.1038/35104541.

Ashton, A. D., and A. B. Murray (2006), High-angle wave instability and emergent shoreline shapes : 1. Modeling of sand waves, flying spits, and capes, *Journal of Geophysical Research*, *111*(F4), F04,011, doi:10.1029/2005JF000422.

Bagnold, R. (1963), Beach and nearshore processes - Part 1, Mechanics of marine sedimentation, *Physics of Sediment Transport by Wind and Water*, p. 188.

Bailard, J. A. (1981), An energetics total load sediment transport model for a plane sloping beach, *Journal of Geophysical Research: Oceans*, *86*(C11), 10,938–10,954, doi:10.1029/JC086iC11p10938.

Battjes, J., and M. Stive (1985), Calibration and verification of a dissipation model for random breaking waves, *Journal of Geophysical Research: Oceans (1978-2012)*, *90*(C5), 9159–9167.

Biausque, M., N. Sénéchal, B. Blossier, and K. R. Bryan (2016), Seasonal variations in recovery timescales of shoreline change on an embayed beach, *Journal of Coastal Research, In Review*.

Blossier, B., K. R. Bryan, and C. Winter (2015), Simple Pocket Beach Rotation Model Derived From

Linear Analysis, in *Proceedings of the Coastal Sediments 2015*, World Scientific, doi:10.1142/9789814689977_0032.

Blossier, B., K. R. Bryan, C. J. Daly, and C. Winter (2016), Nearshore sandbar rotation at single-barred embayed beaches, *Journal of Geophysical Research: Oceans*, *121*(4), 2286–2313, doi:10.1002/2015JC011031.

Booden, M. A., I. E. Smith, J. L. Mauk, and P. M. Black (2012), Geochemical and isotopic development of the Coromandel Volcanic Zone, Northern New Zealand, since 18 Ma, *Journal of Volcanology and Geothermal Research*, *219-220*, 15–32, doi:10.1016/j.jvolgeores.2012.01.005.

Booij, N., R. C. Ris, and L. H. Holthuijsen (1999), A third-generation wave model for coastal regions: 1. Model description and validation, *Journal of Geophysical Research: Oceans*, *104*(C4), 7649–7666, doi:10.1029/98JC02622.

Bowen, A. J., D. L. Inman, and V. P. Simmons (1968), Wave 'Set-Down' and Set-Up, *Journal of Geophysical Research*, *73*(8), 2569–2577, doi:10.1029/JB073i008p02569.

Brander, R. W. (1999), Field observations on the morphodynamic evolution of a low-energy rip current system, *Marine Geology*, *157*(3-4), 199–217, doi:10.1016/S0025-3227(98)00152-2.

Bryan, K. R., R. Foster, and I. MacDonald (2013), Beach Rotation at Two Adjacent Headland-Enclosed Beaches, in *Proceedings of the 12th International Coastal Symposium (Plymouth, England), Journal of Coastal Research, Special Issue 65*, edited by D. C. Conley, G. Masselink, P. E. Russell, and T. J. O'Hare, pp. 2095–2100, doi:10.2112/SI65-354.1.

Burby, R. J. (2006), Hurricane Katrina and the Paradoxes of Government Disaster Policy: Bringing About Wise Governmental Decisions for Hazardous Areas, *The ANNALS of the American Academy of Political and Social Science*, *604*(1), 171–191, doi:10.1177/0002716205284676.

Calvete, D., N. Dodd, A. Falquès, and S. M. van Leeuwen (2005), Morphological development of rip channel systems: Normal and near-normal wave incidence, *Journal of Geophysical Research: Oceans*, *110*(C10), doi:10.1029/2004JC002803, c10006.

Castelle, B., and G. Coco (2012), The morphodynamics of rip channels on embayed beaches, *Continental Shelf Research*, *43*, 10–23, doi:10.1016/j.csr.2012.04.010.

Castelle, B., and G. Coco (2013), Surf zone flushing on embayed beaches, *Geophysical Research Letters*, *40*(10), 2206–2210, doi:10.1002/grl.50485.

Castelle, B., and B. G. Ruessink (2011), Modeling formation and subsequent nonlinear evolution of rip channels: Time-varying versus time-invariant wave forcing, *Journal of Geophysical Research*, *116*(F4), F04,008, doi:10.1029/2011JF001997.

Castelle, B., B. Ruessink, P. Bonneton, V. Marieu, N. Bruneau, and T. Price (2010a), Coupling mechanisms in double sandbar systems. Part 1: patterns and physical explanation, *Earth Surface Processes and Landforms*, *35*(4), 476–486, doi:10.1002/esp.1929.

Castelle, B., B. Ruessink, P. Bonneton, V. Marieu, N. Bruneau, and T. Price (2010b), Coupling mechanisms in double sandbar systems. Part 2: impact on alongshore variability of inner-bar rip channels, *Earth Surface Processes and Landforms*, *35*(7), 771–781, doi:10.1002/esp.1949.

Cavazza, W., F. Immordino, L. Moretti, A. Peirano, A. Pironi, and F. Ruggiero (2000), Sedimentological Parameters and Seagrasses Distributions as Indicators of Anthropogenic Coastal Degradation at Monterosso Bay (Ligurian Sea, NW Italy), *Journal of Coastal Research*, *16*(2), pp. 295–305.

Chadenas, C., A. Creach, and D. Mercier (2014), The impact of storm Xynthia in 2010 on coastal flood prevention policy in France, *Journal of Coastal Conservation*, *18*(5), 529–538, doi:10.1007/s11852-013-0299-3.

Chaibi, M., and M. Sedrati (2009), Coastal Erosion Induced by Human Activities: The Case of Two Embayed Beaches on the Moroccan Coast, *Journal of Coastal Research*, pp. 1184–1188.

Clarke, D., and I. Eliot (1988), Low-frequency variation in the seasonal intensity of coastal weather systems and sediment movement on the beachface of a sandy beach, *Marine Geology*, *79*(1-2), 23–39, doi:10.1016/0025-3227(88)90154-5.

Clarke, D. J., and I. G. Eliot (1982), Description of littoral, alongshore sediment movement from empirical eigenfunction analysis, *Journal of the Geological Society of Australia*, *29*(3-4), 327–341, doi:10.1080/00167618208729217.

Costanza, R., R. d'Arge, R. de Groot, S. Farber, M. Grasso, B. Hannon, K. Limburg, S. Naeem, R. V. O'Neill, J. Paruelo, R. G. Raskin, P. Sutton, and M. van den Belt (1997), The value of the world's ecosystem services and natural capital, *Nature*, *387*(6630), 253–260.

Costanza, R., F. Andrade, P. Antunes, M. v. den Belt, D. Boersma, D. F. Boesch, F. Catarino, S. Hanna, K. Limburg, B. Low, M. Molitor, J. G. Pereira, S. Rayner, R. Santos, J. Wilson, and M. Young (1998), Principles for Sustainable Governance of the Oceans, *Science*, *281*(5374), 198–199, doi:10.1126/science.281.5374.198.

Dally, W. R. (1987), Longshore bar formation: Surf beat or undertow, in *Proc. Specialty Conf. Advances in Understanding of Coastal Sediment Processes, Coastal Sediments 1987*, pp. 71–86, ASCE.

Daly, C., K. Bryan, J. Roelvink, A. Klein, D. Hebbeln, and C. Winter (2011), Morphodynamics of embayed beaches: the effect of wave conditions, *Journal of Coastal Research*, *SI 64*(Proceedings of the 11th International Coastal Symposium), 1003–1007.

Daly, C. J. (2013), Morphodynamic Equilibria of Embayed Beach Systems, Ph.D. thesis, University of Bremen, Germany.

Daly, C. J., K. R. Bryan, and C. Winter (2014), Wave energy distribution and morphological development in and around the shadow zone of an embayed beach, *Coastal Engineering*, *93*(0), 40–54, doi:10.1016/j.coastaleng.2014.08.003.

Daly, C. J., C. Winter, and K. R. Bryan (2015), On the morphological development of embayed beaches, *Geomorphology*, *248*, 252–263, doi:10.1016/j.geomorph.2015.07.040.

Davidson, M., R. Lewis, and I. Turner (2010), Forecasting seasonal to multi-year shoreline change, *Coastal Engineering*, *57*(6), 620–629, doi:10.1016/j.coastaleng.2010.02.001.

Davidson, M., K. Splinter, and I. Turner (2013), A simple equilibrium model for predicting shoreline change, *Coastal Engineering*, *73*(0), 191–202, doi:10.1016/j.coastaleng.2012.11.002.

de Alegria-Arzaburu, A. R., A. Pedrozo-Acuna, J. M. Horrillo-Caraballo, G. Masselink, and D. E. Reeve (2010), Determination of wave-shoreline dynamics on a macrotidal gravel beach using Canonical Correlation Analysis, *Coastal Engineering*, *57*(3), 290–303, doi:10.1016/j.coastaleng.2009.10.014.

de Schipper, M. A., A. J. Reniers, R. Ranasinghe, and M. J. Stive (2014), The influence of sea state on formation speed of alongshore variability in surf zone sand bars, *Coastal Engineering*, *91*(0), 45–59, doi:10.1016/j.coastaleng.2014.05.001.

Dean, R. G. (1973), Heuristic models of sand transport in the surf zone, in *First Australian Conference on Coastal Engineering, 1973: Engineering Dynamics of the Coastal Zone*, p. 215, Institution of Engineers, Australia.

Dehouck, A., H. Dupuis, and N. Sénéchal (2009), Pocket beach hydrodynamics: The example of four macrotidal beaches, Brittany, France, *Marine Geology*, *266*(1-4), 1–17, doi:10.1016/j.margeo.2009.07.008.

Dion, P., and S. L. Bozec (1996), *Marine Benthic Vegetation. Recent Changes and the Effects of Eutrophication*, chap. The French Atlantic Coasts, pp. 251–264, 123, Springer-Verlag Berlin Heidelberg, doi:10.1007/978-3-642-61398-2.

Dormand, J., and P. Prince (1980), A family of embedded Runge-Kutta formulae, *Journal of Computational and Applied Mathematics*, *6*(1), 19–26, doi:10.1016/0771-050X(80)90013-3.

Duxbury, J., and S. Dickinson (2007), Principles for sustainable governance of the coastal zone: In the context of coastal disasters, *Ecological Economics*, *63*(2-3), 319–330, doi:10.1016/j.ecolecon.2007.01.016.

Ebbesen, S., P. Kiwitz, and L. Guzzella (2012), A generic particle swarm optimization Matlab function, in *American Control Conference (ACC, Montréal, Canada)*, pp. 1519–1524, doi:10.1109/ACC.2012.6314697.

Eliot, I., and D. Clarke (1982), Seasonal and biennial fluctuation in subaerial beach sediment volume on Warilla Beach, New South Wales, *Marine Geology*, *48*(1-2), 89–103, doi:10.1016/0025-3227(82)90131-1.

Falquès, A., N. Dodd, R. Garnier, F. Ribas, L. MacHardy, P. Larroudé, D. Calvete, and F. Sancho (2008), Rhythmic surf zone bars and morphodynamic self-organization, *Coastal Engineering*, *55*(7-8), 622–641, doi:10.1016/j.coastaleng.2007.11.012.

Ferrer, P., R. Certain, J. Barusseau, and M. Gervais (2009), Conceptual modelling of a double crescentic barred coast (Leucate beach, France), in *Coastal Dynamics 2009, Tokyo, Japan*.

Gallop, S., K. Bryan, G. Coco, and S. Stephens (2011), Storm-driven changes in rip channel patterns on an embayed beach, *Geomorphology*, *127*(3-4), 179–188, doi:10.1016/j.geomorph.2010.12.014.

Garnier, R., D. Calvete, A. Falquès, and N. Dodd (2008), Modelling the formation and the long-term behavior of rip channel systems from the deformation of a longshore bar, *Journal of Geophysical Research*, *113*(C7), C07,053, doi:10.1029/2007JC004632.

Garnier, R., A. Falquès, D. Calvete, J. Thiébot, and F. Ribas (2013), A mechanism for sandbar straightening by oblique wave incidence, *Geophysical Research Letters*, *40*(11), 2726–2730, doi:10.1002/grl.50464.

Goldberg, D. E. (1989), *Genetic Algorithms in Search, Optimization and Machine Learning*, 1st ed., Addison-Wesley Longman Publishing Co., Inc., Boston, MA, USA.

Guedes, R. M., K. R. Bryan, and G. Coco (2012), Observations of alongshore variability of swash motions on an intermediate beach, *Continental Shelf Research*, *48*, 61–74, doi:10.1016/j.csr.2012.08.022.

Guedes, R. M. C., K. R. Bryan, G. Coco, and R. A. Holman (2011), The effects of tides on swash statistics on an intermediate beach, *Journal of Geophysical Research: Oceans*, *116*(C4), doi:10.1029/2010JC006660.

Hannachi, A., I. T. Jolliffe, and D. B. Stephenson (2007), Empirical orthogonal functions and related techniques in atmospheric science: A review, *International Journal of Climatology*, *27*(9), 1119–1152, doi:10.1002/joc.1499.

Harley, M. D., I. L. Turner, A. D. Short, and R. Ranasinghe (2011), A reevaluation of coastal embayment rotation: The dominance of cross-shore versus alongshore sediment transport processes, Collaroy-Narrabeen Beach, southeast Australia, *Journal of Geophysical Research*, *116*(F04033), doi:10.1029/2011JF001989.

Harley, M. D., I. L. Turner, and A. D. Short (2015), New insights into embayed beach rotation: The importance of wave exposure and cross-shore processes, *Journal of Geophysical Research: Earth Surface*, doi:10.1002/2014JF003390, 2014JF003390.

Healy, T., and T. Soomere (2008), Managed Retreat – Is It Really an Option for Mitigation of Chronic Erosion and Storm Surge Flooding?, in *Solutions to Coastal Disasters 2008*, vol. Solutions to Coastal Disasters 2008, pp. 456–462, doi:10.1061/40968(312)41.

Heikkila, J., and O. Silven (1997), A four-step camera calibration procedure with implicit image correction, in *Proceedings of IEEE Computer Society Conference on Computer Vision and Pattern Recognition, 1997*, pp. 1106–1112, doi:10.1109/CVPR.1997.609468.

Hoefel, F., and S. Elgar (2003), Wave-Induced Sediment Transport and Sandbar Migration, *Science*, *299*(5614), 1885–1887, doi:10.1126/science.1081448.

Hsu, J., and C. Evans (1989), Parabolic bay shapes and applications., in *ICE Proceedings*, vol. 87, pp. 557–570, Thomas Telford.

Iglesias, G., I. López, A. Castro, and R. Carballo (2009), Neural network modelling of planform geometry of headland-bay beaches, *Geomorphology*, *103*(4), 577–587, doi:10.1016/j.geomorph.2008.08.002.

Inman, D. L., and R. Bagnold (1963), Littoral processes, *The sea*, *3*, 529–553.

Jara, M., M. González, and R. Medina (2015), Shoreline evolution model from a dynamic equilibrium beach profile, *Coastal Engineering*, *99*(0), 1–14, doi:10.1016/j.coastaleng.2015.02.006.

Karunarathna, H., J. M. Horrillo-Caraballo, R. Ranasinghe, A. D. Short, and D. E. Reeve (2012), An analysis of the cross-shore beach morphodynamics of a sandy and a composite gravel beach, *Marine Geology*, *299-302*(0), 33–42, doi:10.1016/j.margeo.2011.12.011.

Kirkpatrick, S., C. D. Gelatt, and M. P. Vecchi (1983), Optimization by Simulated Annealing, *Science*, *220*(4598), 671–680, doi:10.1126/science.220.4598.671.

Klein, A. H. d. F., L. B. Filho, and D. H. Schumacher (2002), Short-Term Beach Rotation Processes in Distinct Headland Bay Beach Systems, *Journal of Coastal Research*, *18*(3), pp. 442–458.

Knutson, T. R., J. L. McBride, J. Chan, K. Emanuel, G. Holland, C. Landsea, I. Held, J. P. Kossin, A. K. Srivastava, and M. Sugi (2010), Tropical cyclones and climate change, *Nature Geoscience*, *3*(3), 157–163.

Komar, P. D., and D. L. Inman (1970), Longshore sand transport on beaches, *Journal of Geophysical Research*, *75*(30), 5914–5927.

Larson, M., M. Capobianco, and H. Hanson (2000), Relationship between beach profiles and waves at Duck, North Carolina, determined by canonical correlation analysis, *Marine Geology*, *163*, 275–288, doi:10.1016/S0025-3227(99)00119-X.

Lasagna, R., M. Montefalcone, G. Albertelli, N. Corradi, M. Ferrari, C. Morri, and C. N. Bianchi (2011), Much damage for little advantage: Field studies and morphodynamic modelling highlight the environmental impact of an apparently minor coastal mismanagement, *Estuarine, Coastal and Shelf Science*, *94*(3), 255–262, doi:10.1016/j.ecss.2011.07.003.

LeBlond, P. (1972), On the formation of spiral beaches, *Coastal Engineering Proceedings*, *1*(13).

Leblond, P. H. (1979), An explanation of the logarithmic spiral plan shape of headland-bay beaches, *Journal of Sedimentary Research*, *49*(4).

Lippmann, T., and R. Holman (1990), The Spatial and Temporal Variability of Sand Bar Morphology, *Journal of Geophysical Research*, *95*(C7), 11,575–11,590.

Longuet-Higgins, M., and R. Stewart (1964), Radiation stresses in water waves; a physical discussion, with applications, *Deep Sea Research and Oceanographic Abstracts*, *11*(4), 529–562, doi:10.1016/0011-7471(64)90001-4.

Longuet-Higgins, M. S. (1963), The effect of non-linearities on statistical distributions in the theory of sea waves, *Journal of Fluid Mechanics*, *17*, 459–480, doi:10.1017/S0022112063001452.

MacMahan, J., J. Brown, and E. Thornton (2009), Low-Cost Handheld Global Positioning System for Measuring Surf-Zone Currents, *Journal of Coastal Research*, *25*(3), 744–754.

Martínez, M., A. Intralawan, G. Vázquez, O. Pérez-Maqueo, P. Sutton, and R. Landgrave (2007), The coasts of our world: Ecological, economic and social importance, *Ecological Economics*, *63*(2-3), 254–272, doi:10.1016/j.ecolecon.2006.10.022.

Masselink, G., and A. Short (1993), The Effect of Tide Range on Beach Morphodynamics and Morphology: A Conceptual Beach Model, *Journal of Coastal Research*, *9*(3), 785–800.

McCarroll, R. J., R. W. Brander, J. H. MacMahan, I. L. Turner, A. J. H. M. Reniers, J. A. Brown, A. Bradstreet, and S. Sherker (2014), Evaluation of swimmer-based rip current escape strategies, *Natural Hazards*, *71*(3), 1821–1846, doi:10.1007/s11069-013-0979-1.

Miller, J. K., and R. G. Dean (2004), A simple new shoreline change model, *Coastal Engineering*, *51*(7), 531–556, doi:10.1016/j.coastaleng.2004.05.006.

Miller, J. K., and R. G. Dean (2007a), Shoreline variability via empirical orthogonal function analysis: Part I temporal and spatial characteristics, *Coastal Engineering*, *54*(2), 111–131, doi:10.1016/j.coastaleng.2006.08.013.

Miller, J. K., and R. G. Dean (2007b), Shoreline variability via empirical orthogonal function analysis: Part II relationship to nearshore conditions, *Coastal Engineering*, *54*(2), 133–150, doi:10.1016/j.coastaleng.2006.08.014.

Mrini, A. E., M. Maanan, E. Anthony, and M. Taaouati (2012), An integrated approach to characterize the interaction between coastal morphodynamics, geomorphological setting and human interventions on the Mediterranean beaches of northwestern Morocco, *Applied Geography*, *35*(1-2), 334–344, doi:10.1016/j.apgeog.2012.08.009.

Murray, C., and D. Marmorek (2003), Adaptive Management: a science-based approach to managing ecosystems in the face of uncertainties, in *Munro, N. (Ed.), Fifth International Conference on Science and Management of Protected Areas: Making Ecosystem Based Management Work. Victoria, B. C.*, pp. 11–16.

Neumann, B., A. T. Vafeidis, J. Zimmermann, and R. J. Nicholls (2015), Future Coastal Population Growth and Exposure to Sea-Level Rise and Coastal Flooding - A Global Assessment, *PLoS ONE*, *10*(1932-6203), doi:10.1371/journal.pone.0118571.

New Zealand Department of Conservation (2010), *New Zealand Coastal Policy Statement*, vol. 3, Department of Conservation, PO Box 10420, The Terrace, Wellington 6143, New Zealand.

Nicholls, R. J., and A. Cazenave (2010), Sea-Level Rise and Its Impact on Coastal Zones, *Science*, *328*(5985), 1517–1520, doi:10.1126/science.1185782.

Nordstrom, K. F. (2004), *Beaches And Dunes of Developed Coasts*, Cambridge University Press.

North, G. R., T. L. Bell, R. F. Cahalan, and F. J. Moeng (1982), Sampling Errors in the Estimation of Empirical Orthogonal Functions, *Mon. Wea. Rev.*, *110*(7), 699–706, doi:10.1175/1520-0493(1982)110<0699:SEITEO>2.0.CO;2.

Ojeda, E., and J. Guillén (2008), Shoreline dynamics and beach rotation of artificial embayed beaches, *Marine Geology*, *253*(1-2), 51–62, doi:10.1016/j.margeo.2008.03.010.

Ojeda, E., J. Guillén, and F. Ribas (2011), Dynamics of single-barred embayed beaches, *Marine Geology*, *280*(1-4), 76–90, doi:10.1016/j.margeo.2010.12.002.

Pape, L., B. Ruessink, M. A. Wiering, and I. L. Turner (2007), Recurrent neural network modeling of nearshore sandbar behavior, *Neural Networks*, *20*(4), 509–518, doi:10.1016/j.neunet.2007.04.007.

Pape, L., N. Plant, and B. Ruessink (2010a), On cross-shore migration and equilibrium states of nearshore sandbars, *Journal of Geophysical Research*, *115*(F3), F03,008.

Pape, L., Y. Kuriyama, and B. G. Ruessink (2010b), Models and scales for cross-shore sandbar migration, *Journal of Geophysical Research: Earth Surface*, *115*(F3), doi:10.1029/2009JF001644.

Plant, N., K. Todd Holland, and R. Holman (2006), A dynamical attractor governs beach response to storms, *Geophysical Research Letters*, *33*(17), L17,607, doi:10.1029/2006GL027105.

Plant, N. G., R. A. Holman, M. H. Freilich, and W. A. Birkemeier (1999), A simple model for interannual sandbar behavior, *Journal of Geophysical Research: Oceans*, *104*(C7), 15,755–15,776, doi:10.1029/1999JC900112.

Press, W. H., S. A. Teukolsky, W. T. Vetterling, and B. P. Flannery (1992), Numerical Recipes in Fortran 77: The Art of Scientific Computing, *Cambridge University Press, Cambridge*.

Price, T., and B. Ruessink (2011), State dynamics of a double sandbar system, *Continental Shelf Research*, *31*(6), 659–674, doi:10.1016/j.csr.2010.12.018.

Ranasinghe, R., G. Symonds, K. Black, and R. Holman (2004a), Morphodynamics of intermediate beaches: a video imaging and numerical modelling study, *Coastal Engineering*, *51*(7), 629–655, doi:10.1016/j.coastaleng.2004.07.018.

Ranasinghe, R., R. McLoughlin, A. Short, and G. Symonds (2004b), The Southern Oscillation Index, wave climate, and beach rotation, *Marine Geology*, *204*(3-4), 273–287, doi:10.1016/S0025-3227(04)00002-7.

Ratliff, K. M., and A. B. Murray (2014), Modes and emergent time scales of embayed beach dynamics, *Geophysical Research Letters*, *41*(20), 7270–7275, doi:10.1002/2014GL061680.

Rea, C. C., and P. D. Komar (1975), Computer simulation models of a hooked beach shoreline configuration, *Journal of Sedimentary Research*, *45*(4).

Reeve, D. E., J. M. Horrillo-Caraballo, and V. Magar (2008), Statistical analysis and forecasts of long-term sandbank evolution at Great Yarmouth, {UK}, *Estuarine, Coastal and Shelf Science*, *79*(3), 387–399, doi:10.1016/j.ecss.2008.04.016.

Reniers, A., J. Roelvink, and E. Thornton (2004), Morphodynamic modeling of an embayed beach under wave group forcing, *Journal of Geophysical Research*, *109*(C1), C01,030, doi:10.1029/2002JC001586.

Reniers, A. J. H. M., J. H. MacMahan, E. B. Thornton, T. P. Stanton, M. Henriquez, J. W. Brown, J. A. Brown, and E. Gallagher (2009), Surf zone surface retention on a rip-channeled beach, *Journal of Geophysical Research: Oceans*, *114*(C10), n/a–n/a, doi:10.1029/2008JC005153, c10010.

Ruessink, B., L. Pape, and I. Turner (2009), Daily to interannual cross-shore sandbar migration: Observations from a multiple sandbar system, *Continental Shelf Research*, *29*(14), 1663–1677, doi:10.1016/j.csr.2009.05.011.

Ruessink, B. G., Y. Kuriyama, A. J. H. M. Reniers, J. A. Roelvink, and D. J. R. Walstra (2007a), Modeling cross-shore sandbar behavior on the timescale of weeks, *Journal of Geophysical Research: Earth Surface*, *112*(F3), F03,010, doi:10.1029/2006JF000730.

Ruessink, B. G., G. Coco, R. Ranasinghe, and I. L. Turner (2007b), Coupled and noncoupled behavior of three-dimensional morphological patterns in a double sandbar system, *Journal of Geophysical Research: Oceans*, *112*(C7), C07,002, doi:10.1029/2006JC003799.

Schulz, M., and M. Mudelsee (2002), REDFIT: estimating red-noise spectra directly from unevenly spaced paleoclimatic time series, *Computers & Geosciences*, *28*(3), 421–426.

Short, A., and C. Hogan (1994), Rip Currents and Beach Hazards: Their Impact on Public Safety and Implications for Coastal Management, *Journal of Coastal Research*, pp. pp. 197–209.

Short, A. D. (1999), *Handbook of Beach and Shoreface Morphodynamics*, John Wiley & Sons.

Short, A. D., and A. C. Trembanis (2004), Decadal Scale Patterns in Beach Oscillation and Rotation Narrabeen Beach, Australia: Time Series, PCA and Wavelet Analysis, *Journal of Coastal Research*, *20*(2), pp. 523–532.

Silva, R., A. Baquerizo, M. A. Losada, and E. Mendoza (2010), Hydrodynamics of a headland-bay beach – Nearshore current circulation, *Coastal Engineering*, *57*(2), 160–175, doi:10.1016/j.coastaleng.2009.10.003.

Silvester, R. (1960), Stabilization of Sedimentary Coastlines, *Nature*, *188*(4749), 467–469.

Small, C., and R. J. Nicholls (2003), A Global Analysis of Human Settlement in Coastal Zones, *Journal of Coastal Research*, *19*(3), pp. 584–599.

Small, C., V. Gornitz, and J. E. Cohen (2000), Coastal Hazards and the Global Distribution of Human Population, *Environmental Geosciences*, *7*(1), 3–12, doi:10.1046/j.1526-0984.2000.71005.x.

Smith, R., and K. Bryan (2007), Monitoring Beach Face Volume with a Combination of Intermittent Profiling and Video Imagery, *Journal of Coastal Research*, *23*(4), 892–898, doi:10-2112/04-0287.1.

Soomere, T., A. Kask, J. Kask, and T. Healy (2008), Modelling of wave climate and sediment transport patterns at a tideless embayed beach, Pirita Beach, Estonia, *Journal of Marine Systems*, *74, Supplement*, S133–S146, doi:10.1016/j.jmarsys.2008.03.024, baltic Sea Science Congress 2007Baltic Sea Science Congress 2007.

Soulsby, R. (1995), Bed shear-stresses due to combined waves and currents, *Advances in Coastal Morphodynamics*, pp. 4–20.

Soulsby, R. (1997), *Dynamics of Marine Sands: A Manual For Practical Applications*, Thomas Telford.

Splinter, K. D., R. A. Holman, and N. G. Plant (2011), A behavior-oriented dynamic model for sandbar migration and 2DH evolution, *Journal of Geophysical Research: Oceans*, *116*(C01020), doi:10.1029/2010JC006382.

Stanton, B. R., D. G. Goring, and R. G. Bell (2001), Observed and modelled tidal currents in the New Zealand region, *New Zealand Journal of Marine and Freshwater Research*, *35*(2), 397–415, doi:10.1080/00288330.2001.9517010.

Thiede, J., and K. Ahrendt (2000), Klimaänderung und Küste – Fallstudie Sylt. Teilprojekt: Klimabedingte Veränderung der Gestalt der Insel Sylt, *Tech. rep.*, Forschungszentrum für marine Geowissenschaften der Christian-Albrechts-Universität zu Kiel.

Thomson, D. J. (1990), Time Series Analysis of Holocene Climate Data, *Philosophical Transactions of the Royal Society of London. Series A, Mathematical and Physical Sciences*, *330*(1615), pp. 601–616.

Turki, I., R. Medina, M. Gonzalez, and G. Coco (2013a), Natural variability of shoreline position: Observations at three pocket beaches, *Marine Geology*, *338*, 76–89, doi:10.1016/j.margeo.2012.10.007.

Turki, I., R. Medina, G. Coco, and M. Gonzalez (2013b), An equilibrium model to predict shoreline rotation of pocket beaches, *Marine Geology*, *346*(0), 220–232, doi:10.1016/j.margeo.2013.08.002.

UN Millenium Project (2005), *Environment and Human Well-being: A Practical Strategy.*, Report of the Task Force on Environment Sustainability, London: Earthscan.

United Nations Conference on Environment and Development, Rio de Janeiro, Brazil (1992), *Agenda 21, Rio Declaration*.

U.S. Army Corps of Engineers (2009), Louisiana Coastal Protection and Restoration (LAPCR) Final Technical Report, *Tech. rep.*, New Orleans District, Mississippi Valley Division.

van de Lageweg, W., K. Bryan, G. Coco, and B. Ruessink (2013), Observations of shoreline-sandbar coupling on an embayed beach, *Marine Geology*, *344*(0), 101–114, doi:10.1016/j.margeo.2013.07.018.

van Enckevort, I., and B. Ruessink (2001), Effect of hydrodynamics and bathymetry on video estimates of nearshore sandbar position, *Journal of Geophysical Research*, *106*(C8), 16,969–16,979, doi:10.1029/1999JC000167.

van Enckevort, I. M. J., B. G. Ruessink, G. Coco, K. Suzuki, I. L. Turner, N. G. Plant, and R. A. Holman (2004), Observations of nearshore crescentic sandbars, *Journal of Geophysical Research: Oceans*, *109*(C6), doi:10.1029/2003JC002214.

van Maanen, B., P. de Ruiter, G. Coco, K. Bryan, and B. Ruessink (2008), Onshore sandbar migration at Tairua Beach (New Zealand): Numerical simulations and field measurements, *Marine Geology*, *253*(3-4), 99–106, doi:10.1016/j.margeo.2008.05.007.

van Rijn, L. (2007), Unified view of sediment transport by currents and waves – Part I, II, III and IV, *Journal of Hydraulic Engineering, ASCE*, *133*(6-7).

van Rijn, L., D. Walstra, B. Grasmeijer, J. Sutherland, S. Pan, and J. Sierra (2003), The predictability of cross-shore bed evolution of sandy beaches at the time scale of storms and seasons using process-based Profile models, *Coastal Engineering*, *47*(3), 295–327, doi:10.1016/S0378-3839(02)00120-5.

Walters, R. A., D. G. Goring, and R. G. Bell (2001), Ocean tides around New Zealand, *New Zealand Journal of Marine and Freshwater Research*, *35*(3), 567–579, doi:10.1080/00288330.2001.9517023.

Wilks, D. (2011), Chapter 12 - Principal Component (EOF) Analysis, in *Statistical Methods in the Atmospheric Sciences*, *International Geophysics*, vol. 100, edited by D. S. Wilks, pp. 519–562, Academic Press, doi:10.1016/B978-0-12-385022-5.00012-9.

Winter, G., A. van Dongeren, M. de Schipper, and J. van Thiel de Vries (2014), Rip currents under obliquely incident wind waves and tidal longshore currents, *Coastal Engineering*, *89*(0), 106–119, doi:10.1016/j.coastaleng.2014.04.001.

Wright, L., and A. Short (1984), Morphodynamic variability of surf zones and beaches: A synthesis, *Marine Geology*, *56*(1-4), 93–118, doi:10.1016/0025-3227(84)90008-2.

Yasso, W. E. (1965), Plan Geometry of Headland-Bay Beaches, *The Journal of Geology*, *73*(5), pp. 702–714.

Yates, M. L., R. T. Guza, and W. C. O'Reilly (2009), Equilibrium shoreline response: Observations and modeling, *Journal of Geophysical Research: Oceans*, *114*(C09014), doi:10.1029/2009JC005359.

Yates, M. L., R. T. Guza, W. C. O'Reilly, J. E. Hansen, and P. L. Barnard (2011), Equilibrium shoreline response of a high wave energy beach, *Journal of Geophysical Research: Oceans*, *116*(C4), doi:10.1029/2010JC006681.

Appendix A

Semi-empirical models derivations

A.1. Barline migration model

The barline migration model is an extension of the shoreline migration model of *Yates et al.* [2009]. This model, that can be applied to beach cross-shore transects, is in the present study alongshore averaged to allow for its free parameters not to be constant alongshore. The morphodynamic damping factor (Equation 2.3) is not taken into account here since it is considered alongshore uniform. The alongshore-averaged model of *Yates et al.* [2009] is:

$$\overline{\frac{\partial y_b}{\partial t}} = \overline{C_{y_b}\sqrt{E}(E-(a_b y_b + b_b))}, \tag{A.1}$$

$$\overline{C_{y_b}} = C_{y_b}, \tag{A.2}$$

$$E = \overline{E} + \tilde{E}, \tag{A.3}$$

$$y_b = \overline{y_b} + \tilde{y_b}, \tag{A.4}$$

where the symbol $\bar{}$ indicates alongshore averaging. C_{y_b} is considered alongshore uniform and a is symmetric compared to the centre of the beach. E and y_b are linearised, with $\overline{E}$ and $\overline{y_b}$ their alongshore-averaged contributions and $\tilde{E}$ and $\tilde{y_b}$ their asymmetric, linear alongshore-varying contributions respectively. Using this decomposition, Equation A.1 becomes:

$$\overline{\frac{d\overline{y_b}}{dt} + \frac{\partial \tilde{y_b}}{\partial t}} = C_{y_b}\overline{\sqrt{\overline{E}+\tilde{E}}(\overline{E}+\tilde{E}-a_b\overline{y_b}-a_b\tilde{y_b}-b_b)} \tag{A.5}$$

Due to its asymmetry, the alongshore-averaged time-derivative of $\tilde{y_b}$ is zero. In addition, we use a Taylor expansion of $\sqrt{\overline{E}+\tilde{E}}$:

$$\sqrt{\overline{E}+\tilde{E}} = \sqrt{\overline{E}}\left(1+\frac{\tilde{E}}{2\overline{E}}+O\left(\frac{\tilde{E}}{\overline{E}}\right)^2\right), \tag{A.6}$$

to obtain:

$$\begin{aligned}\frac{d\overline{y_b}}{dt} &= C_{y_b}\sqrt{\overline{E}}\,\overline{(\overline{E}+\tilde{E}-a_b\overline{y_b}-a_b\tilde{y_b}-b_b)} \\ &+C_{y_b}\sqrt{\overline{E}}\,\overline{\left(\frac{\tilde{E}}{2\overline{E}}\right)(\overline{E}+\tilde{E}-a_b\overline{y_b}-a_b\tilde{y_b}-b_b)} \\ &+C_{y_b}\sqrt{\overline{E}}\,\overline{\left(O\left(\frac{\tilde{E}}{\overline{E}}\right)^2\right)(\overline{E}+\tilde{E}-a_b\overline{y_b}-a_b\tilde{y_b}-b_b)}, \end{aligned} \tag{A.7}$$

$$\begin{aligned}\frac{d\overline{y_b}}{dt} &= C_{y_b}\sqrt{\overline{E}}\overline{(\overline{E}+\tilde{E}-a_b\overline{y_b}-a_b\tilde{y_b}-b_b)}+C_{y_b}\sqrt{\overline{E}}\,\overline{\frac{\tilde{E}}{2\overline{E}}(\overline{E}+\tilde{E}-a_b\overline{y_b}-a_b\tilde{y_b}-b_b)} \\ &+O\left(\frac{\overline{\tilde{E}^2}}{\sqrt{\overline{E}}}\right). \end{aligned} \tag{A.8}$$

Decomposing and using $\overline{\tilde{E}}=0$:

$$\begin{aligned}\frac{d\overline{y_b}}{dt} &= C_{y_b}\sqrt{\overline{E}}(\overline{E}-\overline{a_b}\,\overline{y_b}-\overline{a_b\tilde{y_b}}-\overline{b_b})+\frac{C_{y_b}}{2\sqrt{\overline{E}}}\left(\overline{\tilde{E}^2}-\overline{a_b\tilde{E}}\,\overline{y_b}-\overline{\tilde{E}a_b\tilde{y_b}}-\overline{b_b\tilde{E}}\right) \\ &+O\left(\frac{\overline{\tilde{E}^2}}{\sqrt{\overline{E}}}\right). \end{aligned} \tag{A.9}$$

Using the symmetry of a and the asymmetry of $\tilde{E}$ and $\tilde{y_b}$, $\overline{a_b\tilde{y_b}}=0$ and $\overline{\frac{a_b\tilde{E}}{2\overline{E}}}\,\overline{y_b}=0$:

$$\frac{d\overline{y_b}}{dt} = C_{y_b}\sqrt{\overline{E}}(\overline{E}-\overline{a_b}\,\overline{y_b}-\overline{b_b})+\frac{C_{y_b}}{2\sqrt{\overline{E}}}\left(\overline{\tilde{E}^2}-\overline{\tilde{E}a_b\tilde{y_b}}-\overline{b_b\tilde{E}}\right)+O\left(\frac{\overline{\tilde{E}^2}}{\sqrt{\overline{E}}}\right), \tag{A.10}$$

$$\frac{d\overline{y_b}}{dt} = C_{y_b}\sqrt{\overline{E}}(\overline{E}-\overline{a_b}\,\overline{y_b}-\overline{b_b})+O\left(\frac{\overline{\tilde{E}^2}}{\sqrt{\overline{E}}}\right). \tag{A.11}$$

After verification, the last term is indeed negligible for more than 94% of the modelled wave conditions.

A.2. Barline rotation model

The barline rotation model is computed by differentiating the model of *Yates et al.* [2009] (Equation 2.2) along the alongshore dimension:

$$\frac{\partial}{\partial x}\left(\frac{\partial y_b}{\partial t}\right)=\frac{\partial}{\partial t}\left(\frac{\partial y_b}{\partial x}\right)=\frac{\partial}{\partial t}\left(\frac{\partial \tilde{y_b}}{\partial x}\right)=C_{y_b}\frac{\partial}{\partial x}\left(\sqrt{E}(E-(a_by_b+b_b)\right). \tag{A.12}$$

Alongshore-averaged, this becomes:

$$\overline{\frac{\partial}{\partial t}\left(\frac{\partial \tilde{y}_b}{\partial x}\right)} = \frac{d\alpha_b}{dt} = C_{y_b}\overline{\frac{\partial}{\partial x}\left(\sqrt{E}(E-(a_b y_b + b_b)\right)}. \tag{A.13}$$

The differentiation and decomposition of E and y_b lead to:

$$\frac{d\alpha_b}{dt} = C_{y_b}\overline{\sqrt{E}\left(\frac{\partial E}{\partial x} - \frac{da_b}{dx}y_b - a_b\frac{\partial y_b}{\partial x} - \frac{db_b}{dx}\right)} + C_{y_b}\overline{\frac{1}{2\sqrt{E}}\frac{\partial E}{\partial x}(E - a_b y_b - b_b)}, \tag{A.14}$$

$$\begin{aligned}\frac{d\alpha_b}{dt} &= C_{y_b}\sqrt{\overline{E}}\overline{\left(1+\frac{\tilde{E}}{2\overline{E}}+O\left(\frac{\tilde{E}}{\overline{E}}\right)^2\right)\left(\frac{\partial E}{\partial x} - \frac{da_b}{dx}y_b - a_b\frac{\partial y_b}{\partial x} - \frac{db_b}{dx}\right)} \\ &+ \frac{C_{y_b}}{2\sqrt{\overline{E}}}\overline{\left(1-\frac{\tilde{E}}{2\overline{E}}+O\left(\frac{\tilde{E}}{\overline{E}}\right)^2\right)\frac{\partial E}{\partial x}(E - a_b y_b - b_b)},\end{aligned} \tag{A.15}$$

$$\begin{aligned}\frac{d\alpha_b}{dt} &= C_{y_b}\sqrt{\overline{E}}\overline{\left(\frac{\partial \tilde{E}}{\partial x} - \frac{da_b}{dx}\overline{y_b} - \frac{da_b}{dx}\tilde{y}_b - a_b\frac{\partial \tilde{y}_b}{\partial x} - \frac{db_b}{dx}\right)} \\ &+ \frac{C_{y_b}}{2\sqrt{\overline{E}}}\overline{\frac{\partial \tilde{E}}{\partial x}\left(\overline{E}+\tilde{E} - a_b\overline{y_b} - a_b\tilde{y}_b - b_b\right)} \\ &+ C_{y_b}\sqrt{\overline{E}}\overline{\left(\frac{\tilde{E}}{2\overline{E}}+O\left(\frac{\tilde{E}}{\overline{E}}\right)^2\right)\left(\frac{\partial \tilde{E}}{\partial x} - \frac{da_b}{dx}\overline{y_b} - \frac{da_b}{dx}\tilde{y}_b - a_b\frac{\partial \tilde{y}_b}{\partial x} - \frac{db_b}{dx}\right)} \\ &+ \frac{C_{y_b}}{2\sqrt{\overline{E}}}\overline{\left(\frac{-\tilde{E}}{2\overline{E}}+O\left(\frac{\tilde{E}}{\overline{E}}\right)^2\right)\frac{\partial \tilde{E}}{\partial x}\left(\overline{E}+\tilde{E} - a_b\overline{y_b} - a_b\tilde{y}_b - b_b\right)}.\end{aligned} \tag{A.16}$$

Using the asymmetry of $\frac{da_b}{dx}$, $\tilde{E}$, $\tilde{y_b}$ and the fact that the alongshore-averaged derivatives of E and y_b are the alongshore derivatives of $\tilde{E}$ and $\tilde{y_b}$ in any point:

$$\begin{aligned}
\frac{d\alpha_b}{dt} &= C_{y_b}\sqrt{\overline{E}}\left(\frac{\partial\tilde{E}}{\partial x}-\overline{\frac{da_b}{dx}\tilde{y_b}}-\overline{a_b}\frac{\partial\tilde{y_b}}{\partial x}-\overline{\frac{db_b}{dx}}\right)+\frac{C_{y_b}}{2\sqrt{\overline{E}}}\frac{\partial\tilde{E}}{\partial x}\left(\overline{E}-\overline{a_b}\,\overline{y_b}-\overline{b_b}\right)\\
&\quad+\frac{C_{y_b}}{2\sqrt{\overline{E}}}\left(-\overline{\frac{da_b}{dx}\tilde{E}}\,\overline{y_b}-\overline{a_b\tilde{E}}\frac{\partial\tilde{y_b}}{\partial x}-\overline{\tilde{E}\frac{db_b}{dx}}\right)+\frac{C_{y_b}}{4\overline{E}^{\frac{3}{2}}}\frac{\partial\tilde{E}}{\partial x}\left(-\overline{\tilde{E}\tilde{E}}+\overline{\tilde{E}a_b\tilde{y_b}}+\overline{\tilde{E}b_b}\right)\\
&\quad+O\left(\frac{\overline{\tilde{E}^3}}{L\sqrt{\overline{E}}}\right)+O\left(\frac{\overline{\tilde{E}^3}}{L\overline{E}^{\frac{3}{2}}}\right), \qquad \text{(A.17)}\\
\frac{d\alpha_b}{dt} &= C_{y_b}\sqrt{\overline{E}}\left(\frac{\partial\tilde{E}}{\partial x}-\overline{\frac{da_b}{dx}\tilde{y_b}}-\overline{a_b}\alpha_b-\overline{\frac{db_b}{dx}}\right)+\frac{C_{y_b}}{2\sqrt{\overline{E}}}\frac{\partial\tilde{E}}{\partial x}\left(\overline{E}-\overline{a_b}\,\overline{y_b}-\overline{b_b}\right)\\
&\quad+O\left(\frac{\overline{\tilde{E}^2}}{L\sqrt{\overline{E}}}\right), \qquad \text{(A.18)}
\end{aligned}$$

with L the length of the beach. The term $\overline{\frac{da_b}{dx}\tilde{y_b}}$ can be further derived. Considering that x varies between 0 and L and using $a_b(0)=a_b(L)$ by symmetry:

$$\begin{aligned}
\overline{\frac{da_b}{dx}\tilde{y_b}} &= \frac{1}{L}\int_0^L\frac{da_b}{dx}\tilde{y_b}dx,\\
&= \frac{1}{L}\int_0^L\frac{da_b}{dx}(\tilde{y_b}(0)+\alpha_b x-\overline{y_b})dx,\\
&= \frac{1}{L}(\tilde{y_b}(0)-\overline{y_b})(a_b(L)-a_b(0))+\frac{\alpha_b}{L}\int_0^L\frac{da_b}{dx}xdx,\\
&= \frac{\alpha_b}{L}\int_0^L\frac{da_b}{dx}xdx,\\
&= \frac{\alpha_b}{L}[a_b x]_0^L-\frac{\alpha_b}{L}\int_0^L a_b dx,\\
&= \alpha_b(a_b(L)-\overline{a_b}). \qquad \text{(A.19)}
\end{aligned}$$

Replacing in the first term of Equation A.18:

$$\frac{d\alpha_b}{dt} = C_{y_b}\sqrt{\overline{E}}\left(\frac{\partial\tilde{E}}{\partial x} - \alpha_b a_b(L) - \overline{\frac{db_b}{dx}}\right) + \frac{C_{y_b}}{2\sqrt{\overline{E}}}\frac{\partial\tilde{E}}{\partial x}\left(\overline{E} - \overline{a_b}\,\overline{y_b} - \overline{b_b}\right) + O\left(\frac{\overline{\tilde{E}^2}}{L\sqrt{\overline{E}}}\right), \tag{A.20}$$

$$\frac{d\alpha_b}{dt} = C_{y_b}\sqrt{\overline{E}}\left(\frac{\partial\tilde{E}}{\partial x} - \delta\overline{a_b}(\alpha_b - \alpha_0)\right) + \frac{C_{y_b}}{2\sqrt{\overline{E}}}\frac{\partial\tilde{E}}{\partial x}\left(\overline{E} - \overline{a_b}\,\overline{y_b} - \overline{b_b}\right) + O\left(\frac{\overline{\tilde{E}^2}}{L\sqrt{\overline{E}}}\right), \tag{A.21}$$

with δ and α_0 corresponding to the following parameterisation:

$$\delta = \frac{a_b(L)}{\overline{a_b}}, \tag{A.22}$$

$$\alpha_0 = -\frac{1}{\delta\overline{a_b}}\overline{\frac{db_b}{dx}}. \tag{A.23}$$

After verification, the last term $O\left(\frac{\overline{\tilde{E}^2}}{L\sqrt{\overline{E}}}\right)$ is indeed negligible for more than 93% of the modelled wave conditions. In Equation 2.8, additional flexibility is given to the model by changing C_{y_b} into C_{α_b}.

Appendix B

Tidal and wave model calibration

B.1. Tidal model

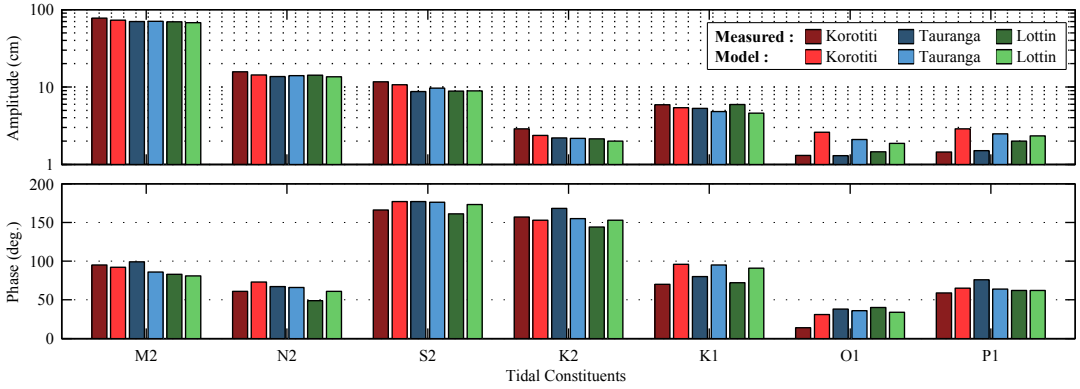

Figure B.1.: *Comparison between measured (darker colors) and modelled (brighter colors) amplitude and phase of seven main tidal constituents at three tidal stations over the Bay of Plenty: Korotiti (red bars), Tauranga (blue bars) and Lottin (green bars) (see their location in Figure 7.1, panel (a)).*

B.2. Wave model and currents

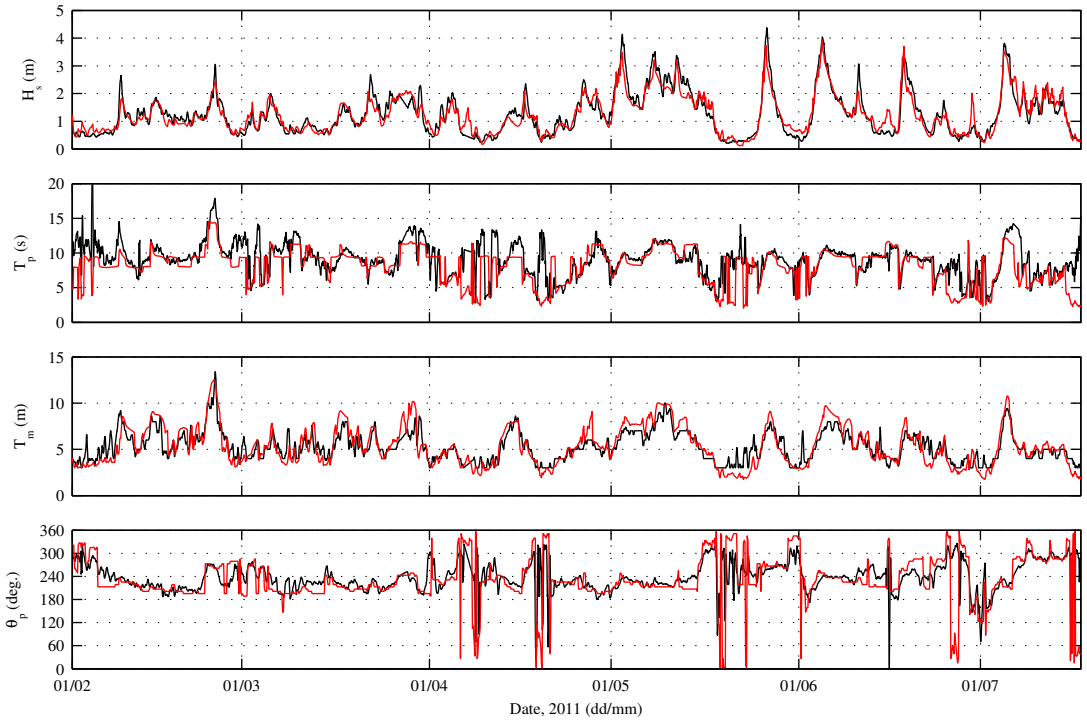

Figure B.2.: *Comparison between measured (black line) and modelled (red line) significant wave height (H_s), peak period (T_p), mean period (T_m) and peak wave angle (θ) at the BoPRC buoy **B** (see location in Figure 7.1, panel (a)).*

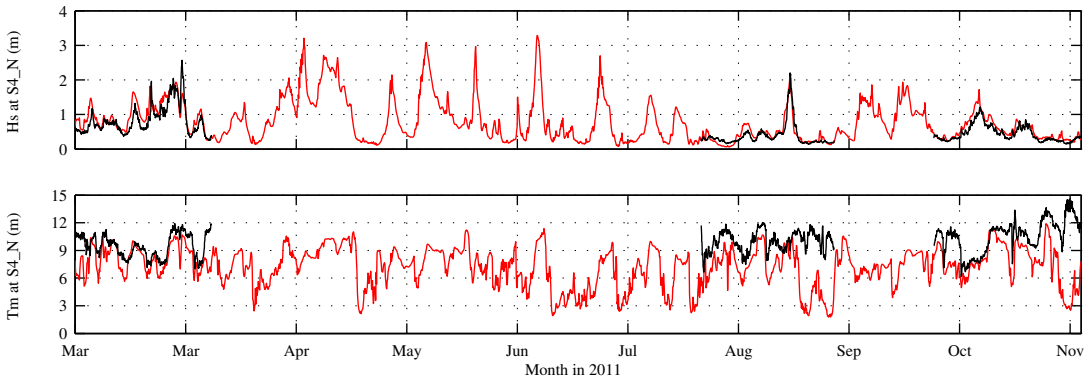

Figure B.3.: *Comparison between measured (black line) and modelled (red line) significant wave height (H_s) and mean period (T_m) at instrument **S4_N** in 2011 (see location in Figure 2.1).*

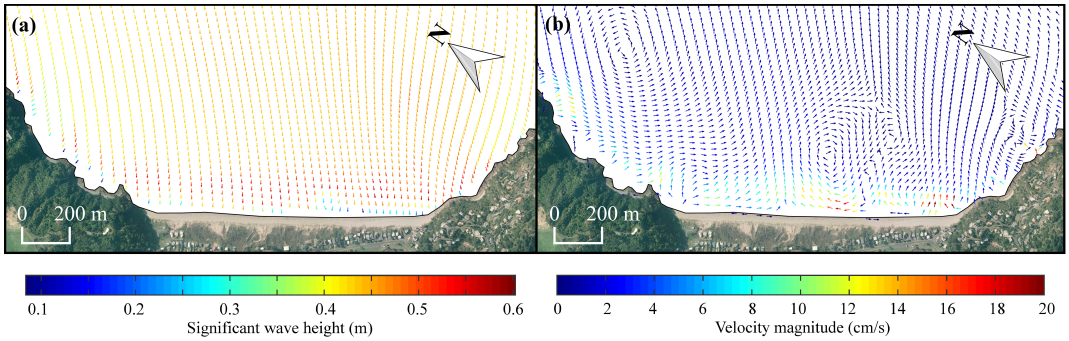

Figure B.4.: *Example of wave (a) and current velocity (b) fields computed at Tairua Beach (12th of May, 2014) at the present stage of model development. Arrows length is normalised. Aerial imagery from Waikato Regional Aerial Photography Service (WRAPS), 2012 via LINZ Data Service.*